SANDIA REPORT

SAND93–0773 • UC–~~400~~ 100
Unlimited Release
Printed August 1993

Experimental and Numerical Studies of High-Velocity Impact Fragmentation

M. E. Kipp, D. E. Grady, J. W. Swegle

Prepared by
Sandia National Laboratories
Albuquerque, New Mexico 87185 and Livermore, California 94550
for the United States Department of Energy
under Contract DE-AC04-76DP00789

Issued by Sandia National Laboratories, operated for the United States Department of Energy by Sandia Corporation.

Available to DOE and DOE contractors from
Office of Scientific and Technical Information
PO Box 62
Oak Ridge, TN 37831

Prices available from (615) 576-8401, FTS 626-8401

Available to the public from
National Technical Information Service
US Department of Commerce
5285 Port Royal Rd
Springfield, VA 22161

NTIS price codes
Printed copy: A07
Microfiche copy: A01

SAND93 - 0773
Unlimited Distribution
August 1993

Distribution
UC-[redacted] 700

Experimental and Numerical Studies of High-Velocity Impact Fragmentation*

M. E. Kipp, D. E. Grady, and J. W. Swegle
Sandia National Laboratories
Department 1430
Albuquerque, New Mexico 87185-5800

ABSTRACT

Developments are reported in both experimental and numerical capabilities for characterizing the debris spray produced in penetration events. We have performed a series of high-velocity experiments specifically designed to examine the fragmentation of the projectile during impact. High-strength, well-characterized steel spheres (6.35 mm diameter) were launched with a two-stage light-gas gun to velocities in the range of 3 to 5 km/s. Normal impact with PMMA plates, thicknesses of 0.6 to 11 mm, applied impulsive loads of various amplitudes and durations to the steel sphere. The extent of fragmentation, loss in momentum, and divergence of the debris are shown to correlate with the impact conditions. Multiple flash radiography diagnostics and recovery techniques were used to assess size, velocity, trajectory and statistics of the impact-induced fragment debris. Damage modes to the primary target plate (plastic) and to a secondary target plate (aluminum) were also evaluated. Dynamic fragmentation theories, based on energy-balance principles, were used to evaluate local material deformation and fracture state information from CTH, a three-dimensional Eulerian solid dynamics shock wave propagation code. The local fragment characterization of the material defines a weighted fragment size distribution, and the sum of these distributions provides a composite particle size distribution for the steel sphere. The calculated axial and radial velocity changes agree well with experimental data, and the calculated fragment sizes for a specific experiment are in qualitative agreement with the radiographic data. A particle cloud impact has been made onto a witness plate to simulate secondary fragment impact. Supporting analytic studies have also been performed.

A secondary effort involved the experimental and computational analyses of normal and oblique copper ball impacts on steel target plates. High-resolution radiography and witness plate diagnostics provided impact motion and statistical fragment size data. CTH simulations were performed to test computational models and numerical methods.

* This work performed at Sandia National Laboratories supported by the U.S. Department of Energy under contract #DE-AC04-76D00789.

Acknowledgments

The authors gratefully acknowledge the support of Sandia National Laboratory funding through a Laboratory Directed Research and Development grant for the fiscal years 1990 to 1992. The expert help of R. Moody in the experimental aspect of this work is acknowledged, as is the support of Millie Elrick in the use of CTH. The radiographs were image-processed by David Johnson.

CONTENTS

	Page
Acknowledgments	4
Contents	5
I. INTRODUCTION	7
II. STEEL SPHERE IMPACT ON PMMA TARGETS	9
A. Experimental Configuration and Materials	9
B. Fragment Debris Experimental Results	11
C. Analysis of the Steel Debris	17
D. Target Crater Characteristics	26
E. Summary of Fragmentation Theory and Code Implementation	28
F. Numerical Simulations of Steel Sphere Impact on PMMA Targets	34
G. Secondary Target Damage	44
H. Numerical Analysis of Debris Cloud Impact on Aluminum Target	53
III. COPPER SPHERE IMPACT ON STEEL TARGETS	58
A. Experimental Configuration and Materials	58
B. Experimental Results	60
C. Numerical Analysis of the Copper Sphere Impact	70
IV. CONCLUSIONS	77
V. REFERENCES	79
APPENDIX A - Debris Cloud Data (Steel Impacts onto PMMA Targets)	81
APPENDIX B - Radiographs (Steel Impacts onto PMMA Targets)	82
APPENDIX C- Foam Block Radiographs (Copper Impacts onto Steel Targets)	124
DISTRIBUTION	127

I. INTRODUCTION

Some basic theories have emerged within the past 10 years for predicting the consequences of dynamic fragmentation brought about by high-velocity impact or explosive events. These theories have focused principally on the prediction of mean fragment size through energy and momentum balance principals (*e.g.* Grady, 1982; Kipp and Grady, 1985; Grady, 1988; Glenn and Chudnovsky, 1986) and on the statistical issues of fragment size distributions (*e.g.* Brown, 1989; Englman, *et al.*, 1984; Grady and Kipp, 1985; Grady, 1990). This theoretical basis has provided the underlying framework for a number of computational algorithms employed to analyze complex fragmentation events (*e.g.* Johnson, *et al.*, 1990; Melosh, *et al.*, 1992; Smith, 1989).

High-velocity impact represents a mechanical event which is ideally suited to treatment with large scale computational wave-propagation codes. Through parametric computational studies involving material properties, geometry and impact velocity, much can be learned about the high-velocity impact process. Such computational studies can also prove useful in guiding the development of models which provide the components for more specific engineering solution methods of the impact process. Because of the high-velocities and intense stress states achieved on impact, a significant portion of the motions are hydrodynamic in nature in spite of the high-strength materials which may be involved in the interaction. Nonetheless, critical aspects of the impact interaction are strongly dependent on strength properties of the materials involved. The total mass and size distribution of ejecta material, along with the size and structure of the impact or penetration crater, depend sensitively on the strength properties.

High-velocity impact also exercises the full thermodynamic equation-of-state of materials. Entropy production due to both the initial shock wave and the dynamic shear deformation will lead to a broad range of temperature states. Melting and vaporization of some fraction of the impact debris will commonly occur above impact velocities of about 5 km/s.

There are, nonetheless, a number of unresolved issues within the development of statistical energy-balance theories of fragmentation, and there is a pressing need for high-resolution experimental data focused on the validation of these theories. Furthermore, implementation of these theories into Eulerian wave propagation codes is important for the purpose of investigating dynamic fragmentation in large scale catastrophic events.

The present studies focus on the development of both numerical and experimental capabilities for characterizing the debris spray produced in penetration events. A systematic fragment debris database is essential for the continued development of a theoretical understanding of fragmentation and the associated computational model development and verification. This investigation of impact-induced fragmentation was undertaken to provide such an experimental base of high-resolution impact fragmentation data for evaluating models and determining the accuracy of current computational fragmentation analysis techniques.

The primary experimental objective in this study was to investigate the dynamic fragmentation characteristics of a high-strength steel through controlled impact experiments, using flash-radiography diagnostics. Experiments of this type usually involve the high-velocity interaction of a metal projectile with a stationary target (plate) of similar or dissimilar metals. We

report high-velocity impact experiments in which copper spheres strike 4340 steel target plates at velocities between 3 and 5 km/s, and at both normal and oblique impact angles. In addition to flash radiography, witness plate and fragment capture methods were used to evaluate size and trajectory statistics of ejecta fragment debris.

Radiographic diagnostics of the fragmentation event cannot readily discern projectile fragments from target fragments, however. In a second suite of experiments, a high-velocity steel sphere, accelerated to a velocity in the range of 3 to 5 km/s, undergoes normal impact on a thin stationary plastic plate. The plate imparts a controlled impulse to the steel sphere of magnitude and duration determined by impact velocity and plate thickness. The radiographic diagnostic exclusively images the fragmented steel sphere, since the target plastic is transparent to the x-ray beam. This technique offers valuable analysis and interpretation features of the fragmentation event not available in multi-metal impact experiments, foremost of which is the association of the known mass of the sphere with the debris in the radiograph. Several secondary issues were also investigated in the experimental aspects of this study. An aluminum target plate was placed at a fixed position behind the primary plastic plate and intercepted the flux of steel fragments. The objective was to assess secondary target damage by a noncontinuum fragment debris pattern. The experimental consequences of the secondary impact event were evaluated. Finally, interesting damage modes were noted in the primary plastic plate and these results have also been documented.

The numerical tool chosen for development of fragmentation prediction capability is the three-dimensional Eulerian wave propagation code, CTH (McGlaun, *et al.*, 1990). A post-processor was developed to determine local average fragment sizes from strain-rate and temperature information, using the dynamic fragmentation theories mentioned previously.

II. STEEL SPHERE IMPACT ON PMMA TARGETS

The first major series of experiments to be reported are focused on the normal impact of hardened steel spheres onto PMMA target plates, with the intent to examine the dependence of the steel fragmentation on the impact conditions. This section includes the experimental description, experimental results, analysis of the data and the approach to numerical analysis of fragmentation events, and concludes with some numerical analysis of the motion of the debris.

A. Experimental Configuration and Materials

The experimental configuration for the series of impact fragmentation tests is shown in Figure 1. Saboted steel spheres were launched at velocities between about 3 to 5 km/s with a two-stage light-gas gun system. The launch tube diameter was 12 mm. Plastic sabots were separated from the steel spheres through forces produced by a slight back pressure in the gun range section. Sabot segments are trapped upstream and do not reach the target impact chamber. Velocity of the steel spheres is measured to ±1% accuracy by recording of the time interval during passage between two magnetic coils of known separation. Normal impact occurred in the target chamber at the center of a 75 mm by 75 mm square plastic target plate of thickness between 0.6 and 11 mm. The plastic is PMMA (polymethyl-methacrylate) Rohm and Haas Type II UVA, and has a nominal density of 1186 kg/m^3.

In all experiments a steel sphere 6.35 mm (1/4 in.) in diameter was used. The measured mass was 1.027 ± 0.001 grams. The steel was AISI E52100 high-carbon chromium steel, heat treated to a Rockwell-C hardness of 60 to 67. The density of the steel is 7837 kg/m^3, static yield strength is

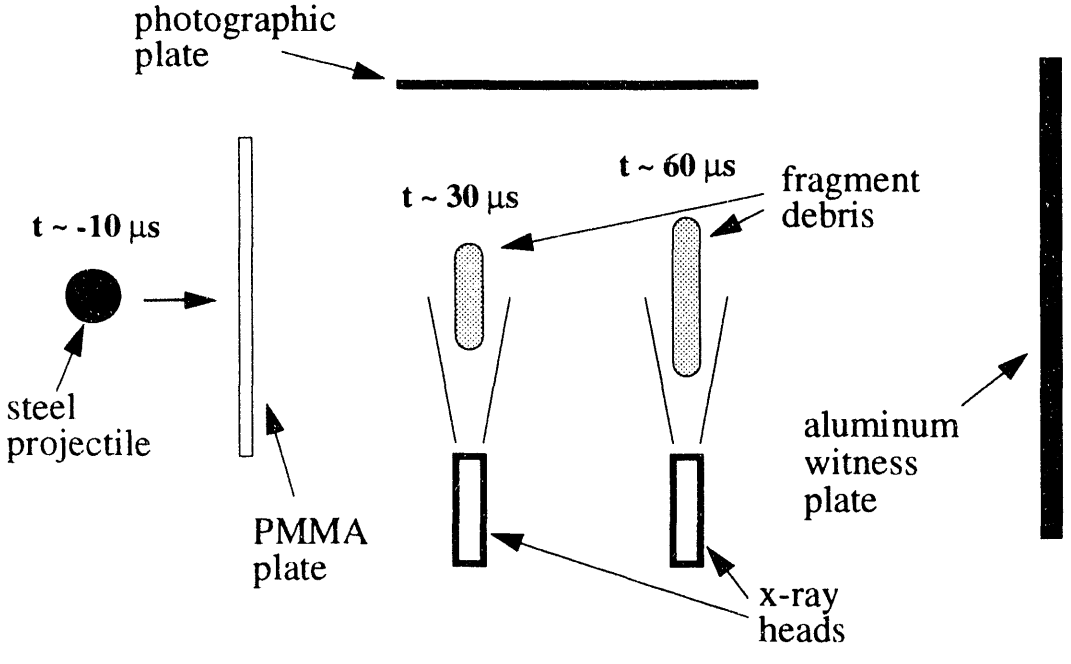

Figure 1. Experimental configuration for radiographic and witness plate diagnostic of impact fragmentation experiment. (Timing is representative of a 5 km/s impact.)

2.03 GPa, fracture toughness is 30 to 40 MPa$\sqrt{m}$, and elastic modulus (Young's) is 200 GPa, with a Poisson ratio of 0.29.

Fragment debris is diagnosed at two stations (approximately 150 mm and 300 mm) downstream from the input point. Two 150 keV flash x-ray tubes, placed approximately 400 mm from the line of debris travel, provided orthogonal shadow-graphs of the fragment debris, as shown in Figure 1. Appropriate delay times were calculated from the predicted impact velocity and x-ray tubes independently triggered from the second magnetic velocity coil. The x-ray film cassette, using Kodak Direct Exposure film backed by a Quanta Fast Detail screen, was stationed about 100 mm from the centerline of the debris trajectory.

For two experiments (Test 1 and Test 2), the x-ray tubes and film cassette were oriented to obtain an oblique shadow-graph of the fragment debris (the x-ray angle was significantly less than the 90 degree orientation to the line of travel used in the majority of the experiments).

Table 1: Experimental Impact Parameters[a]

Test	h	x_{ps}	d_s	V_i	Test	h	x_{ps}	d_s	V_i
#	mm	mm	mm	m/s	#	mm	mm	mm	m/s
1	3.28	b	b	4460	13	5.37	422	12.7	4430
2	3.28	b	b	4460	14	5.36	422	12.7	4060
3	1.74	206	6.35	4450	15	5.38	422	12.7	3310
4	1.74	495	6.35	4700	16	5.37	422	12.7	4080
5	3.38	470	12.7	4570	17	3.25	657	12.7	4520
6	3.28	476	12.7	3460	18	4.71	638	12.7	4430
7	3.44	483	12.7	4160	19	5.39	637	12.7	4610
8	1.49	422	6.35	3950	20	4.75	640	12.7	4040
9	1.51	422	6.35	3460	21	4.78	646	12.7	3750
10	0.63	422	6.35	3410	22	0.99	637	12.7	4700
11	0.64	422	6.35	3920	23	11.23	641	12.7	4060
12	0.69	422	9.53	4470	24	9.47	638	12.7	4030

[a] h = primary plate thickness; x_{ps} = plate separation; d_s = secondary plate thickness; V_i = impact velocity.
[b] Oblique angle radiograph — Witness plate data was not recorded.

An aluminum target plate 152.4 mm (6 in.) on a side and either 6.35 mm (1/4 in.) or 12.7 mm (1/2 in.) in thickness was placed on axis approximately 400 mm down stream from the PMMA primary target plate to intercept the flux of steel fragments. This witness plate, prepared from 6061-T6 aluminum plate stock, was recovered after each experiment, and provided a post-test passive diagnostic of secondary fragmentation effects.

The primary configuration parameters for all experiments in the present study are provided in the first two columns of Table 1, where h is the PMMA plate thickness and V_i is the impact velocity.

B. Fragment Debris Experimental Results

A total of 24 experiments of the basic impact configuration described in the previous section were performed in this investigation. The principal experimental variables were the impact velocity, V_i, and the thickness, h, of the primary target plate (PMMA), which defined the amplitude and duration of the impulse transmitted to the steel sphere, and consequently, the intensity of fragmentation of the steel projectile.

An example of the experimental radiographic results is shown in Figure 2, where the images for Test 5 are displayed. These images qualitatively illustrate the nature of the fragmentation process observed in all of the experiments in the present study, with the exception of several tests in which parameter extremes were reached. The steel fragments remain well grouped and continue to move along the original trajectory at velocities somewhat less than the initial impact velocity, having been slowed by the impulse delivered to the sphere by the plate. Axial dispersion of the fragment debris is quite limited, with fairly well-defined, nearly planar boundaries forming. Radial dispersion is significant, but still the fragments are contained by rather well-defined limits. These observations hold in general except for the very largest of target thicknesses. Since the PMMA is not recorded in the radiograph, we are assured that only the mass of the original steel sphere is represented in each image.

The foremost objective of the experimental study was to assess, through radiographic diagnostics, the kinematic and structural characteristics of the steel fragment debris produced by the impact of the PMMA plate with the steel sphere.

Kinematic Properties of the Debris

Several experimental parameters have been extracted from the data and are included in Table 2. First is the axial velocity decrease, ΔV, of the fragment debris from the initial impact velocity, V_i. Residual velocity, V_r, of the debris is readily calculated from $\Delta V = V_i - V_r$. The magnitude of ΔV can also be regarded as the change in axial velocity of a stationary sphere due to momentum imparted by the impacting plate. This velocity change is determined from the motion of the geometric center of mass of the debris cloud observed in the radiograph. The most accurate value is calculated by using the separation of the two radiographic images and the times at which

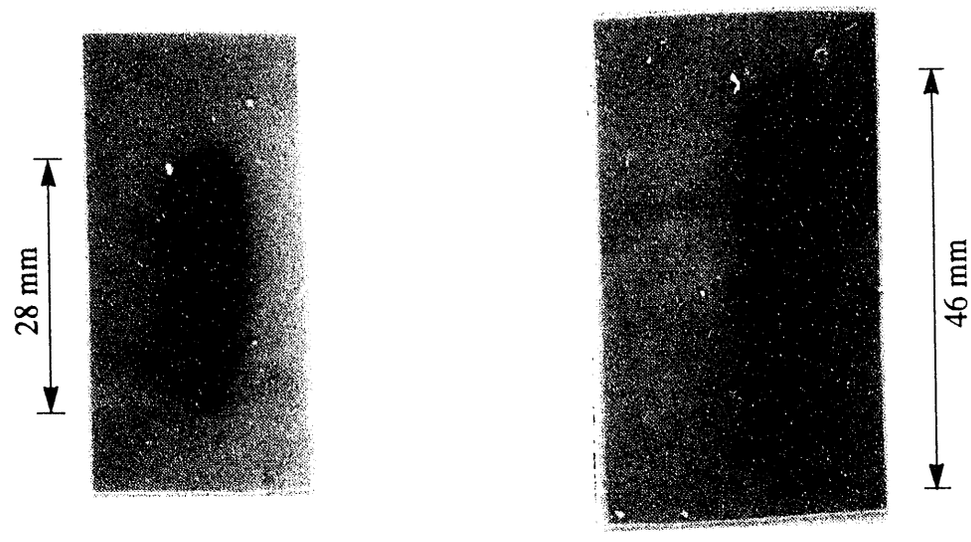

Figure 2. Radiographic images from Test 5 illustrating the general fragmentation character observed in the majority of experiments in the present study. (Time interval between images: 33.2 μs.)

the images were made. Corrections are made for magnification and parallax in the radiographic measurement. A more detailed table of timing measurements is included in Appendix A.

As noted earlier, axial dispersion of the fragment debris is small. The axial extent for all of the tests is not more than several sphere diameters at the later radiograph image. The induced radial expansion velocity, V_e, is substantial, however, and varies systematically with initial impact parameters. V_e represents the radial velocity of the outer fringe of the fragment cloud from the center-line and is determined from the change in diameter of the successive radiographic images. Although an errant fragment at the cloud fringe can lead to a degree of subjectivity, the expansion velocity is determined with an accuracy of about ± 20 m/s. In a few cases, at the higher impact velocities, data scatter was somewhat larger. In three experiments (Test 19, Test 23, and Test 24) the fragment debris pattern included a sparse spray of high velocity peripheral fragments. For these tests, radial expansion velocities in Table 2 represent the extreme of spray fragments observed on the radiographs. In three experiments (Test 10, Test 11, and Test12) the impulse to the steel ball was insufficient to induce an expansion velocity.

Fragment Size and Number Measurements Through Radiographic Diagnostics and Image Processing

The x-ray image of a cloud of fragment debris produced in a high-velocity impact event produces a shadow-graph of the resulting fragments. The total number of fragments and the average fragment size are important items of data in such an experiment. This data is difficult to

Table 2: Kinematic Properties of the Debris

Test	V_i	ΔV	V_e	V_r	Test	V_i	ΔV	V_e	V_r
#	m/s	m/s	m/s	m/s	#	m/s	m/s	m/s	m/s
1	4460	a	a	a	13	4430	460	290	3970
2	?	a	a	a	14	4060	330	183	3730
3	4450		200		15	3310	240	50	3070
4	4700	150	147	4550	16	4080	330	164	3750
5	4570	270	271	4300	17	4520	195	223	4325
6	3460	200	52	3260	18	4430	345	219	4085
7	4160	250	171	3910	19	4610	410	660[c]	4200
8	3950	130	105	3820	20	4040	295	158	3745
9	3460	170	44	3290	21	3750	270	82	3480
10	3410	50	0	3360	22	4700	85	72	4615
11	3920	60	0	3860	23	4060	785[b]	580[c]	3275
12	4470	90	0	4380	24	4030	680[b]	540[c]	3350

[a] Oblique angle radiograph — parameters not determined.
[b] Velocity of debris cloud front.
[c] Diffused

extract from radiograph records, however, because of the overlap and shadowing of fragments which occur if sufficient spreading of the fragment debris is not allowed before x-ray imaging. The latter solution is often inconsistent with other objectives of the radiographic diagnostics. For example, preliminary examination of the images shown in Figure 2 for Test 5 indicates about 200 particles, with an average fragment size of about 1 mm and a largest fragment size of about 2 mm.

A useful method for extracting fragment number and average fragment size data from radiographs of reasonable tightly packed fragment debris clouds is based on a statistical formula for randomly positioned areas (Johnson and Mehl, 1939). The approach can be conceptualized by imagining coins of various sizes which are tossed and land at random positions on a table of a specified area A_{reg}. After N coins have been thrown the total area of interest A will be the sum of the areas of the N coins. The area of the table that is covered, however. will be less because of overlapping due to the random placement of the coins. If the area covered is A_{obs}, then the statistical theory leads to a relation between the observed area A_{obs} and the actual area A of the N coins randomly distributed on the region A_{reg},

$$A = A_{obs} \ln (1 - f)^{-1/f}, \qquad (1)$$

where $f = A_{obs}/A_{reg}$ is the fraction of the region (table) covered by coins. A Taylor expansion of Equation 1,

$$A = A_{obs}\left(1 + \frac{f}{2} + \frac{f^2}{3} + \cdots\right), \tag{2}$$

reveals that A is always greater than A_{obs} and approaches A_{obs} as f becomes small.

Application of the statistical relation in Equation 1 or Equation 2 to radiographs of fragment debris is reasonably clear. Because of shadowing and overlap of fragments in the relatively dense debris cloud, the fragment area projected on the radiographic image will be less than the projected area of the same fragments if shadowing and overlap does not occur — the latter being the desired property. Thus, image processing of the radiographic record requires two measured properties — the total observed projected fragment area A_{obs}, and an estimate of the area fraction of the debris cloud region masked by the debris fragments. Assuming a random distribution of fragments through the region, Equation 1 provides the required projected fragment area. Note that if f is reasonably small the expression for A is relatively insensitive to inaccuracies in f.

Knowing the total volume of fragmented material within the debris cloud, the number of fragments N and the average fragment size S are related through $V = NS^3$. In addition the total projected area satisfies $A = NS^2$. Solving these relations provides the average fragment size,

$$S = V/A, \tag{3}$$

and the total fragment number,

$$N = A^3/V^2. \tag{4}$$

The above procedure was used to analyze the majority of the fragment debris radiographs in the present study and extract experimental fragment size and number data. The image-processed records are included in Appendix B and provide a documented record of the radiographic images obtained in the present work. The figures in Appendix B also indicate the areas (A_{reg}, A_{obs}) used in the above analysis. Results for all fragment debris radiographs are tabulated in Table 3, including both average fragment size and number calculated from Equation 3 and Equation 4.

Table 3: Fragment Size and Number Results from Image-Processed Radiographs

Test #	A_{obs} mm^2	f	A mm^2	N	S mm	Test #	A_{obs} mm^2	f	A mm^2	N	S mm
1	168.4	0.287	198.5	435	0.67	15b	52.1	0.361	64.7	15	2.07
2	108.3	0.069	115.6	86	1.16	16a	93.3	0.519	131.5	127	1.02
3	92.4	0.438	121.5	100	1.10	16b	118.6	0.274	138.5	148	0.97
4a	275.4	0.503	142.6	161	0.94	17a	92.1	0.469	124.3	106	1.08
4b	119.0	0.274	139.1	150	0.96	17b	134.7	0.273	157.4	216	0.85
5a	117.1	0.582	175.5	301	0.76	18a	89.3	0.587	134.6	136	1.00
5b	160.3	0.379	201.5	455	0.67	18b	114.1	0.283	134.2	134	1.00
6a	65.4	0.572	97.0	51	1.38	19a	93.1	0.386	117.6	90	1.14
6b	73.8	0.337	90.0	40	1.49	19b	102.0	0.150	110.7	76	1.21
7a	110.2	0.593	167.0	259	0.80	20a	95.3	0.591	144.2	167	0.93
7b	155.4	0.412	200.3	447	0.67	20b	123.3	0.389	156.2	212	0.86
8a	65.2	0.615	101.3	58	1.32	21a	73.5	0.623	115.0	85	1.17
8b	95.7	0.420	124.1	106	1.08	21b	116.2	0.449	154.3	204	0.87
9a	44.3	0.664	72.8	22	1.84	22a	64.6	0.581	96.7	50	1.39
9b	61.6	0.565	90.7	41	1.47	22b	99.3	0.421	128.8	119	1.04
13a	83.3	0.607	128.2	117	1.04	23a*		0.			
13b	124.3	0.361	154.2	203	0.87	23b	166.2	0.084	173.6	291	0.77
14a	80.0	0.565	117.9	91	1.14	24a	116.2	0.308	138.9	149	0.97
14b*	83.6	0.366	104.1			24b	122.2	0.105	128.0	117	1.05
15a	44.8	0.576	66.7	17	2.01						

* Partial radiograph

The fragment size and number data are plotted in Figure 3 and Figure 4, respectively, as a function of the radial expansion velocity for that experiment provided in Table 2. The experiment numbers are used as data symbols in Figure 3 and Figure 4. For the experiment in which two radiographs of the debris cloud were obtained both points are plotted.

Uncertainties in the present analysis can arise from several sources. The estimate of A_{reg} which encloses the fragment cloud has some subjectivity. This measure effects the value of f, but

Test 21, Radiograph b ~

10 mm

6.35 mm Steel Sphere Impact Velocity: 3750 m/s
PMMA Target Thickness: 4.78 mm

Figure B35. Test 21, Radiograph b.

its influence on the final S and N values is small if f is small. One can readily see other image-processing methods for estimating f but they were not pursued. The image-processing method used to determine A_{obs} requires an edge-selection criterion and further uncertainties can be introduced in this procedure. In retrospect this uncertainty could be reduced by calibration of the edge-selection method on a radiograph of particles of known size.

The fragment size data are fairly clearly represented in Figure 3: the average fragment size is relatively constant above expansion velocities of 150 m/s.The level of scatter probably reflects the uncertainties mentioned above. The fragment number data in Figure 4 reflect a similar insensitivity to expansion velocity above 150 m/s. The data for Tests 5 and 7 clearly fall outside of the trend in this plot. The reasons for this behavior are not yet understood.

C. Analysis of the Steel Debris

It is apparent from the radiograph in Figure 2 that the impulse imparted to the steel sphere by the PMMA plate partitions the initial kinetic energy of the steel sphere into kinetic energies of axial translation and radial expansion of the steel fragments, kinetic energy of the PMMA debris, and energy expended in the various dissipative processes active during the impact process. The axial velocity change, ΔV, recorded for the experimental series in Table 2, provides a measure of the translational momentum loss by the steel sphere upon impact. These results are plotted against the product of the PMMA plate thickness and the steel sphere impact velocity, hV_i, in Figure 5. This latter parameter provides a measure of the impulse delivered to the sphere by the PMMA target. Within experimental scatter, the ΔV data are found to be a single-valued function of the parameter hV_i.

Translational Impulse Analysis

The trend of the data in Figure 5 can be reasonably well understood in terms of a relatively basic hydrodynamic description of the sphere and target interaction (*e.g.* Backman and Goldsmith, 1978). The acceleration of the steel sphere of mass m, is determined from,

$$m\frac{dV}{dt} = \frac{1}{2}\rho V^2 A, \qquad (5)$$

where $\rho V^2/2$ is the Bernoulli pressure applied by the PMMA target material, of density ρ, under steady flow conditions, and is assumed to apply over the projected geometric area A of the sphere. The velocity V is the equilibrated velocity of the PMMA and the steel sphere. The relatively low target impedance of PMMA compared with that of the steel projectile permits this approximation. Integration of Equation 5 leads to a predicted exponential change in projectile velocity with plate perforation thickness. For target plate thicknesses h on the order of the sphere diameter, a first order solution of Equation 5 provides the functional relationship of the decrease in velocity with the impact velocity and target thickness,

$$\Delta V = \frac{\rho A}{2m} hV_i. \qquad (6)$$

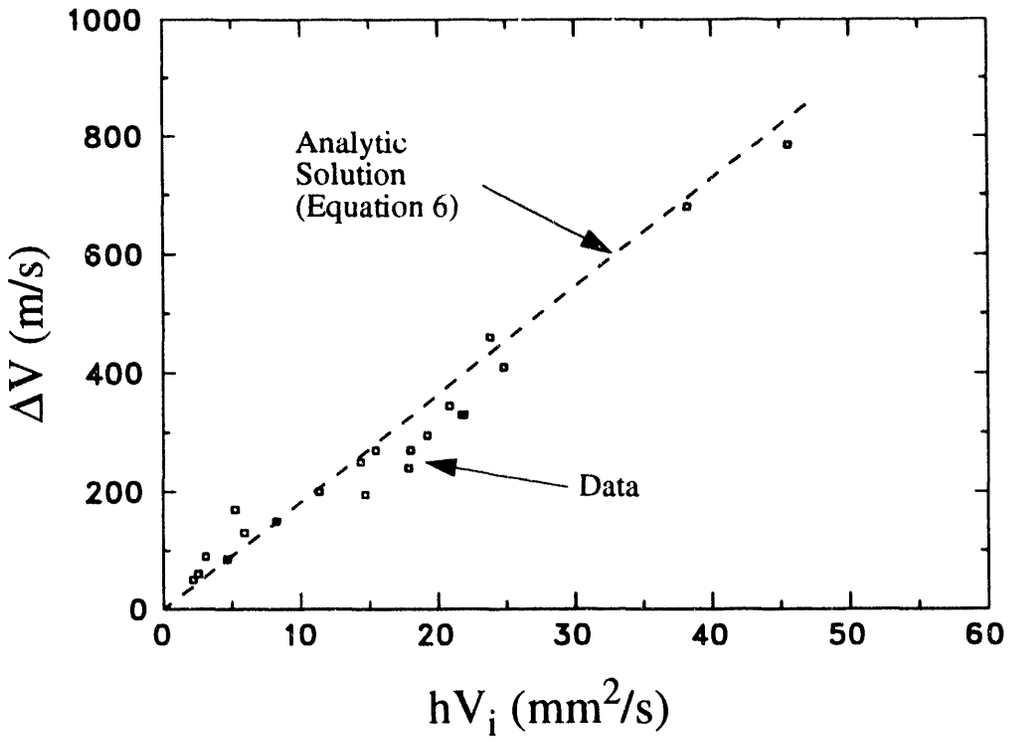

Figure 5. Translational velocity reduction data. Dependence on product of target plate thickness and impact velocity.

Comparison of Equation 6 with the measured velocity decrease data, tabulated in Table 2, is shown in Figure 5, and demonstrates excellent agreement.

Fragment Debris Pattern

In the preponderance of experiments performed, the fragment debris stayed closely grouped or clustered. There was a well-defined region in space within which fragment density was high and a sharp gradient outside of which no fragments were found. This description readily carries over to the characteristics of the impact footprint on the secondary impact plate (see later Sections). In these tests the radial expansion velocity defined previously was relatively easy to establish.

Interesting features are also observed in the radial expansion characteristics of the steel fragment debris following target impact. Several distinct regions of behavior were noted to occur within the parameter range of the present study. First, impulses below which there was no radial expansion of the steel spheres were observed in three experiments performed on target plates approximately 0.6 mm in thickness. The steel sphere remained intact at impact velocities of 3400 and 3900 m/s. A small fragment was spalled off the rear surface of the sphere at a velocity of 4500 m/s.

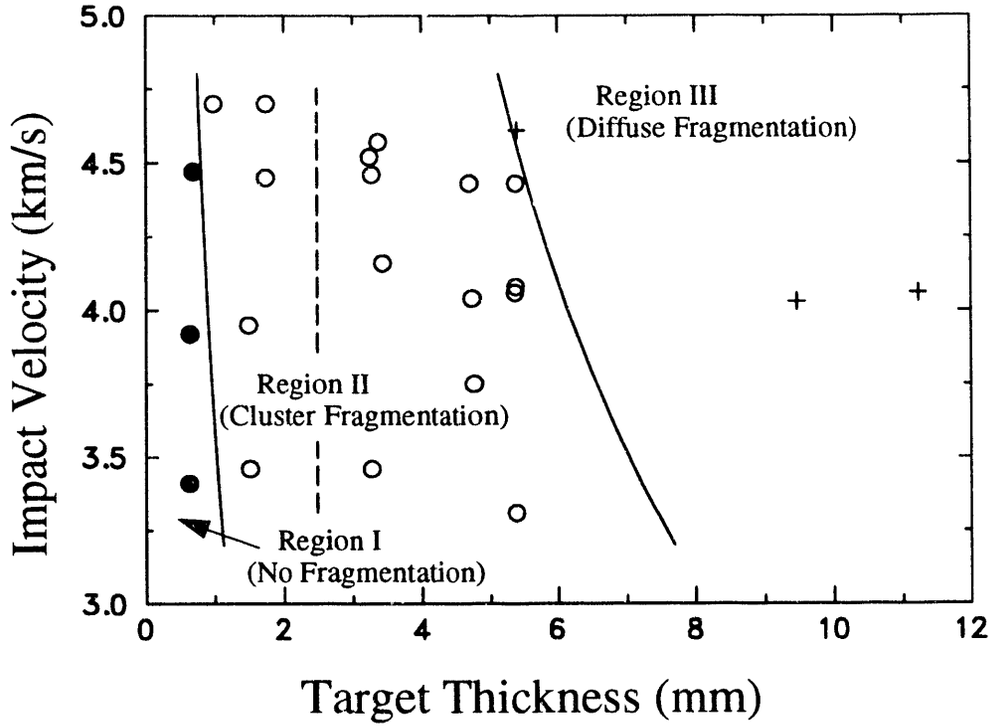

Figure 6. Plot of impact velocity versus target thickness. Different regions of fragment debris characteristics are identified and separated by iso-impulsive curves. The vertical dashed line separates distinct fragment pattern differences in Region II (see text).

One of several possible representations of debris formation data is provided in Figure 6. Points identify the impact velocity and the target plate thickness, on the vertical and horizontal axes, respectively, the product of which provides an approximate measure of the impulse imparted to the steel sphere. Curves of constant impulse are used to identify boundaries between three regions of behavior in the fragmentation process: Region I - No Fragmentation; Region II - Cluster Fragmentation; and Region III - Diffuse Fragmentation. In Region I, the impulse was insufficient to cause fragmentation. Region II identifies the tests in which fragment debris was clearly clustered in the sense described previously. Within this cluster region, two fairly distinct patterns were observed in the debris cloud; they were most likely a consequence of the target plate thickness relative to sphere diameter. For plate thicknesses less than about 2 mm, distinct spall debris from the back of the sphere leads to some axial divergence and a shallow conical shape to the debris pattern (for example Test 4 and Test 8). For plate thicknesses closer to the sphere diameter (3 to 6 mm) a distinct plate or disc shape is observed for the debris pattern.

Also appearing in Region II are two experiments (Test 1 and Test 2) in which an oblique x-ray orientation was used (47 ± 2 degrees from the shot line) to establish how fragments were distributed through the diameter of the debris disc. The radiograph for Test 2 is shown in Figure 7. The debris is moving obliquely away from the point of observation. The radiograph establishes that

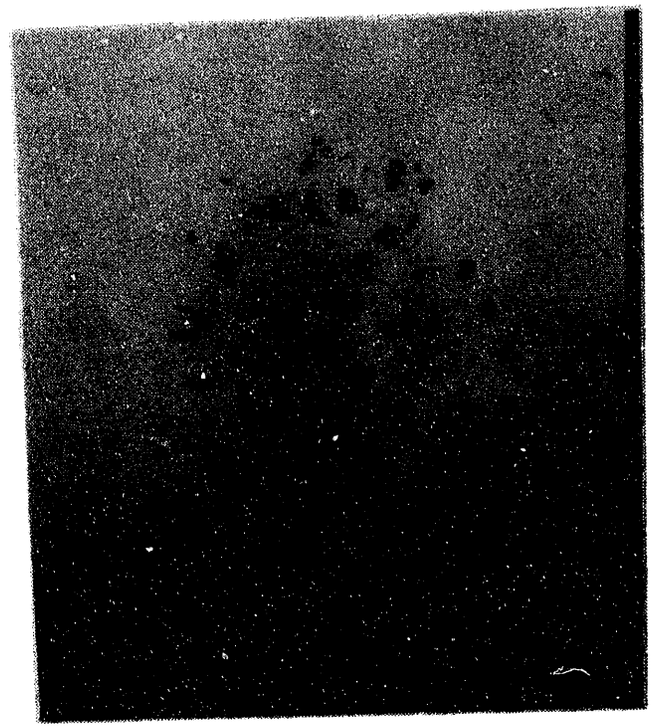

Figure 7. Radiograph of steel debris using oblique x-ray diagnostics (Test 2). Note the continuous spatial distribution of the fragments.

fragment debris is in fact distributed fairly uniformly through the diameter, and a distinct regular structure in the pattern of the peripheral fragments is observed.

Finally, a clear transition in debris characteristics was observed in several tests in which parameter extremes were achieved (Region III). The impact velocity in Test 19 was in excess of 4600 m/s for the steel sphere on a 5.4 mm plate, and the spheres in Test 23 and Test 24 impacted at slightly lower velocities on plates in excess of 9 mm in thickness. Rather than an abrupt transition in the fragment density, as observed in Region II, there is a more gradual thinning in the density toward the cloud perimeter. The perimeter fragments in Region III have significantly higher expansion velocities (see Table 2) than those achieved in Region II. The debris pattern was umbrella shaped with perimeter fragments lagging behind the central cloud.

It is speculated that sufficient impulse has been achieved in the Region III tests to trigger incipient jetting of material from the sphere-plate contact zones. Jetting could account for the excessive radial velocity and trajectory of this part of the fragment debris, however this conjecture has yet to be verified.

Radial Expansion Velocity

For the tests which have Region II behavior for their fragment debris pattern, expansion velocity data from Table 2 are plotted as a function of impact velocity, as shown in Figure 8. In this graph, tests of nominally the same plate thickness are identified by a common symbol. Although data scatter tends to obscure detailed trends, some observations can be made. First, at similar impact velocities, the expansion velocity increases with increased plate thickness but becomes less sensitive to plate thickness. This trend is most noticeable at the higher impact velocities. Second, there is a critical impact velocity below which fragmentation and subsequent expansion do not

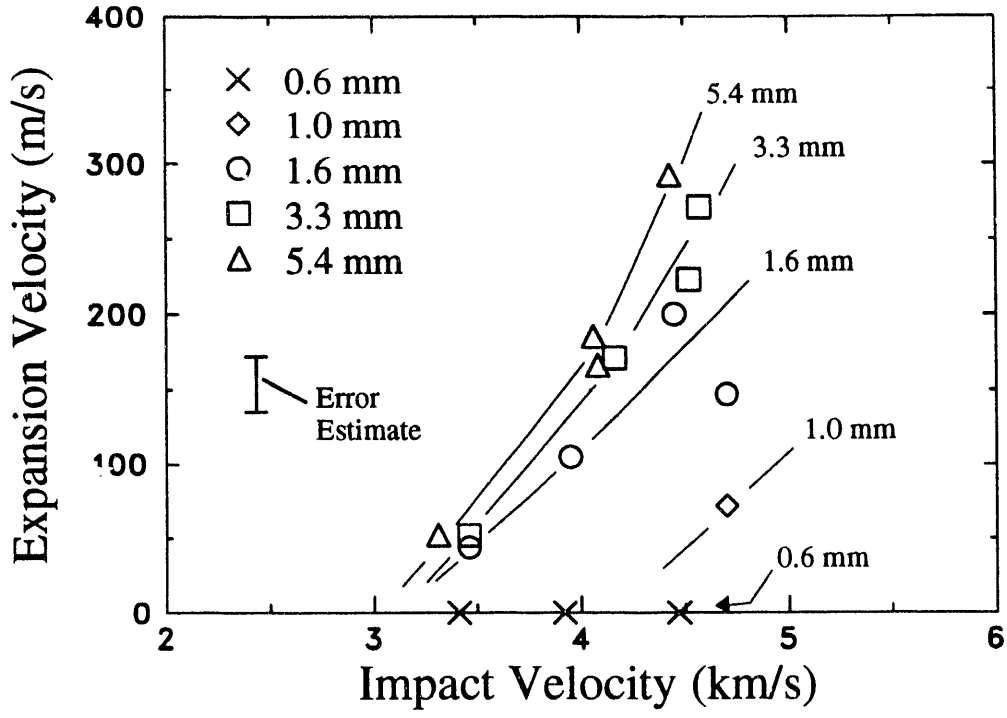

Figure 8. Radial expansion velocity of fragment debris. Tests with nominally similar target-plate thicknesses are plotted against the impact velocity.

occur. This velocity limit is outside of the range of the data for the 0.6 mm plate and is probably around 4000 m/s for a 1.0 mm plate. For thicker plates (1.6 mm and above) this critical velocity (about 3000 m/s) becomes independent of plate thickness, as found by extrapolating to zero expansion velocity in Figure 8.

In Figure 9, an alternative representation of the expansion velocity data is shown. Expansion velocity is plotted against plate thicknesses at nominally similar impact velocities. Increased expansion velocity with increasing impact velocity is seen. Flattening of the curves for plate thicknesses above about 2 mm is clearly observed.

Shock Coupling Analysis

The translational impulse imparted to the fragment debris appears to be a consequence of the momentum exchanged during hydrodynamic penetration of the target plate. This conclusion is supported by the nearly linear dependence on plate thickness, in agreement with the analytic expression given in Equation 6 and our numerical computations to be described later. In contrast, the evidence displayed in Figure 8 and Figure 9 would suggest that radial impulse acquired by the impacting sphere is a consequence of the early shock phase of the interaction and is little affected by the later hydrodynamic penetration phase.

To explore this supposition we will examine a conceptual theory of the shock interaction event and compare implications with the observed trends in the expansion velocity data. Because

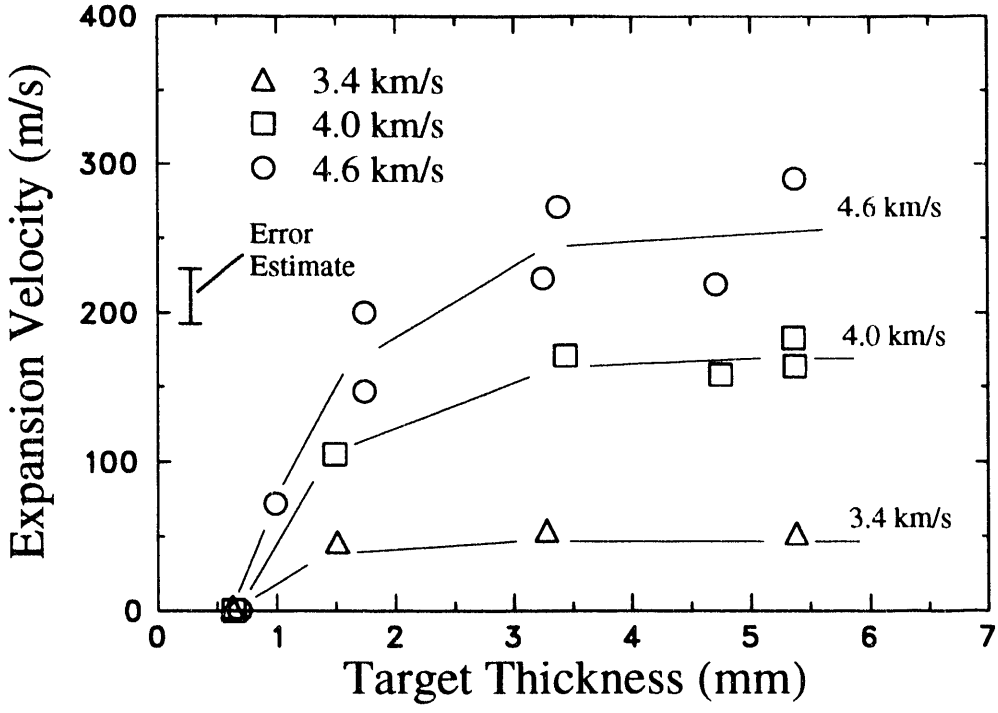

Figure 9. Radial expansion velocity of fragment debris. Tests at nominally similar impact velocities are plotted against target plate thickness.

of the spherical geometry of the impacting projectile, the coupling of shock energy into the projectile is transient and constrained to the central impact surface of the projectile. An analysis of the impact conditions due to Ang (1990) can be used to calculate duration and magnitude of the coupled shock energy.

Referring to the geometry illustrated in Figure 10, for a spherical projectile undergoing normal impact at a velocity V_i on a planar surface, the distance of the collision point from the centerline at time t is,

$$a = V_i t \sqrt{\frac{2R}{V_i t} - 1}. \tag{7}$$

The velocity of the collision point is provided by the derivative of Equation 7,

$$\dot{a} = \frac{V_i \left(\frac{R}{V_i t} - 1\right)}{\sqrt{\frac{2R}{V_i t} - 1}}. \tag{8}$$

The collision velocity is initially infinite and decreases with time. As curvature of the impacting sphere at the contact point increases, the collision velocity will continue to decrease

(Figure 10a), ultimately allowing a lateral release wave to propagate inward and quenching the shock coupling phase (Figure 10b).

A reasonable assumption is that shock waves will couple into both materials over the lateral distance at which $\dot{a}$ reduces to the release wave velocity in the faster material. We will approximate the release velocity by the shock velocity U_{s1} in the faster material. (Release waves are dispersive but U_{s1} is approximately equal to the release velocity at one-half of the Hugoniot particle velocity in a linear shock velocity - particle velocity material.) The time t_1 at which $\dot{a} = U_{s1}$ is calculated from Equation 8 through,

$$U_{s1} = \frac{V_i\left(\frac{R}{V_i t_1} - 1\right)}{\sqrt{\frac{2R}{V_i t_1} - 1}}. \tag{9}$$

The corresponding radius at this time is provided by Equation 7,

$$a_c = V_i t_1 \sqrt{\frac{2R}{V_i t_1} - 1}. \tag{10}$$

The release time t_2 is in turn calculated from the radius a_c and the release velocity (shock velocity U_{s1}) in the faster material through,

$$t_2 = a_c / U_{s1}. \tag{11}$$

The axial thickness b_c of the shock pulse in the projectile (see Figure 10b) is then determined from,

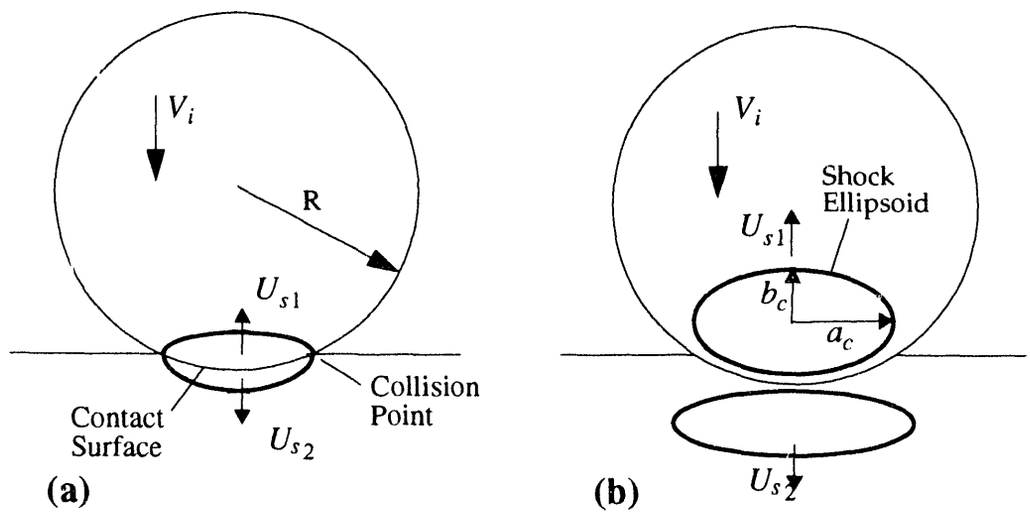

Figure 10. Geometry of shock-wave coupling upon normal impact of a spherical particle on a planar surface.

$$b_c = \frac{1}{2} U_{s1} (t_1 + t_2) . \qquad (12)$$

A reasonable estimate of the region of shock coupling into the projectile is an ellipsoidal volume with major axis a_c and minor axis b_c. Hence the coupled shock energy (kinetic and internal) is provided by the volume of material times its energy density,

$$E_s = \frac{4\pi}{3} a_c^2 b_c \frac{p_h^2}{\rho U_{s1}^2} . \qquad (13)$$

The shock energy provided by Equation 13 is necessarily approximate due to the simplification needed to complete the analytic solution. Also, there is not a clear transition time between the shock and the steady hydro-phases of penetration. Nevertheless, comparisons of Equation 13 with wave-code simulations (see later Sections) of spherical impact on planar surfaces have shown reasonably close agreement (within about 25%).

A portion of the shock energy coupled into the projectile will be dissipated in shock heating. This heat energy is calculated to be about 10% of the shock energy at the present impact amplitudes. Momentum conservation requires that a portion of the shock energy also be converted into kinetic energy associated with axial motion. This energy is also about 10% of the total shock energy. Most of the shock energy will go into plastic distortion of the projectile and radial kinetic energy of fragments if the impact is sufficiently intense.

Carrying through the analysis needed to calculate the shock energy from Equation 13 for a 4600 m/s impact velocity, and reducing this value by the required heat and axial kinetic energies provides an energy available for radial expansion of about 33 J. If we assume that this energy is fully coupled into the uniform radial expansion of a uniform disc of fragment debris (K.E. = $mV_r^2/4$), an expansion velocity of V_e = 360 m/s is calculated. Comparison with the appropriate expansion data in Figure 11 (see also Figure 9) finds the calculated value somewhat higher than the data.

Although approximations in the analytic solution could probably encompass the observed difference between calculation and experiment, it is, nevertheless, worthwhile attempting to account for energy absorbed in the fragmentation process to assess the expected level of influence on the calculated expansion velocity. First, energy to create fragment surface area can be expected to reduce the radial kinetic energy. For a fracture toughness of K_c = 35 MPa$\sqrt{m}$, a fracture surface energy from $\Gamma = K_c^2/2E$ is calculated to be about 3830 J/m^2. At an impact velocity of 4600 m/s a total number of about 100 fragments can be calculated, or estimated from the radiographs. For this degree of fragmentation, a fragment surface energy of 2.8 J is calculated. Reducing the 33 J expansion energy by this amount leads to a slightly lower expansion velocity of V_e = 343 m/s (see Figure 11).

Static tensile tests on the present steel provide a strain to failure of $\varepsilon_f \approx 0.05$ (5%). Assuming a similar strain to failure under the dynamic conditions of the impact fracture process, a strain-to-failure energy, $E_f = Y\varepsilon_f$, (Y = 2 GPa is the yield stress) provides an additional fracture energy

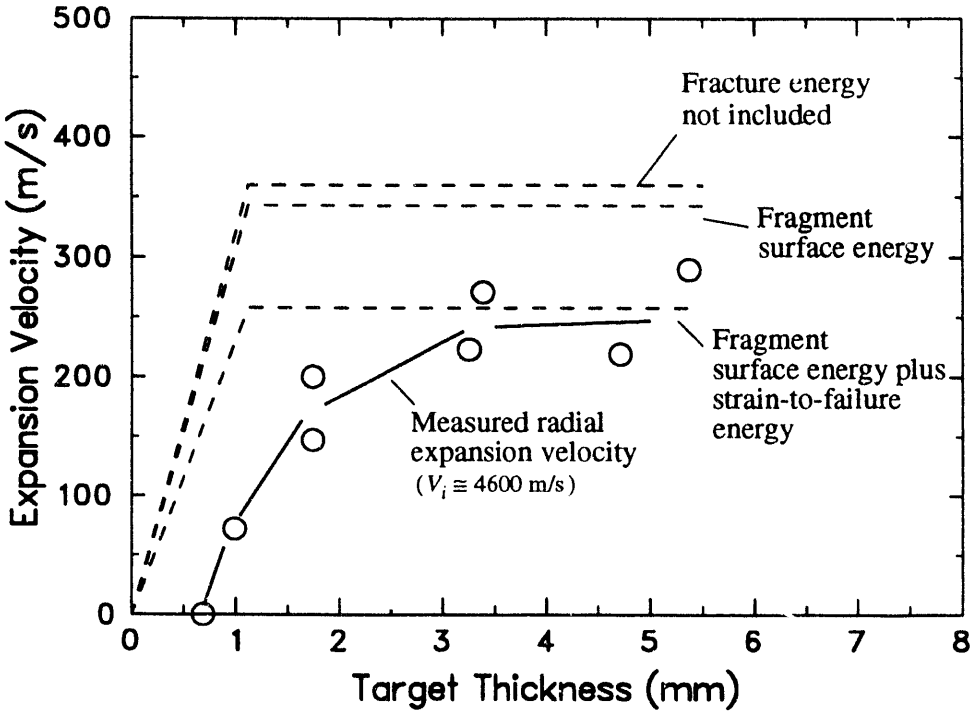

Figure 11. Comparison of calculated and measured radial expansion velocities for debris fragments at 4600 m/s impact velocity.

of 13.1 J. Accounting for both fracture surface energy and strain-to-failure energy further reduces the expansion velocity to V_e = 258 m/s. It is interesting to note from the radiographic record for Test 12 that this projectile indicates a plastic distortion of about 5% without fragmentation.

As noted earlier the shock energy is coupled into the spherical projectile in a time $t_1 + t_2$ (see Equation 9 to Equation 12). This time requires that the target plate be thicker than $U_{s2}(t_1 + t_2)/2$ where U_{s2} is the shock velocity in the target material. For an impact velocity of 4600 m/s this thickness is calculated to be approximately 1.1 mm. Thinner target plates would lead to reduced shock energies and radial expansion velocities as is indicated by the linear decrease for thickness below 1.1 mm in Figure 11. In contrast, target plates thicker than 1.1 mm would not increase the coupled shock energy and the expansion velocity would be independent of increasing plate thickness. This predicted behavior roughly approximates the observed behavior (Figure 11).

Debris Cloud Expansion Analysis

Considering the level of approximations adopted in achieving an analytic solution to the radial expansion characteristics of the Region II fragment debris, the agreement is certainly better than can be expected. Nevertheless, the agreement between trends and rough magnitudes tend to support the premise that the radial expansion and dominant fragmentation characteristics of the debris pattern are established earlier in the interaction by the shock aspect of the impact, and are only weakly effected by the later hydrodynamic loading portion on the projectile.

An alternative approach relating the debris cloud expansion velocity to the impact velocity has been taken by Lawrence (1992). In this analysis, hypervelocity impact of particles onto a target is assumed to result in perforation of the target. A non-dimensionalized impact velocity is determined that is dependent upon geometric parameters and the expansion angle, θ, of the debris cloud behind the target plate. The geometric non-dimensionalized variable is

$$M = \frac{h\rho_{target}}{D\rho_{ball}} \times \frac{3}{2}\beta^2, \qquad (14)$$

where h is the target thickness, ρ_{target} is the target material density, D is the spherical particle diameter, ρ_{ball} is the material density of the sphere, and β is the ratio of hole diameter to sphere diameter, set equal to 1 in this case. The angle of the debris divergence, θ, is determined from $\theta = arc\sin(V_e/V_r)$, where V_e is the debris cloud expansion velocity and V_r is the debris cloud translation velocity. The non-dimensionalized impact velocity, V_p, is determined from

$$V_p = \frac{(1+M^2)}{M-(\sin\theta)^2}. \qquad (15)$$

Data from Table 2 are used to calculate the experimental values of M and V_p for each experiment, and these are plotted in Figure 12. The experimental data are grouped into three separate ranges of expansion angle: 0.7 - 3°, 3 - 5°, and 9 - 11°. The theoretical curves for θ = 0, 5, and 10 degrees compare very well with the available data. The most extensive data is for the lower angles of debris divergence (Tests 4, 6, 7, 8, 9, 14, 15, 16, 17, 20, 21, and 22). The three points in the 9 - 11° range (Tests 19, 23, and 24) fall right on the 10° curve, and the three data points in the 3 - 5° range (Tests 5, 13, and 18) fall just below the 5° curve. (Note in Table 2 that expansion data is unavailable for Tests 1, 2, and 3, and that the expansion velocity is zero for Tests 10, 11, and 12.) Note also that β is not constant, varying between 1.2 and 1.6 for these data.

D. Target Crater Characteristics

Although a study of the PMMA target crater formation process was not a primary objective in the present investigation, the results were noteworthy and warrant some discussion. A number of the target plates were seriously shattered due to the primary or subsequent impacts within the target tank. Consequently, a systematic examination of all the data was not possible. Nevertheless, a sufficient number of plates survived to reveal characteristic trends of the crater geometry.

The target plate from Test 19 remained intact after the test and a photograph of the impact crater region is shown in Figure 13. The crater characteristics observed in Figure 13 are representative of all of the tests with the exception of those experiments in which very thin plates were used. These latter include tests 10, 11 and 12 which used 0.6 to 0.7 mm thickness plates. In these tests simple punch-through left a hole only slightly over projectile diameter and no collateral crater damage was observed. A transition to the cratering behavior seen in Figure 13 occurred with the 1.0 mm plate used in Test 22 and for all thicker plates.

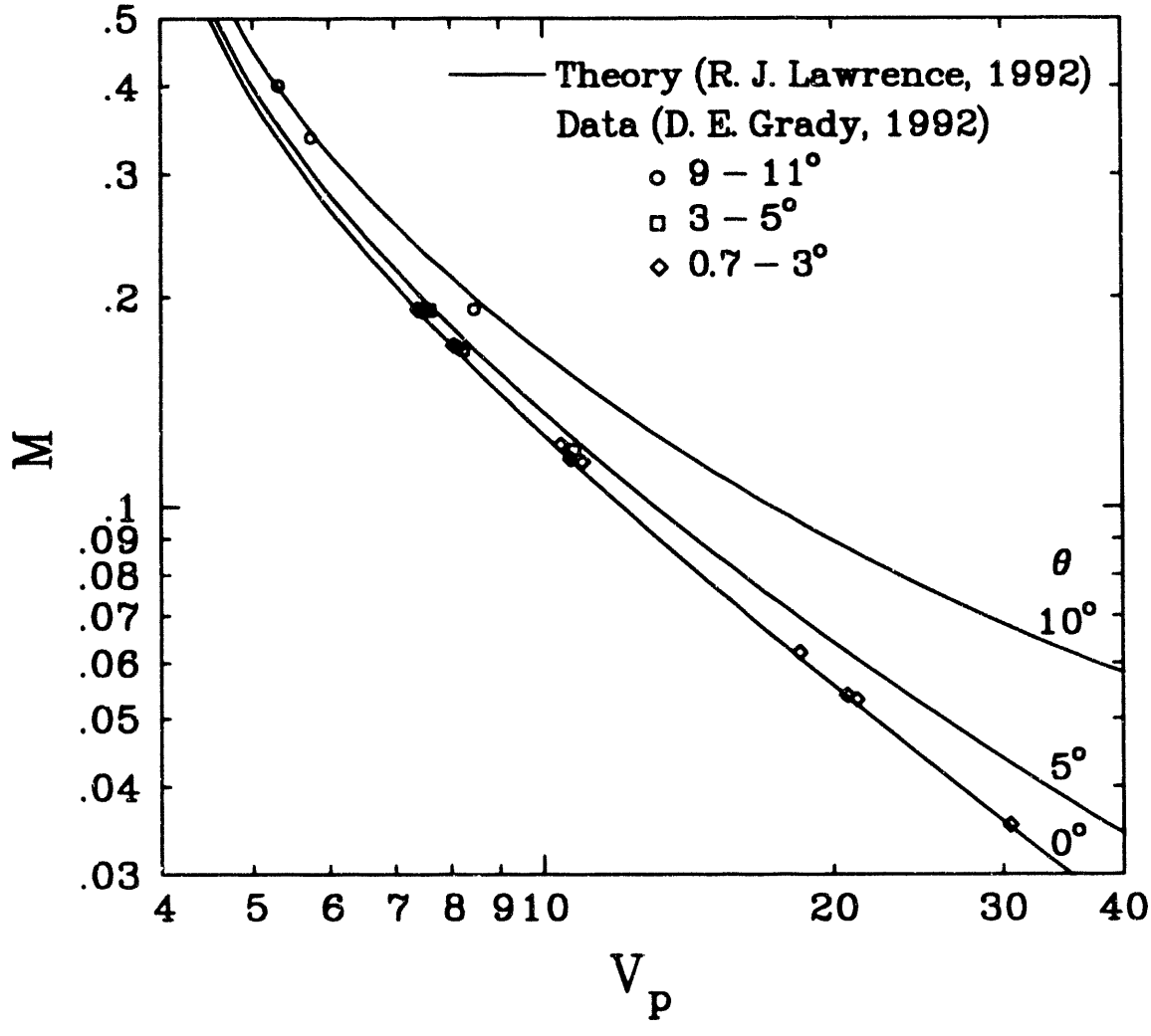

Figure 12. Comparison of steel debris expansion velocities with theory of Lawrence (1992)

In all tests the physical hole left in the PMMA target plate after the penetration process was never larger than 10 mm in diameter and was usually somewhat less. The hole diameter for Test 19 (Figure 13) was about 8 mm. (Recall that the projectile sphere was 6.35 mm in diameter.)

The concentric radial spall region on both the front (impact) and back (exit) of the target plate was the most striking feature of the impact crater. The diameter of the spall crater was slightly larger in front than in back. A sharply-defined circular spall lip was observed on the front crater. The spall lip of the exit crater was more jagged and less uniform. This general character of the spall crater is clearly seen in the photographic results of Test 19 in Figure 13. An interior hackle or crazed region in the PMMA was observed to extend a few millimeters beyond the radius of the spall lip - representing further interior spall without material break-away. Finally a collection of 15 to 25 irregular spoke cracks extending radially outward another 10 to 30 mm completed the

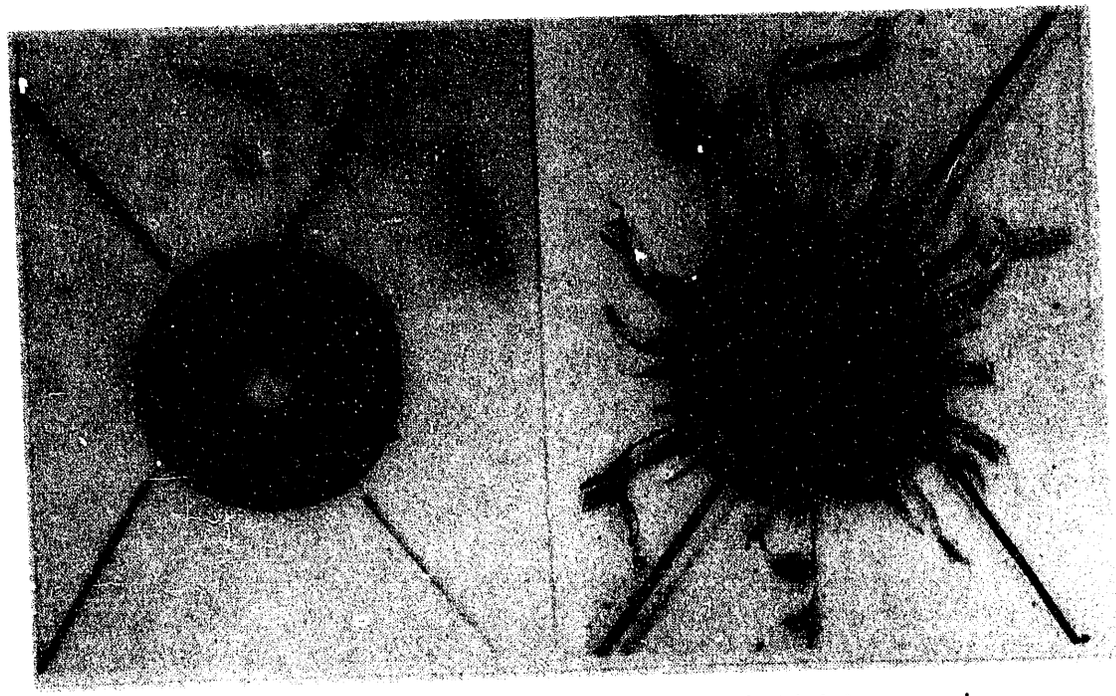

Figure 13. Photographs of the impact (left) and exit (right) craters in the PMMA target plate for Test 19. Plate thickness = 5.39 mm and impact velocity = 4.61 km/s.

collateral crater damage effects. Propagation of several of these cracks to the plate edge caused breakup of most of the target plates.

Some systematics were extracted from the target crater data. First, the diameter of the radial front spall zone was found to be relatively insensitive to changes in the impact velocity over the range studied (~ 3.3 to 4.7 km/s) for target plates of similar thicknesses. Diameters were 20 and 23 mm, respectively, for Tests 6 and 17, and 33 and 34 mm, respectively, for Tests 15 and 19.

On the other hand, a clear dependence of the front spall crater diameter on target thickness was observed. All tests for which a spall crater diameter could be measured are plotted in Figure 14. The data include impact velocities over the range of 3.3 to 4.7 km/s. A linear increase in crater diameter with plate thickness up to thicknesses approaching 6 mm was observed. This linear trend is not continued for the two thicker plates.

E. Summary of Fragmentation Theory and Code Implementation

A capability has been developed to produce fragment size predictions from calculations using wave propagation codes that solve the equations expressing conservation of mass, momentum, and energy for a continuum. Although plots produced from standard wavecode calculations sometimes appear to depict a collection of discrete fragments, the physical mechanisms that control these processes, such as surface tension or real physical heterogeneities and microstructure, are not currently included in the codes. It is not feasible for continuum mechanics wavecodes, except perhaps in one dimension (Kipp and Grady, 1985), to account for the complete, explicit formation of discrete fragments. But extensive work has demonstrated that continuum models of various

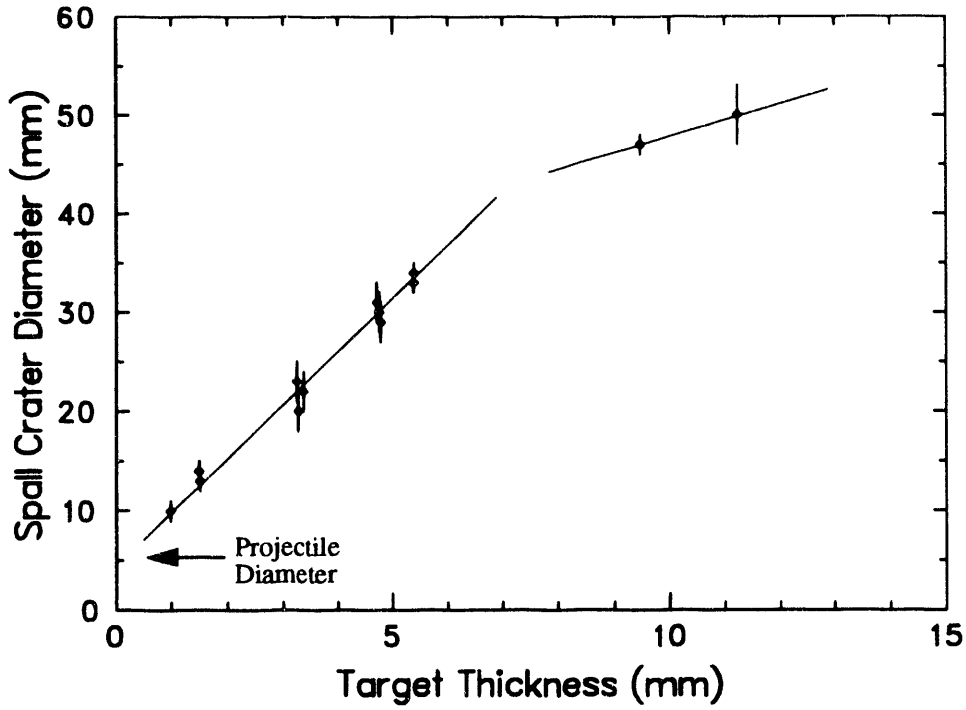

Figure 14. Front (impact side) spall-crater diameter data. Impact velocities ranged from 3.3 to 4.7 km/s.

levels of sophistication can successfully address the damage processes of void and crack growth leading to material failure (*e.g.* Grady and Kipp, 1989).

Previous work (Grady, *et al.*, 1990b) has produced dynamic fragmentation theories that are based on the assumption that strain rate and temperature at the time of failure control subsequent fragmentation. Considerable progress has been made in extracting this information from Lagrangian wavecodes (Grady, *et al.*, 1990b; Johnson, *et al.*, 1990), which are excellent at tracking the history associated with each material element and can easily save the required information at the time of fracture. It is a much more difficult task for an Eulerian wavecode to maintain accurate values of this information because of the degradation accumulated by the repetitive rezoning used in the convection process. However, the extensive deformation associated with these impact and penetration events encourages the use of an Eulerian wave propagation code.

The wavecode that was used for the calculations was the Eulerian finite-difference shock wave propagation code CTH (McGlaun, *et al.*, 1990). This code has a general internal state variable capability which allows information to be saved in variables that are advected with the material as it crosses the cell boundaries. Significant modifications were made to the fracture algorithm in the code to locate each time and position at which the tensile stress criterion for a single material, rather than a mixed-material cell, was exceeded and material fracture was judged to occur. All diagonal components of the strain-rate tensor,

$$\dot{\varepsilon}_i = \frac{\partial v_i}{\partial x_i}, \tag{16}$$

including the hoop component in cylindrical coordinates,

$$\dot{\varepsilon}_R = \frac{v_R}{R}, \tag{17}$$

where v_i and x_i are velocity and position components and R refers to radius, were then calculated and the maximum value was stored as an internal state variable. While the internal state variables provide storage locations for the strain rate and temperature information that must be saved from the calculation, there is a problem with diffusion of these quantities as material motion occurs. For instance, even though a calculation may be performed in which only a single fracture of a material cell takes place during the entire calculation, subsequent material motion may result in spurious values of strain rate appearing in all cells through which the material has passed. Fortunately, these values typically have a very small magnitude except in the region of the mesh containing the bulk of the fractured material. However, diffusion does result in some spreading and loss of localization of the fractured material, so extreme care was taken to assess such effects and ensure that reasonable fragment size distributions were obtained. Since most fractures occurred at high strain rates on the order of 10^3 to 10^6 per second, it was possible to discard significantly lower strain rates as having been produced by diffusion. Mass fraction weighting was used to maintain the proper convected amplitudes of the strain rates and temperatures.

Files containing strain rate and temperature at the time of fracture are saved periodically during the simulation of the impact, and these are examined to determine the extent of the fractured regions as time progressed. When the fracture process is complete, the data are post-processed outside the wavecode to produce fragment size distributions. Dynamic fragmentation theories predict an average local fragment size at a given strain rate and temperature, and the number of fragments with this average size is determined by the local mass of the material that fractures. The dynamic fragmentation theories that were used to process the strain rate and temperature information have been described in detail elsewhere (Grady, 1988; Grady, *et al.*, 1990a; Grady, *et al.*, 1990b), and they will only be summarized here. Various types of fragmentation mechanisms have been identified, depending on the strain rate and temperature at fracture. The data can also be used to determine the mass distribution of fractured material in the solid, liquid, and vapor phases.

For the present purposes, the average fragment size S will be determined in three different fragmentation regimes. These are:

(1) solid spall dominated by fracture toughness, for which

$$S = \left(\frac{\sqrt{24} K_c}{\rho c \dot{\varepsilon}} \right)^{2/3}, \tag{18}$$

(2) solid spall dominated by the flow stress, for which

$$S = \left(\frac{1.2 Y}{\rho \dot{\varepsilon}^2} \right)^{1/2}, \tag{19}$$

and (3) liquid spall above the melt temperature, for which

$$S = \left(\frac{48\gamma}{\rho\dot{\varepsilon}^2}\right)^{1/3}. \tag{20}$$

In these equations, ρ is the density, $\dot{\varepsilon}$ is the strain rate, c is the sound speed, γ is a constant value of the surface tension, the temperature and strain rate dependent yield strength, Y, is given by

$$Y = Y_0\left(1 - \frac{T}{T_m}\right)^n \left(\frac{\dot{\varepsilon}}{\dot{\varepsilon}_0}\right)^m, \tag{21}$$

and the temperature dependent fracture toughness, K_c, is given by

$$K_c = K_{c0}\left(1 - \frac{T}{T_m}\right)^{n'} \tag{22}$$

where Y_0 is the reference yield strength, K_{c0} is the reference fracture toughness, T is the temperature, T_m is the melt temperature, $\dot{\varepsilon}_0$ is a reference value of the strain rate (one per second), and n, m, and n' are constants. In the solid regime, the transition from fracture toughness to flow stress dominated spall occurs at a strain rate given by

$$\dot{\varepsilon}_t = \sqrt{\frac{0.003\rho c^4 Y^3}{K_c^4}}. \tag{23}$$

Appropriate material properties were obtained for the steel sphere for the fragmentation regimes of brittle, ductile, and liquid spall, as shown in Table 4. Application of the above formulas

Table 4: Fragmentation Material Properties

	Hard Steel
Density ρ (kg/m^3)	7850
Sound Speed c (m/s)	4620
Surface Tension γ (N/m)	1.5
Yield Strength Y_0 (GPa)	2.0
Fracture Toughness K_{c0} (MPa m$^{1/2}$)	40
Melt Temperature T_m (K)	1800
n	1
m	0.1
n'	-1

allows each point in the strain rate - temperature plane to be mapped into a fragment size for a given material.

The fragmentation theories described above are derived assuming spall induced by uniform volumetric dilatation, so they are most applicable to the prompt fragmentation of the steel sphere induced by the impact. The fracture process is complete within a few microseconds following impact. The strain rate and temperature files generated by each of the calculations that were produced immediately after this time were used for the fragment size predictions.

To obtain the fragment size distribution from the analysis, files are generated by the wavecode calculations that contain the strain rate and temperature at the time of fracture for each cell containing fractured material. There is thus a mass associated with each strain rate - temperature pair, which is just the total mass, m, of the material in the cell. The simplest assumption to make when determining fragment size distributions is that all of the mass in the cell produces equal particles of size S, given by the appropriate one of Equation 18 to Equation 20. Thus, letting i be the cell index, where $i = 1, \ldots N$ and N is the total number of cells containing fractured material, the cell data consist of N pairs m_i, S_i where m_i is the mass of material in cell i and S_i is the size of all the particles in the cell. If the data are arranged in order of increasing fragment size, so that $S_i \leq S_{i+1}$, then the cumulative mass of fragments less than or equal to size S_i is

$$M(S_i) = \sum_{j=1}^{i} m_j \tag{24}$$

However, as previously described (Grady and Kipp, 1985), statistical considerations indicate that a distribution of fragment sizes should be determined about the mean fragment size calculated for each cell, S_i. The form of the distribution is obtained by assuming that fragments in the mass m_i are Poisson-distributed. This leads to a probability distribution of finding a fragment of mass μ in the cell within a tolerance $d\mu$ given by

$$dP(\mu) = \frac{1}{\mu_a} e^{-\mu/\mu_a} d\mu, \tag{25}$$

where μ_a is the average, or mean, value of the fragment mass in the cell. Integrating from 0 to μ and multiplying by the total mass m_i of the cell gives the cumulative mass of fragments of mass less than or equal to μ in the cell

$$M(\mu) = m_i\left[1 - e^{-\mu/\mu_a}\right]. \tag{26}$$

Now, assuming that the mass of the fragment is related to the cube of the fragment size (such as for cubic or spherical particles) and noting that the average mass μ_a corresponds to a fragment having the average size S_i,

$$\frac{\mu}{\mu_a} = \left(\frac{S}{S_i}\right)^3. \tag{27}$$

Therefore, the cumulative mass of fragments in cell i having a size less than or equal to S is

$$M(S) = m_i\left[1 - e^{-(S/S_i)^3}\right]. \tag{28}$$

Finally, the total cumulative mass of all fragments in all cells having a size less than or equal to S is

$$M_T(S) = \sum_{i=1}^{N} m_i\left[1 - e^{-(S/S_i)^3}\right]. \tag{29}$$

It was found that if the original distribution (Equation 24) is sharply peaked, a large spread is generated by the statistical relations. However, if the original distribution already contains a large range of fragment sizes, the additional statistical spread is minimal. The statistical distributions do show the addition of a tail at small, possibly aerosol-sized, fragments, but the total additional mass in the aerosol source term so generated is negligible. In application, the cell data is grouped into "bins" of a chosen fragment size increment.

The spectral distribution in size, corresponding to Equation 25, is

$$dP(S) = 3\frac{S^2}{S_i^3}e^{-(S/S_i)^3}dS. \tag{30}$$

The original distribution of average sizes can be depicted as in Figure 15a, where each bin contains

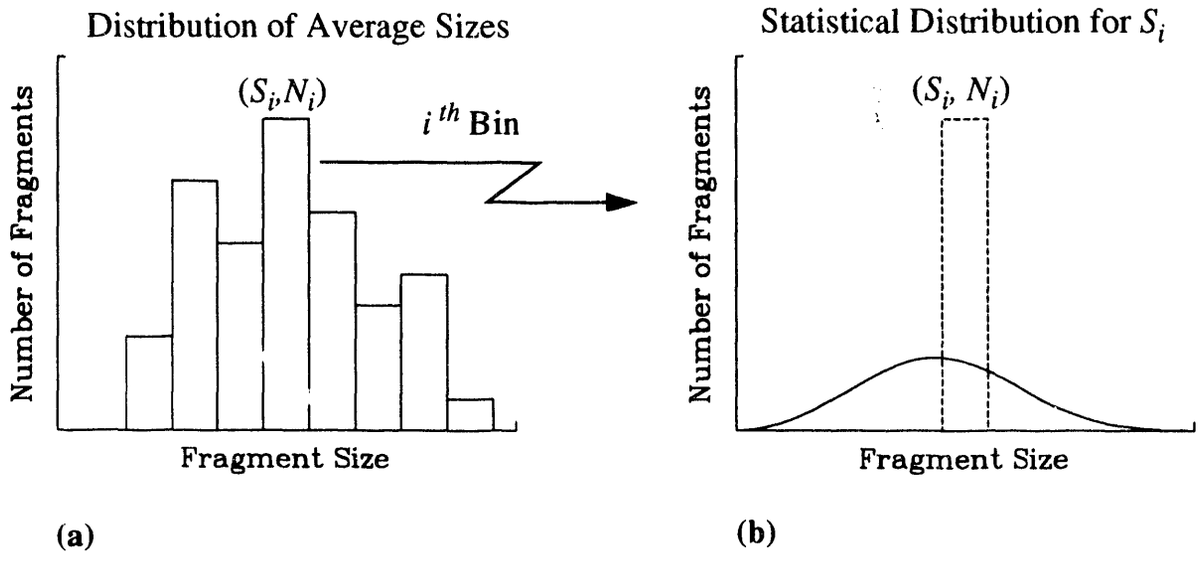

Figure 15. Process of transforming the original fragment size distribution to a statistical fragment size distribution.

the number of fragments, N_i, of an average fragment size, S_i. These parameters are used in Equation 30 to define the associated statistical distribution for that particular bin, as represented in

Figure 15b. All of these statistical distributions are summed to obtain the final statistical distribution of fragment sizes for the event. Note that although the distribution is exponential in mass, it is exponential in the cube of the size, and the resulting coefficient in Equation 30 contains the square of the size, leading to the character of the statistical distribution in Figure 15b.

F. Numerical Simulations of Steel Sphere Impact on PMMA Targets

Impact simulations of a steel sphere onto a PMMA target plate were made with a physical space that was partitioned into uniform square cells, with a resolution of 0.05 mm (about 60 cells in the radius of the sphere). The two-dimensional, axisymmetric geometry encompassed a 20 mm radius and a 20 mm axial length, requiring 160,000 computational cells. This radius is sufficiently large that edge effects of the target do not influence the fragmentation behavior of the steel sphere. The steel and PMMA were both represented as low temperature Mie-Gruneisen solids, in which the Hugoniot was described with a linear shock velocity - particle velocity relationship. The properties used in the calculations are listed in Table 5. The fragmentation parameters for the steel

Table 5: Material Parameters Used For Calculations

	PMMA	Hard Steel
Density (kg/m^3)	1186	7850
Bulk sound speed (m/s)	2598	4570
Linear shock velocity - particle velocity slope	1.516	1.49
Gruneisen coefficient	0.97	2.17
Yield strength (GPa)	0.2	2.0
Poisson ratio	0.32	0.29
Fracture stress (GPa)	0.15	4.0

are listed in Table 4. The mass of the sphere used in the calculations was 1.052 gm, slightly larger than the experimental mass of 1.027 gm.

As an example, consider the case of Test 5, in which a steel sphere impacts a 3.38 mm PMMA target plate at a velocity of 4570 m/s (*cf* Table 1). The computed sequence of penetration that occurs is plotted in Figure 16. Note that the sphere is deformed as it progresses through the plate, with the leading surface undergoing significant flattening. The impact pressure is about 30 GPa, well above the 2 GPa yield strength of the steel. Just after 1 μs, void is beginning to be inserted into the sphere by the code as spall fracture commences. It is apparent from these plots that the PMMA material in front of the sphere has been accelerated to a higher velocity than the exit velocity of the sphere, as is easily confirmed from a one-dimensional pressure - particle velocity diagram of the impact. Flash laser photographs of similar events also clearly show the dispersed PMMA debris leading the clustered steel debris (Ang, 1992). We note in passing that the appearance of the calculated PMMA target plate residual hole is that of a rather ductile material; the experiments

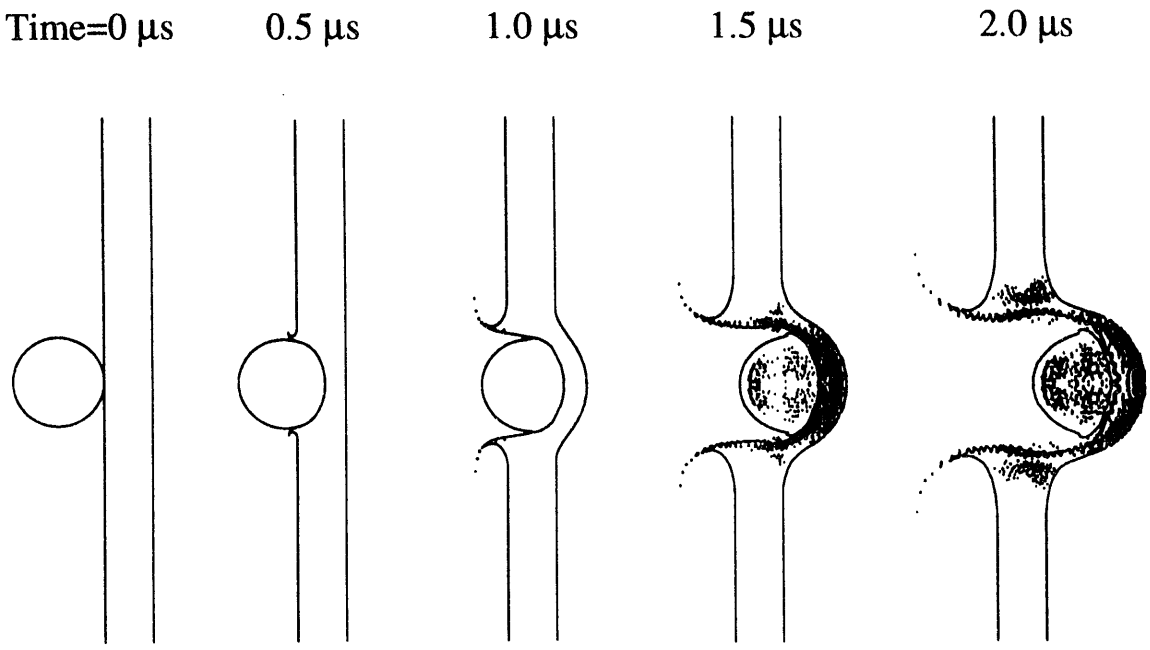

Figure 16. Calculated sequence of a 6.35 mm steel sphere, with normal incidence velocity of 4570 m/s, perforating a 3.38 mm PMMA target plate (Test 5).

indicate a far more distinctive residual hole surrounded by large fractured rings that have been removed, suggesting that there are equation of state and plastic fracture issues to be pursued.

Tracer particles, embedded in the sphere to provide point histories of computed variables, indicate that fracture is completed between 1.5 and 2 μs. After this time, the PMMA imparts very little impulse to the steel sphere. This response is illustrated in Figure 17, where the minimum principal stresses through the axial diameter of the sphere are plotted. (The first pulse is recorded at the impact surface, and the final pulse at the trailing surface.) The tensile stress is observed to reach a limit of about 4 GPa, then unload as void is added to the local cells to relieve the state of tension. The strain rates going into tension along the axis of the sphere are about 2×10^5 per second. This strain rate occurs in the regions that are driven into tension by release wave interactions. Divergent strain rates near the periphery of the sphere tend to drop below 1×10^5 per second. As the shock pulse transits the axis of the sphere, the amplitude decays from an initial peak of about 30 GPa to less than 10 GPa. The immediate consequence of this decay in impulse is a larger decrease in particle velocity at the leading edge of the sphere than at the trailing edge, so that the trailing material in the sphere has a relative velocity towards the leading edge of the sphere. This relative velocity of the leading and trailing surfaces of the sphere explains the tendency of the particles to stay clustered in a thin disk, as seen in the radiographs (*cf* Figure 2 and Figure 7). As a consequence of the impulse delivery being completed by about 2 μs, the formation of fragments has also been completed by then, and the fragmentation post-analysis calculations can be made.

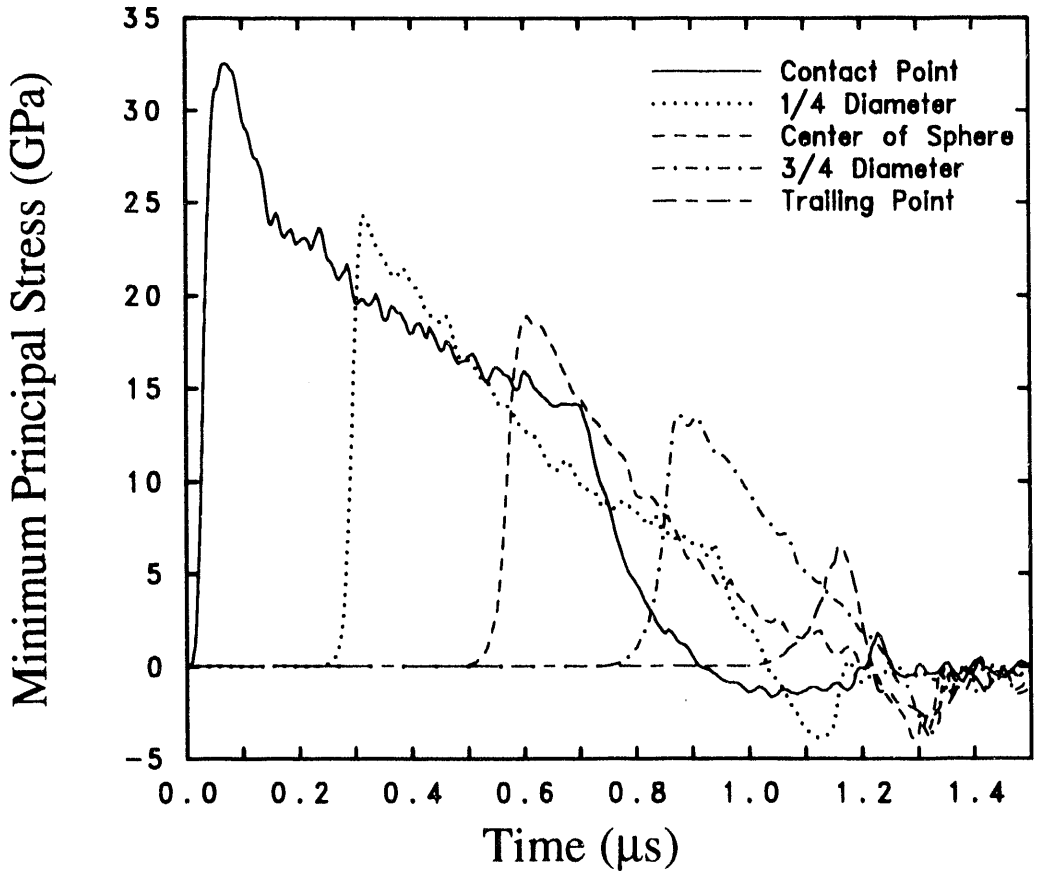

Figure 17. Histories of minimum principle stress at points along the axis of the steel sphere.

The debris is basically in free flight by this time, expanding as seen in the radiographs (in Figure 2) at much later times (*e.g.*, 30 and 60 μs).

When the steel fragmentation characteristics were computed for this example, it was found that less than 25% of the mass of the steel sphere had fragmented. That is, the fracture stress of 4.0 GPa was exceeded in only a quarter of the volume of the sphere. Examination of the tensile strain rates that occur throughout the sphere indicate a range from about 6×10^4 per second to over 1×10^6 per second. Under these conditions, the expected spall stress would range from 2.2 GPa to 5.6 GPa, based on derived expressions by Grady (1988) for brittle fracture. Recalculating this example with a fracture stress of 2.0 GPa results in about 80% of the sphere fracturing; with a fracture stress of 1.0 GPa, 100% of the sphere fractures. It is clear that fracture based on a constant tensile stress limit does not accurately represent the behavior of this steel, nor of other materials with similar strain-rate dependence.

To further elucidate this issue, it is of interest to evaluate the shock energy coupled into the sphere considered earlier by analytic methods, as defined by Equation 13. In the current example of a 3.38 mm PMMA target plate perforated by a 6.35 mm steel sphere, that analysis indicates the

steel sphere acquires approximately 110 J of energy over the duration of the impact process. This calculation is based on an initial impact pressure of about 36 GPa, with a corresponding shock velocity of 5780 m/s and particle velocity of 787 m/s. (In this analysis, t_1 is 0.15 μs, t_2 is 0.34 μs, a_c is 2 mm, and b_c is 1.4 mm.) This energy increase represents the combined kinetic and internal shock heating, and assumes a reverse ballistic impact (*i.e.* the sphere is initially at rest). One-half of this energy is internal energy, or about 55 J. From the numerical analysis, the individual energy components associated with the steel sphere can be determined. The increases of the kinetic and internal energies as a function of time for the steel sphere are plotted in Figure 18. The reference

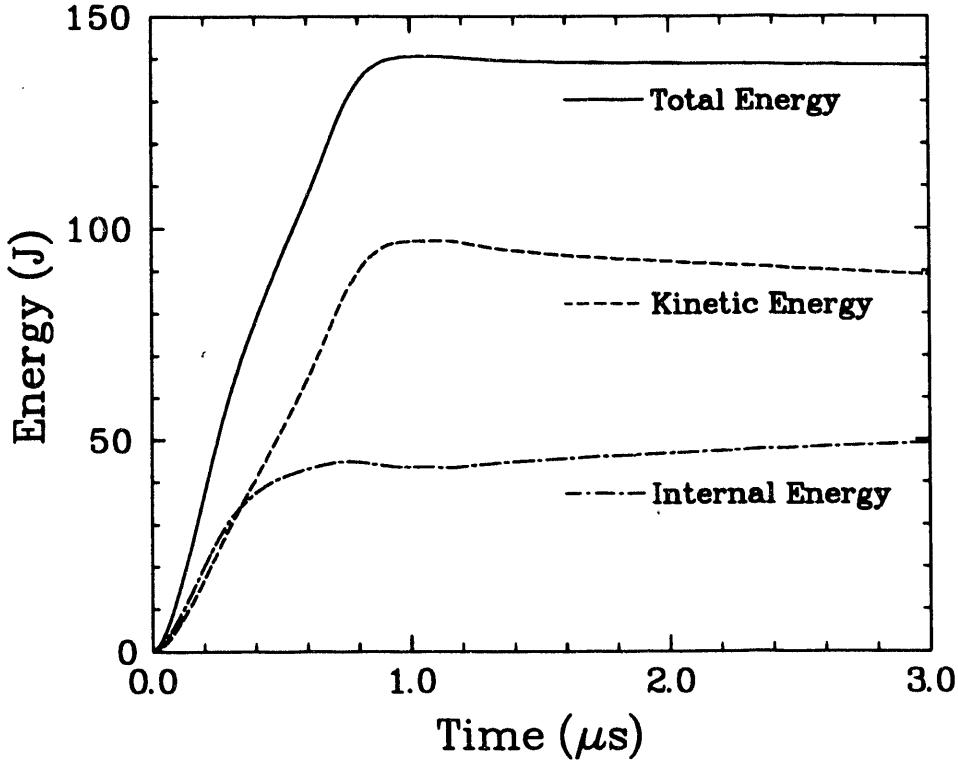

Figure 18. Internal, kinetic, and total energy for the steel sphere from the numerical analysis of Test 5.

internal energy assigned by the shock wave code to the steel (141 J) has been subtracted from the internal energy so that only changes in the internal energy acquired during the impact are plotted. The total change in energy of the steel sphere during the impact process is about 140 J. The change in internal energy is about 50 J, which corresponds well with the calculated analytic value; the kinetic energy tracks the internal energy until about one-half microsecond, and then the kinetic energy continues to increase to about 90 J. The impact process is dominated by changes in kinetic energy of the sphere, and the majority of this change has occurred in the first microsecond. The internal energy of the sphere is acquired during the first one-half microsecond, and changes little after that. The sum of t_1 and t_2 is about 0.5 μs, supporting the numerical results. This indicates that the primary shock contribution to the internal energy of the sphere has occurred well before the shock has even completed a single transit of the axis of the sphere, which takes over one

microsecond (*cf* Figure 17). The energy does not distinguish between shock heating and plastic deformation heating. The sphere is still decelerating for another one-half microsecond, as steady hydrodynamic forces act on it.

Fragmentation Calculations

As a working basis for this example, the fragmentation process was permitted to proceed using the 1.0 GPa fracture stress limit. The resulting computed steel fragment size distribution is shown in Figure 19, labelled "w/o statistics". This distribution sums the masses of fragments in each material cell, where the average fragment size is calculated from the local strain rate, as defined in Equation 18 to Equation 23. The figure plots the total steel fragment mass determined for each fragment size "bin", summed throughout the sphere. Each bin includes a fragment size increment of 0.02 mm. The largest mass of fragments have an average fragment size of about 0.6 mm. The temperature in the steel has increased only about 100 K, so that the majority of the material falls in the brittle, or fracture toughness dominated, region of fragmentation.

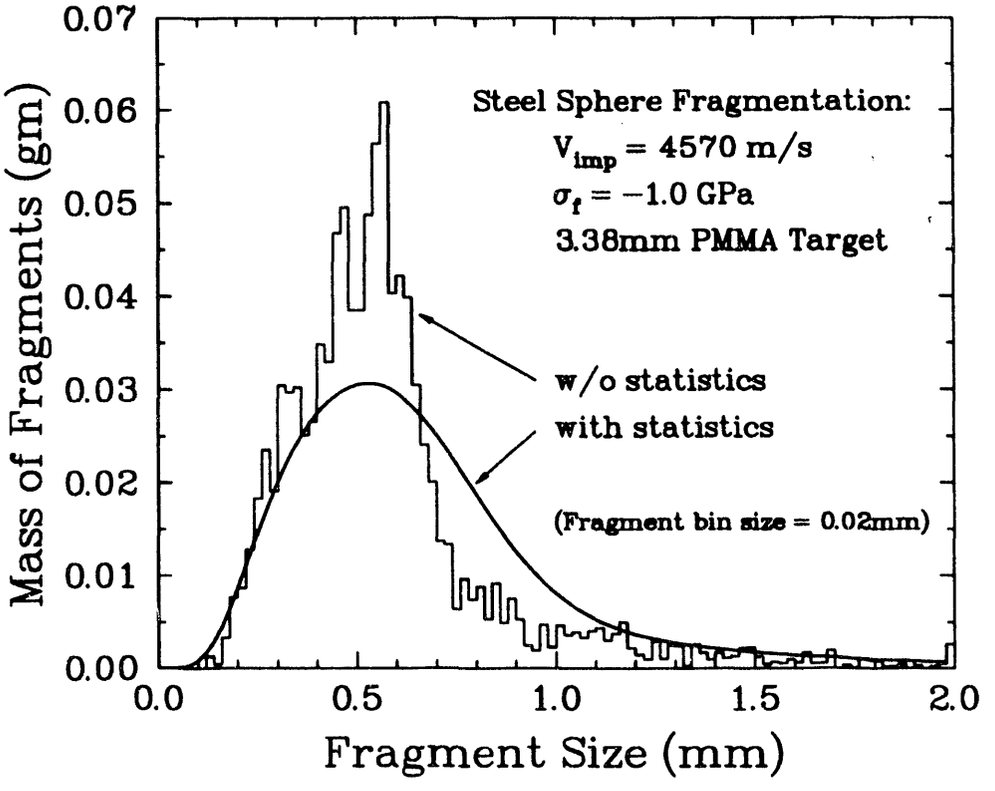

Figure 19. Mass distribution of steel fragments *vs.* fragment size resulting from the impact of a 6.35 mm steel sphere with a 3.38 mm PMMA target plate (Test 5). This distribution represents the sum of the average local fragment size for each steel cell. Both original and Poisson statistics distributions are plotted

As discussed in the previous section, the fragment size calculated for a given strain rate represents the average fragment in an exponential (Poisson) distribution of sizes. The masses associated with each of the fragment sizes shown in Figure 19 (curve labelled "w/o statistics") can be modified to account for this statistical spread by employing the concepts expressed in Equation 24 to Equation 29. When these equations are applied to the current example, the mass associated with each particle size results in the distribution labelled "with statistics" in Figure 19. The Poisson statistics (in which the same size "bins" were used) tend to broaden the distribution up to about 1.1 mm fragment sizes, and do not significantly affect the upper and lower extremes of sizes. The integral of the mass with size, as described by Equation 29, results in the cumulative mass as a function of fragment size. Figure 20 contains both the original calculated cumulative mass distribution and the associated statistical cumulative mass distribution as a function of fragment size. The total mass of steel accounted for up through particle sizes of 2 mm is 1.01 gm, or about 96% of the 1.05 gm mass of the sphere used in the calculations.

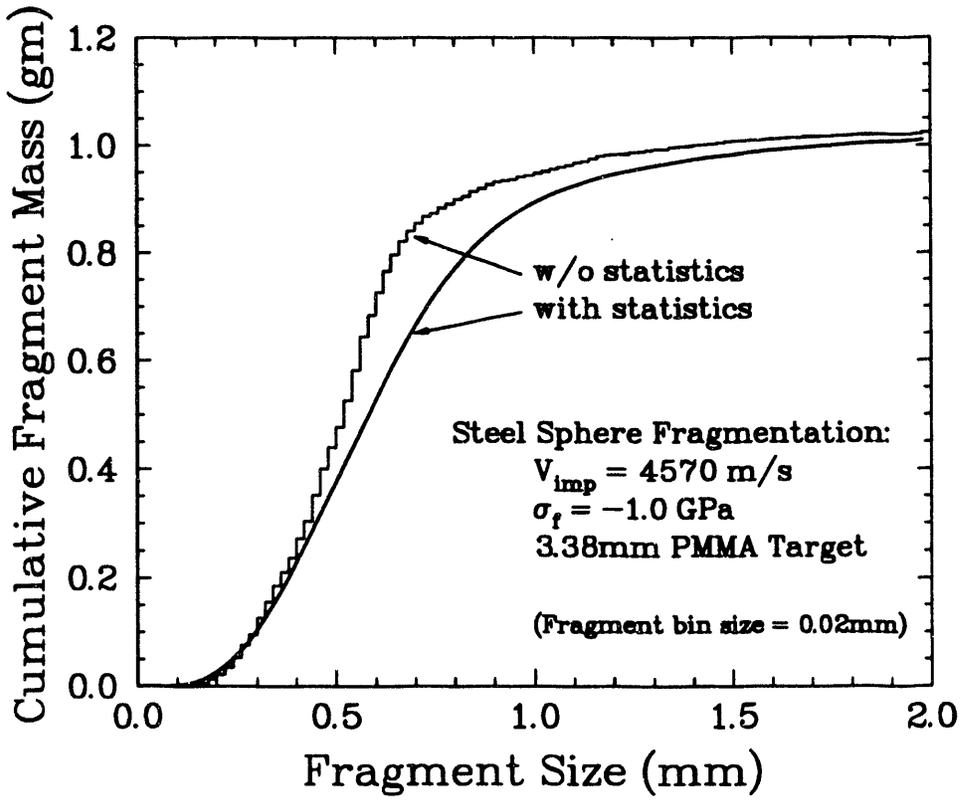

Figure 20. Cumulative mass distribution of steel fragments *vs.* fragment size resulting from the impact of a 6.35 mm steel sphere with a 3.38 mm PMMA target plate (Test 5). This distribution represents the accumulated mass sums of the average local fragment size. Both original and Poisson statistics distributions are plotted.

The corresponding distributions that show the number of fragments at each fragment size are plotted in Figure 21. Now the broadening effect of the Poisson statistics is apparent for the small size particles. The largest number of particles are of size 0.2 mm; the largest mass of particles are

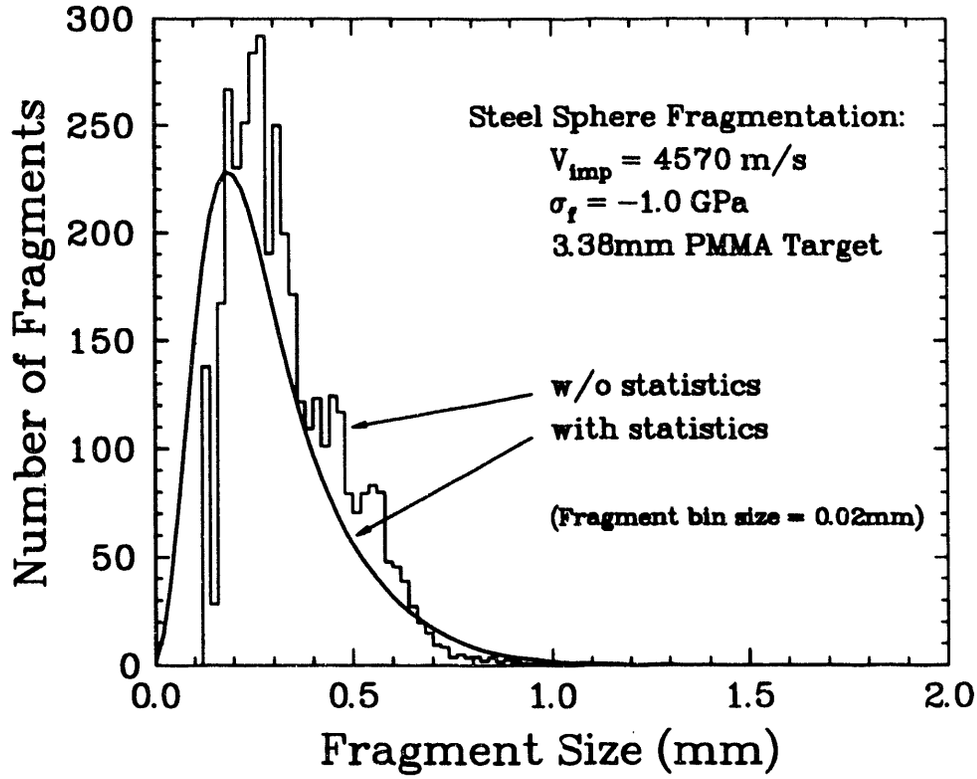

Figure 21. Final number distribution of steel fragments *vs.* fragment size resulting from the impact of a 6.35 mm steel sphere with a 3.38 mm PMMA target plate (Test 5). Both original and Poisson statistics distributions are plotted.

of size 0.6 mm. This prediction compares well with the experimentally observed fragment size of about 0.7 - 1.1 mm (Figure 3) at this impact energy. The cumulative number of particles calculated here is nearly 3800, the majority of which are less than 0.5 mm in size. The average fragment size, based on this number of fragments, is about 0.4 mm (spherical diameter). The average particle size determined from the radiographs for this example (Test 5) was about 0.7 mm, for about 400 particles (Table 3). Hence this computed number of fragments is nearly an order of magnitude too large, suggesting that the estimate of strain rate at the time of failure is too large by about a factor of 2 (*cf.* Equation 18). Some effort is required to evaluate the fracture model being used to ensure that fracture occurs at the proper time, since the governing strain rate is directly tied to this aspect of the model. It has also been observed that the strain rates, and consequently the average calculated fragment sizes, depend on the equation of state being used for the materials. Issues relating to the joining of the energy-based and statistical fragmentation theories may also contribute to uncertainty in the fragment number prediction.

Target Thickness Variations

To examine trends of the behavior resulting from target thickness variations, a suite of eight impact calculations was made in which the impact velocity was fixed at 4500 m/s. Variations in PMMA target thickness from 0.76 mm (1/32 inch) to 6.35 mm (1/4 inch) covered most of the range of the experiments, providing a large spread in the amplitude of the impulse imparted to the steel sphere. From these calculations, comparisons can be made with experimental data for the loss in axial momentum, and the expansion velocity of the particles debris cloud.

The loss in axial velocity as a function of target plate thickness is plotted in Figure 22, and the numerical data clearly compares well with the experimental data. This figure can be compared with Figure 5, noting that the numerical simulations are representing the experimental data in much the same way as the analytic expression. The calculated curve in Figure 22 is not quite linear, and tends to have an upward curvature as the PMMA target thickness increases beyond 3 mm.

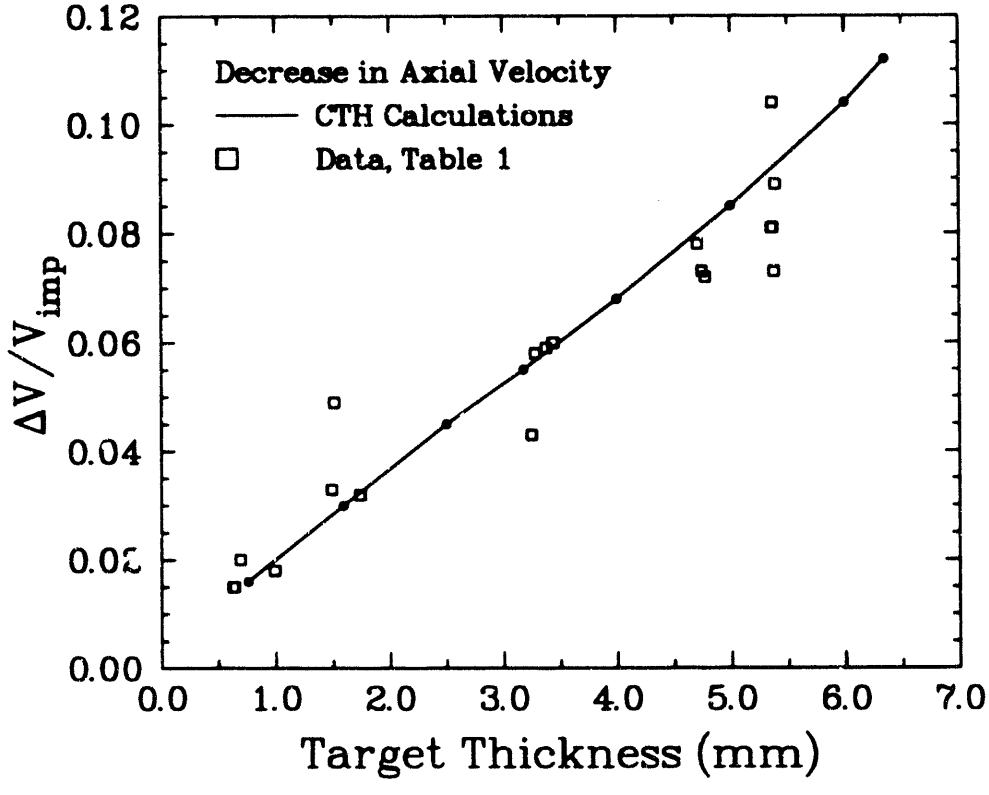

Figure 22. Decrease in axial velocity of the steel sphere as a function of PMMA target plate thickness. Data is from Table 1.

The expansion velocity of the outer debris edge is plotted in Figure 23 as a function of PMMA target plate thickness. The computed points were determined by evaluating the maximum radial momentum acquired by the steel during penetration. The computed values generally fall within the range of the experimental data. This figure can be compared to Figure 9, in which three curves of constant impact velocity are included. In the present figure, only an impact velocity of 4500 m/s

has been tabulated. In principle, the source of the particles in the debris cloud can be determined from velocity histories at points distributed throughout the sphere. Along the initial surface of the sphere, the amplitude of the maximum lateral velocity varies from zero at the leading impact point to a maximum near the equator, returning to zero at the trailing point on the axis. Analysis of the velocity histories on a cross-section at the equator of the sphere indicates a linear increase in velocity from zero on the axis to maximum on the surface, resulting in the distribution of fragments throughout the disk seen in the radiographs. This continuous spatial distribution of particles is in contrast to the commonly observed hollow debris cloud that forms when a target imparts a larger energy to the projectile (*e.g.* Grady and Passman, 1990; Piekutowski, 1992). We note that as the thickness increases, the calculated expansion velocity begins to increase again. This calculational result may relate to the experimentally observed transition to Region III diffuse fragmentation (Figure 6, Table 2) in which anomalously large expansion velocities were observed.

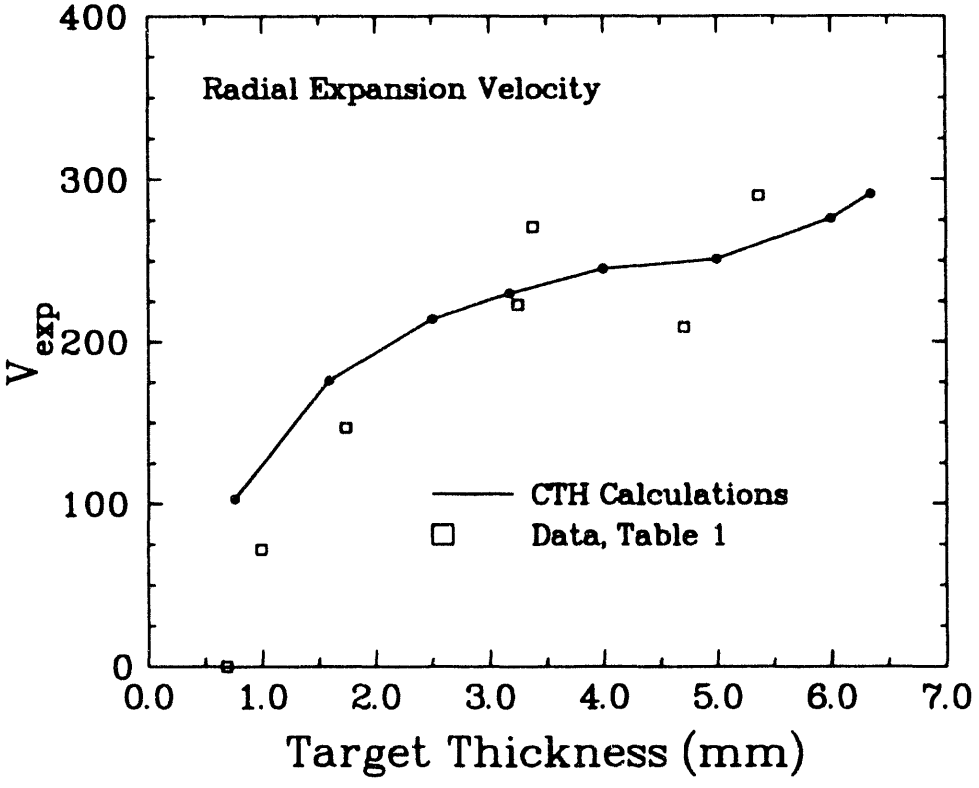

Figure 23. Variation of maximum steel particle debris cloud expansion velocity with PMMA target plate thickness. Data is from Table 1.

An initial attempt was made to quantify the influence of target thickness, or imparted impulse, on the fragmentation characteristics of the steel sphere. For the present calculations with an impact velocity of 4500 m/s, the fragment size distributions for several thicknesses of PMMA targets are compared. The comparison is made on the basis of the statistical fragment size distributions, as illustrated in Figure 19. A statistical distribution was determined for each impact case. The results are plotted in Figure 24. The least impulse imparted to the sphere is for a PMMA thickness of 0.76

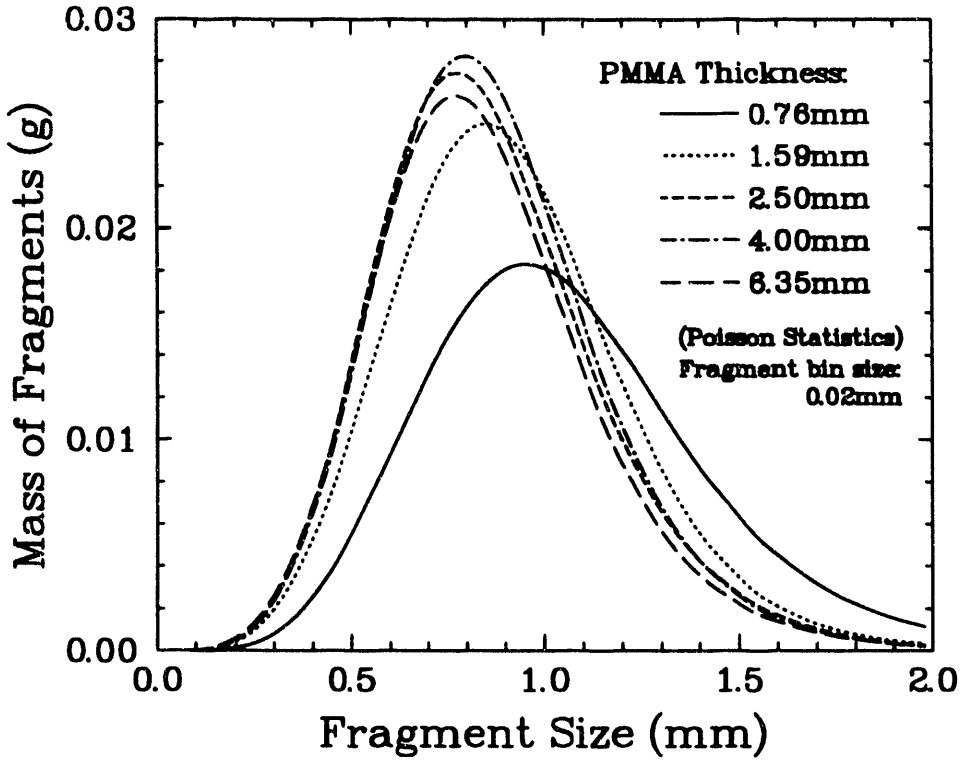

Figure 24. Comparison of statistical fragment size distributions for several thicknesses of PMMA targets, and an impact velocity of 4500 m/s.

mm, and the fragment size distribution has the largest average fragment size (about 1 mm) of all the distributions, as should be. However, the remaining distributions are observed to be nearly indistinguishable from one another, suggesting that the sphere is fragmented in the same way, on average, for PMMA target thicknesses from 1.6 mm to 6.35 mm. However, from radiographs of the debris clouds, the qualitative data indicate a trend of continually smaller fragments as the target thickness increases. The implication is that fracture of the steel sphere is not being correctly represented. As a counter, however, the image-processed fragment size data (Figure 24) indicates a degree of insensitivity to impact conditions above an expansion velocity of about 100 m/s. Indications of this error were mentioned in previous paragraphs regarding the threshold fracture stress required to obtain complete fracture of the steel sphere. Further work will be necessary to sort out the exact source of the error, and correct it in a satisfactory manner. The comparisons made in Figure 24, however, are of the kind desirable for evaluating effectiveness of armor or warheads.

Target Profile Comparison

In some cases, the PMMA targets were recovered intact following an impact experiment. This provided an opportunity to compare the calculated crater and residual hole profiles with that of the recovered target. For example, the cross-section of the PMMA target for Test 19 is sketched in Figure 25a (also see Figure 13). The original steel sphere has been included for reference of scale. This target profile is representative of the recovered targets. The residual hole in the PMMA is only slightly larger than the original diameter of the steel sphere. Both the front and rear faces of the

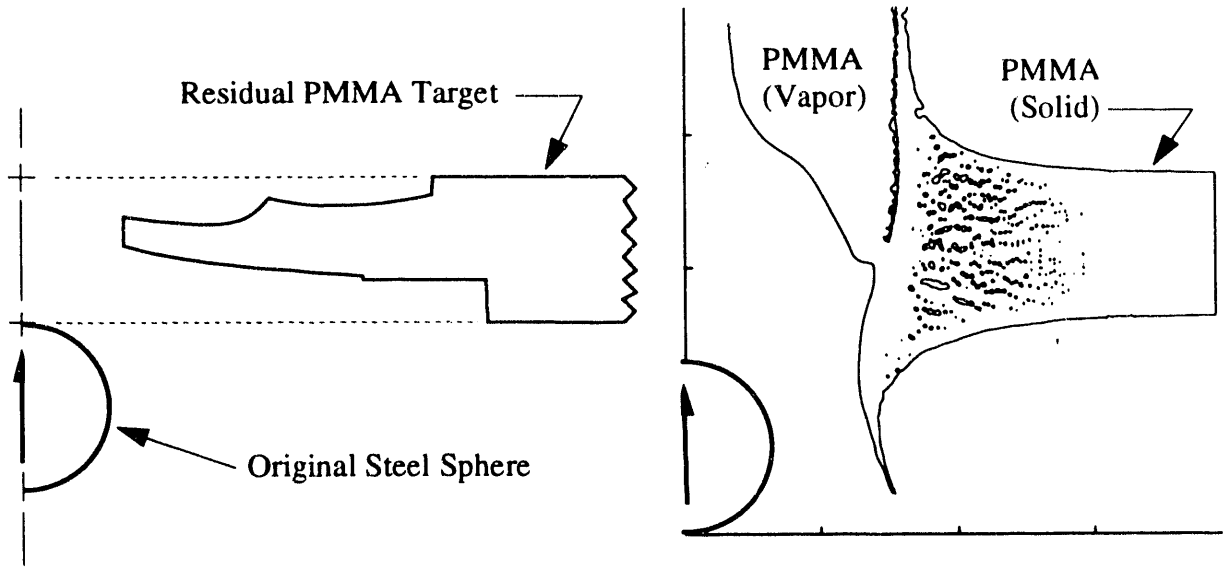

(a) Experimental Profile **(b)** Calculation

Figure 25. Cross-section recovered (a) and calculated (b) comparisons of PMMA target for Test 19 (4610 m/s impact onto 5.385 mm PMMA).

target have been excavated to a radius of nearly five times that of the sphere radius, so that the remaining central section has the appearance of a washer retained in the target. In contrast, the calculated target profile is shown in Figure 25b. The strength material model for the PMMA was elastic-perfectly plastic. Although there is a large fractured region in the target, extending to about four and one-half sphere radii, there is no evidence of preferential front or back face surface excavation. The residual target hole radius is over twice the original projectile sphere radius. The front and rear crater lips are characteristic of this material treatment. At this time, the significant differences between the calculated and experimental target profiles have not been explained. Attempts to modify fracture strengths, yield strengths, or equations of state (with and without vaporization) for the PMMA have had only negligible influence on the profile calculated in Figure 25b. It has already been noted that the impulse imparted to the sphere is correct, because the decrease in axial velocity is corroborated with the experiments (*cf* Figure 22). PMMA is a visco-plastic material, and shock wave propagation and release wave structure are affected by this property, particularly below 6 GPa (Schuler and Nunziato, 1974). This major modification to the equation of state would be a profitable area to explore. In addition, there is also the distinct possibility that PMMA fractures in a much more complex manner than currently modeled.

G. Secondary Target Damage

As indicated in the experimental configuration shown in Figure 1, a secondary target (witness) plate was placed in the line of flow, down stream from the primary impact point, and intercepted the projectile and PMMA target debris. These secondary target plates were prepared from 6061-T6 aluminum plate stock into square plates 15 cm on a side and with several

thicknesses (see Table 1). Depending on specific experiment parameters (impact velocity, PMMA plate thickness, range to secondary plate), the secondary target plates suffered various degrees of impact damage.

The damage experienced by secondary objects exposed to the high-velocity fragment debris of a primary fragment event represents an effect for which computational and analytical solution methods are in an early stage of development. Consequently, the supplemental data from the present series of experiments are useful for guiding theoretical model development focused on secondary-damage high-velocity impact events.

Experimental Results

The thickness d_s of the aluminum target plates was either 6.35 mm (1/4 in) or 12.7 mm (1/2 in), although one 9.53 mm (3/8 in) plate was used. Secondary plates were positioned behind the primary PMMA plates by a distance x_{ps} which ranged between about 40 and 65 cm (a somewhat shorter distance was used in one early test). This dimensional data is provided in Table 1.

Several features of the secondary plate damage are provided in Table 6. First the loss of plate mass caused by the impact and determined by measuring the weight of the plate before and after the test was included. Because of uncertainties in the final disposition of the steel projectiles, and in the difference measurement, an uncertainty of about ± 1.0 g was assigned to this data. Second, in almost all of the tests, whether or not target penetration occurred, the impact debris footprint encompassed a well-defined area on the secondary plate. (Tests 19, 23, and 24 were the exceptions to this observation.) This footprint area was also included in Table 6. In those experiments in which the primary fragment debris penetrated the secondary target, removing a substantial mass of aluminum, the projected area of the hole was also measured and recorded in Table 6. Typically this area was 60 to 80% of the footprint area for that test.

Secondary target plate damage in the present series of experiments could be generally grouped into three classes. These classes were identified in order of severity as splash, perforation, and plugging.

In the plate damage identified as splash the target plate was not penetrated by the steel projectile debris. There is usually a degree of bulging of the back side of the plate over the area behind the region of impact. Damage to the front of the target plate was perceived as a crater extending over an area comparable to the spread of the fragment debris observed in the radiographic record extrapolated to the point of impact. This crater area (footprint) is reported in Table 6. The crater cavity appeared to be accommodated as much by the back-surface bulging as by the splash of target aluminum during impact. Only a few grams of target material are removed by the splash process (see Table 6). The crater floor appeared chaotic with evidence of many subcraters and deeper channels of varying depths associated with the impact of individual fragments.

The character of plate damage called perforation was similar in appearance to that of splash. The only difference is that impact intensity was sufficient to cause full penetration of one or more individual projectile fragments. These penetrations were typically channels through the target

Table 6: Experimental Properties of Secondary Impact Damage

Test #	footprint area[b] cm^2	mass[c] g	damage mode[d]	Test #	footprint area cm^2	mass[c] g	damage mode[d]
1[a]	—	—	—	13	27.2	2.6	spl[e]
2[a]	—	—	—	14	15.9	1.1	prf
3	9.2 (6.7)	15.6	plg	15	8.1 (0.9)	0.5	plg
4	15.6 (13.6)	30.4	plg	16	16.0	4.4	spl
5	33.2	3.1	spl	17	32.3	4.4	prf
6	8.4	7.6	prf	18	30.8	0.1	spl
7	22.8	2.8	prf	19	84.2	2.4	prf[ef]
8	9.4 (7.4)	14.1	plg	20	18.5	5.1	prf[e]
9	5.6 (4.1)	8.6	plg	21	12.1	6.9	prf
10	3.7 (2.0)	8.6	plg	22	10.7 (8.0)	22.7	plg
11	5.7 (2.5)	8.6	plg	23	full plate	1.1	spl[f]
12	7.8 (3.6)	13.6	plg	24	177.0	2.0	spl[f]

[a] Plate was not recovered.
[b] Number in parentheses are hole area where plugging occurred.
[c] Accuracy of 1 gm estimated.
[d] plg - plugging, prf - perforation, spl - splash.
[e] Back surface spall.
f Diffused footprint (see text).

thickness with openings ranging from about one to several millimeters. The minimum mass of steel fragment required to perforate the aluminum witness plate has not been determined empirically, although there have been numerous studies made for other projectile / target material combinations to ascertain the ballistic limit velocity (*e.g.* Backman and Finnegan, 1984; Cour-Palais, 1987; Herrmann and Wilbeck, 1987; Hohler and Stilp, 1987). A brief numerical study indicates that perforation of a 12.7 mm aluminum target will occur with a single steel particle of 2.5 - 3 mm diameter, at an impact velocity of 4300 m/s. However, allowing for a second particle impact in a previous crater, two 1.7 mm particles spaced 10 mm apart (about the cloud thickness at impact), will perforate the aluminum target, with about one half the kinetic energy required by a single particle. The average size particles for this experiment was about 0.7 mm (Table 3), so there would not be much expectation of two particles of 1.7 mm in the same trajectory, and perforation of the witness plate is unlikely (see Table 6).

For plate damage classified as plugging the collective impulse of the fragment debris was sufficient to remove (plug) a region of the plate leaving a hole comparable to the projected area of the debris cloud. For the tests in which the primary PMMA plate was insufficient to fragment the steel sphere, typical single-particle plugging phenomena was observed. The plug hole diameter was somewhat larger than the projectile diameter and increased with increasing impact velocity (see Table 6). When primary projectile fragmentation and debris spread occurred before secondary impact the size of the plug region was significantly larger.

Three impact experiments (Tests 19, 23, and 24) did not readily fall into any of the three classes of secondary plate damage just described. These three tests have already been discussed in terms of the substantially broader dispersion of fragment debris observed on the respective radiographic records. Impact damage on the secondary target also reflected this broad dispersion of debris. Although areas for the impact footprint are reported for Tests 19 and 24 in Table 6, the radius of these two footprints were not distinct, consisting of numerous independent fragment craters which decreased gradually in impact density with increasing radius. The footprint of Test 23 encompassed the full area of the 15 by 15 cm plate. In each of these three tests a major central crater (~15 mm in diameter) caused by a large fragment or cluster of fragments was observed. This crater was virtually identical in Tests 23 and 24, causing significant back surface bulging and incipient spall cracking. In Test 19 a central hole approximately 8 mm in diameter was punched through. There is some evidence for the responsible central fragment or fragment cluster in the radiographs for these three tests.

Photographs of four of the secondary target plates are shown in Figure 26 and Figure 27 to illustrate the various damage modes observed in the present test series. The secondary plates shown were all 12.7 mm in thickness and placed approximately 64 cm behind the PMMA impact plate (see Table 1). Velocities for the tests shown ranged from about 4.0 to 4.7 km/s and various thickness PMMA plates were used. The plate for Test 18 in Figure 26a illustrates the localized splash mode of secondary target damage observed in many of the tests. The plate was not perforated and all fragment impacts are confined (clustered) within a relatively narrow solid angle subtended from the point of impact. In Test 20 slightly different impact conditions led to a smaller area of impact and perforation of several fragments through the plate thickness. Conditions for Test 22, shown in Figure 27a, led to a tight group of the fragment debris and complete plugging damage to a section of the secondary target. The secondary target plate in Figure 27b for Test 24 illustrates the transition to enhanced debris expansion and the more diffused damage footprint observed in several tests at high velocities and/or with thick target plates.

Discussion of Secondary Target Damage

In the remainder of this section the discussion will focus on the critical issues of the predictive analysis of secondary target damage. Computational or analytic methods for addressing secondary damage are not yet mature. The description and treatment of the discrete and statistical character of the primary fragment debris which are sufficient to provide adequate initial conditions for interactions with subsequent barriers represents a challenge which is only beginning to be met.

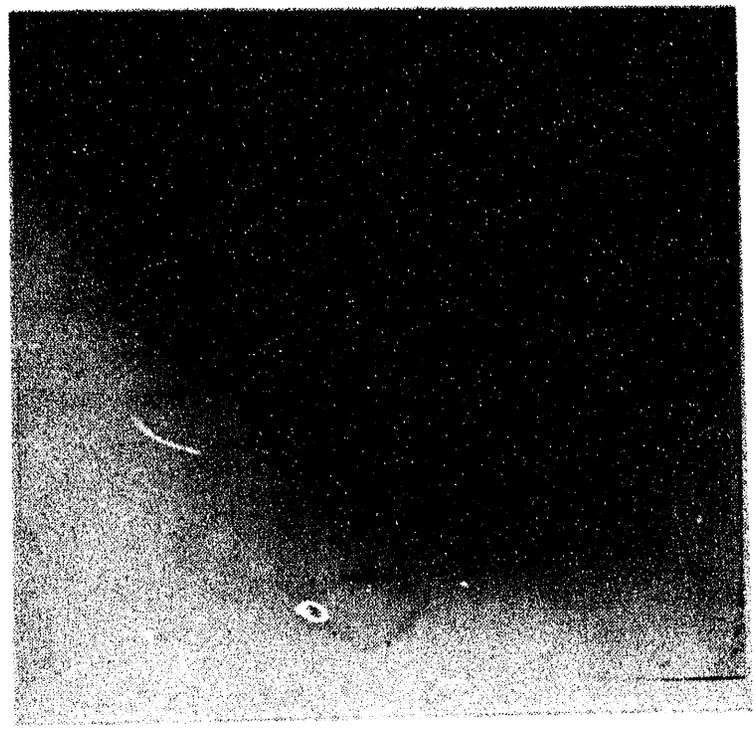

a. Test 18 - Impact velocity = 4.43 km/s - PMMA plate thickness = 4.71 mm. Splash damage.

b. Test 20 - Impact velocity = 4.04 km/s - PMMA plate thickness = 4.75 mm. Perforation damage.

Figure 26. Secondary target damage modes.

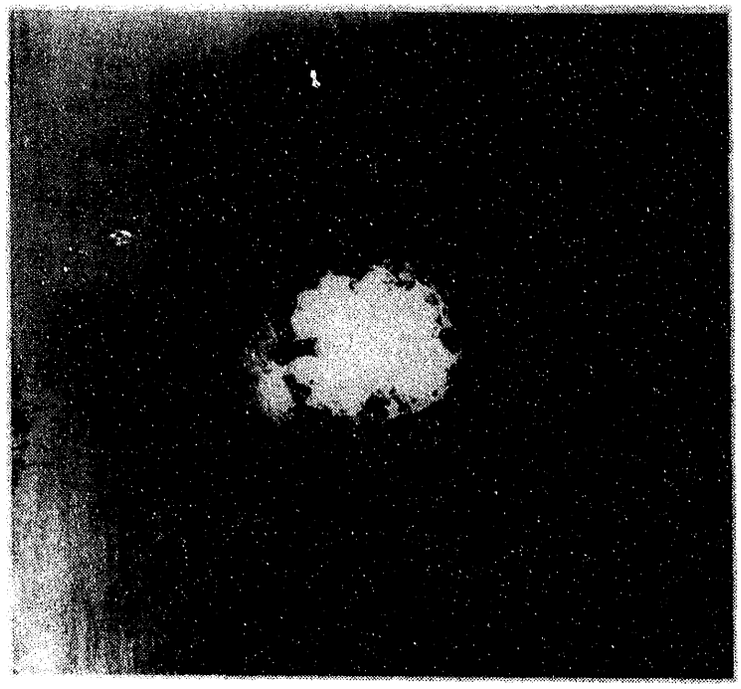

a. Test 22 - Impact velocity = 4.70 km/s - PMMA plate thickness = 0.99 mm. Plugging damage.

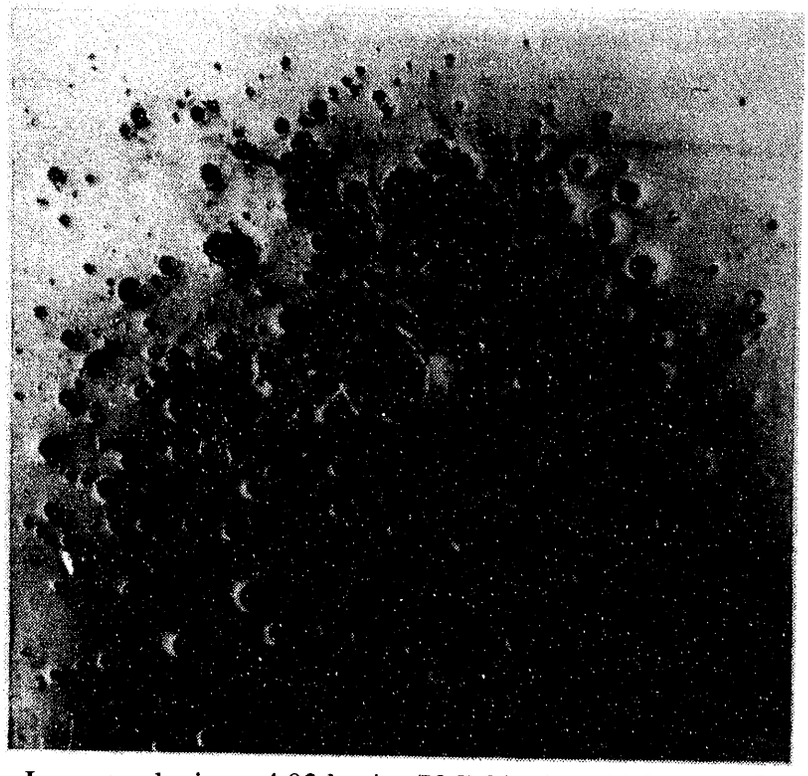

b. Test 24 - Impact velocity = 4.03 km/s - PMMA plate thickness = 9.47 mm. Diffused splash damage.

Figure 27. Secondary target damage modes.

Computer solutions of high velocity impact on primary targets, and subsequent interactions of the resulting ejecta with secondary targets have been performed (*e.g.* Chhabildas, *et al.*, 1993). These solutions intentionally ignore the physics of fragmentation in the condensed phases of the matter. Instead, divergent motions imparted to the removed ejecta lead to a rarefaction of the matter as it propagates through the space between primary and secondary targets. Some computational lumping of the matter during the rarefaction process may occur but this unintentional fragmentation is a consequence of numerical instabilities, or physical instabilities which do not adequately describe the material response during fracture and fragmentation. Impact of this debris continuum onto secondary targets leads to impulsive loadings and material motions which do not, in general, provide the desired details of target damage. For example, secondary target damage through fragment perforation cannot be predicted through continuum solutions.

Computational methods for treating fragmentation in the high-velocity impact of a projectile with a primary target were discussed in the previous section of this report. The available capabilities provide for the statistical size, velocity, and trajectory of a cloud of impact debris fragments over the region of interest. Therefore, it is also possible, in principle, to initiate a second computational solution, describing in detail the motion and interaction of a discrete collection of fragments with a secondary target — the size, velocity, and trajectory data from the first calculation providing the starting condition for the second. Solutions of this type provide insight into details of the multiple impact processes, and are discussed in the following section of this report.

Before examining the simulation of the impact of an explicit fragment cloud onto a target, possible intermediate methods for addressing secondary target damage are considered. One possibility is to retain a continuum description of the impact fragment debris, and determine the limitations of such an approach. However, conditions leading to fragmentation and the fragmentation process will be treated as accurately as current theories will permit and statistical fragment size properties will be advected with the material as internal state variables. Thus, the computational approach retains a continuum representation of the fragment debris cloud, while the discrete fragment characteristics are transported with the continuum cloud as hidden variables.

A difficulty arises with a continuum description of a fragment cloud upon interaction of the system of fragments with a secondary target. Momentum is exchanged at the immediate interface between the continuum fragment cloud and the secondary target. This momentum coupling process does not adequately model the interaction behavior of a discrete fragment cloud with the target. Individual fragments can channel to some depth into the target, depositing momentum along the path of penetration. If the target is thin, full penetration can occur with only a portion of the particle momentum transferred to the target. Thus, in effect, a secondary target can be semipermeable to the mass and momentum of a high-velocity fragment cloud.

There are, however, examples in the field of continuum physics of the type of interpenetration suggested above. In the continuum description of a beam of laser light or atomic ions, the energy and momentum are deposited at some depth into a stationary target — the extent of penetration is a physical property characteristic of the penetrability of discrete light or atomic particles into the specific target material. Another, perhaps useful, continuum description of

matter is that of two-phase flow in material mixtures. Water, for example, can flow through a bed of solid particles. Momentum and energy is exchanged gradually between the two materials through coupling laws which include appropriate friction or viscosity properties.

To assess the applicability of these later examples to the problem of secondary target impact and damage an interaction which resembles the present experimental situation will be considered. In the higher-velocity experiments in the present study a pancake-shaped cloud of several hundred steel fragments was created which underwent normal impact on an aluminum target plate. Accordingly, consider a planar sheet of fragments which is undergoing impact on a plate of target metal. For this analysis, the thickness of the fragment sheet is assumed to be unimportant (*i.e.* ignore the possibility of multiple impacts in the same site). The fragment cloud is characterized by an impact velocity V_o, the number density of particles per unit area n_o, and mass per unit area m_o. The average particle mass is then $\mu = m_o/n_o$.

If treated as a conventional continuum, planar impact will couple a thin impulsive load into the target at the impact interface. Depending on impact intensity and target properties spall damage, or, if the fragment debris is finite in lateral extent, plugging, may occur. Such a treatment is not sufficient to address perforation.

A more detailed analysis of the impact interaction event requires consideration of the microscopic target impact effects. Again, depending on impact velocity, and fragment and target properties, a range of impact physics can be encountered. Here, the development will be restricted to hard (steel) fragments at velocities over which further fragment breakup during penetration does not occur. Target material is plastic (aluminum). Under such conditions deep penetration of individual steel fragments into the aluminum target can be expected as the particle comes to rest.

The depth of penetration of hard spherical particle can be calculated with reasonable accuracy from Equation 5 with a target strength resistance term R included,

$$m\frac{dV}{dt} = (\frac{1}{2}\rho V^2 + R)A. \qquad (31)$$

Integration of Equation 31 and solving for the depth of penetration, λ, provides,

$$\lambda = \frac{2}{3}\frac{\rho_p}{\rho}D\,ln\,(1 + \frac{\rho V^2}{2R}). \qquad (32)$$

In Equation 32 D is the fragment diameter, while ρ_p and ρ are fragment and target densities, respectively. (Note that $R \approx 2.5Y$ for 6061-T6 aluminum provides a best fit to the penetration data of Trucano and Grady (1985).) Values of $R \approx 2.6$ - $3.0\,Y$ are calculated for static punch tests.

Thus, the mass and momentum of a characteristic fragment of size D would not be deposited at the impact surface but would instead be deposited along a penetration channel to a depth λ. A particle-to-particle variation in the depth of penetration is, of course, expected for several reasons: First, there is a statistical variation in particle size in the fragment cloud. Second, some degree of reinforcement and interference as a consequence of the close proximity of penetrating particles would be expected to influence specific penetration events.

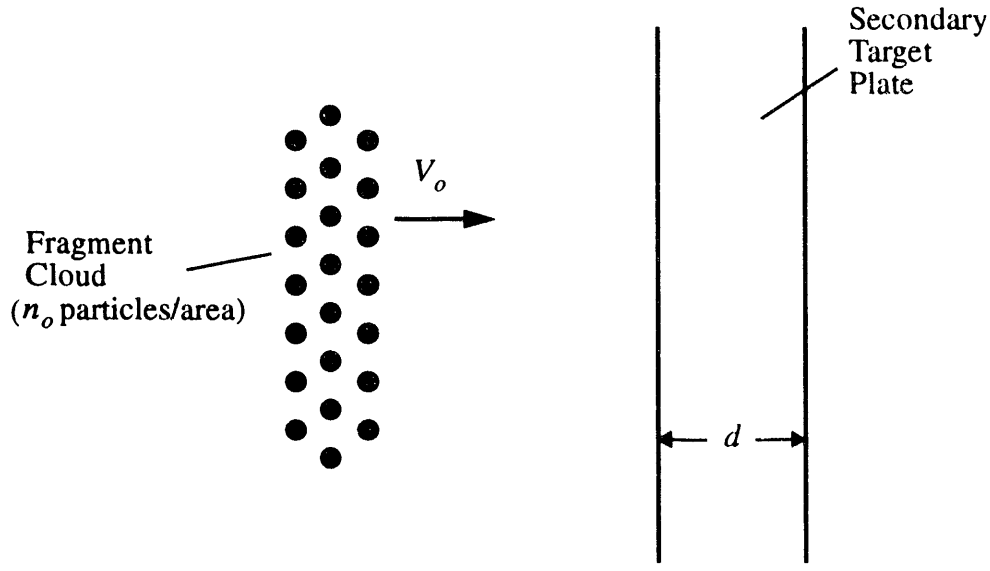

Figure 28. Continuum debris cloud.

In the analysis of secondary impact and damage consider a cloud of debris fragments (depicted in Figure 28) to be a continuum, but with mass and momentum which are initially deposited exponentially in the target to a characteristic depth λ. Thus the cumulative fragment mass as a function of depth into the target is,

$$m(x) = m_o (1 - e^{-x/\lambda}), \tag{33}$$

and the initial cumulative momentum is,

$$p(x) = m_o V_o (1 - e^{-x/\lambda}). \tag{34}$$

The latter relation assumes that a particle momentum is deposited at the final depth of penetration. If the mass of the deposited fragments can be ignored (reasonable if $m_o \ll \rho\lambda$ where ρ is the target material density), then the initial velocity profile in the secondary target plate can be calculated,

$$v(x) = \frac{m_o V_o}{\rho\lambda} e^{-x/\lambda}. \tag{35}$$

A continuum impact in which the theory provides for the deposition of momentum at depth within the secondary target will differ in several ways from the direct coupling of momentum at the impact interface. First, the shape of the impulsive load will be different and, consequently, details of the behind target spall will differ. Second, if the target plate is sufficiently thin, the model would predict that a portion of the debris mass, and momentum, could fully penetrate the target. Only a portion of the fragment debris cloud momentum would be deposited in the target plate. For example, for a plate of thickness d, Equation 33 would predict that a mass per unit area,

$$m = m_o e^{-d/\lambda}, \tag{36}$$

would pass through the plate and Equation 34 would imply that the impulse imparted to the secondary target would be reduced to,

$$p(d) = m_o V_o (1 - e^{-d/\lambda}) \tag{37}$$

Consider one of the present experiments in which the steel fragment debris had an average fragment size of 1 mm (~250 fragments) and impacted at a velocity of 4 km/s. Equation 32 would suggest a characteristic penetration depth of about $\lambda = 6$ mm. Equation 36 would predict that about 30 fragments (~10%) would perforate a 12.7 mm aluminum plate. This is about one order of magnitude larger than the number of observed perforations in the present tests. This poor agreement implies that an exponential distribution of the mass and momentum is probably a poor representation of the deposition profile. Particle breakup may be occurring at these impact velocities in which case the estimate of λ is most likely too large. Furthermore, the theory does not provide for a dependence of the characteristic penetration depth on the density of particles (areal density m_o).

Clearly there are some obvious weaknesses in the present tentative theory in which a continuum interaction of a fragment debris cloud with a secondary target is considered, but where internal state variables characterize the fragmentation state and determine the diffusion and deposition of the cloud mass and momentum into the target. Nevertheless, in lieu of the present lack of models and computational methods for accurately convecting debris from an initial impact to incidence on a secondary target, further development of a theory to utilize these ideas to address secondary target damage problems may be worthwhile.

H. Numerical Analysis of Debris Cloud Impact on Aluminum Target

An explicit approach to examining the effects of a debris cloud impacting a secondary target is to define each particle in the cloud and compute the excavation of the target resulting from the cumulative cratering of each particle. In this section, impact of the particles in a debris cloud representing those formed in Test 5 is numerically simulated with CTH. This example provides insight into the nature of multiple impacts and the influence of the cloud parameters on the target response. For the present generation of computational hardware, this three dimensional problem requires significant memory and execution time, and is not yet a routine method of debris cloud analysis.

The calculations of debris characteristics from the initial impact of the steel sphere with a PMMA target were discussed in Section F. The size and number distribution characteristics of the debris that was produced in that impact simulation were represented in Figure 19, Figure 20, and Figure 21. In principle, a desirable technique would permit the extrapolation of the steel debris from the initial impact with the PMMA target to the location of the next target - the aluminum witness plate in this example - complete with spatial and size distribution of the particles in the debris cloud. The extrapolation step has not been taken yet; although the expansion velocities are available, the axial dimensions of the debris cloud have not been determined from the simulation,

primarily because of a lack of knowledge regarding the particle interactions during the time just after sphere breakup commences. In addition, the total number of particles computed in the example tended to be too large, based on qualitative analyses of the radiographs.

In order to define a tractable problem, the number of particles in the debris cloud was constrained to be about 300, with a particle size distribution that was assumed to be exponential. That is, the number of particles of a given mass was based on an exponential function of the particle mass, normalized so that the total mass of the steel particles summed to the original mass of the steel sphere, M, of 1.05 g. The maximum particle size was less than 2 mm, corresponding to a mass of less than 40 mg for the largest particle. The number of particles of mass m, N_m are distributed according to bin size intervals of Δm, and determined from

$$N_m = \frac{N_0}{\mu} e^{-m/\mu} \Delta m, \qquad (38)$$

where N_0 is the total number of particles, and μ is the average particle mass, related to the total mass of the original steel sphere by $M = N_0 \mu$. For the present analysis, the average particle mass is about 3.5 mg, and the average particle size (diameter) is about 0.76 mm.

The dimensions of the debris cloud envelope at the location of the aluminum witness plate were determined from the positions and times of the radiographs relative to the position of the witness plate. On this basis, the cloud, assumed to be a circular disk, has a diameter of about 55 mm, and a thickness of about 10 mm.

The impact velocity of the particles onto the witness plate is 4300 m/s, and the outer expansion velocity is about 270 m/s (*cf* Table 2). The coordinate positions of each particle were assigned with a random number generator: an (x,y,z) position was assigned, and that coordinate was checked to ensure it was interior to the envelope, and then compared against all previous particles for overlap; if no overlap occurred, then the coordinates were retained; otherwise a new set was assigned and rechecked. This procedure was followed for each of the 300 particles until all the particles were contained within the envelope, and no overlap existed. In addition, each particle was assigned an normal impact velocity of 4300 m/s, as well as a radial velocity based on the expansion velocity times the particle position radius normalized to the envelope radius.

In this three dimensional calculation, the normal impact direction of motion was in the x-coordinate, and the two lateral coordinates were y and z. The physical space of the cloud and 12.7 mm aluminum witness plate was defined by -2 mm < x < 28 mm, -37.5 mm < y < 37.5 mm, and -37.5 mm < z < 37.5 mm, with uniform 0.3 mm cubical cells, resulting in about 6.25 million cells in the calculation. Views of the initial conditions are shown in Figure 29. One can note that in this simulation there are clear differences from the radiographs in Figure 2 and Figure 7. Of particular note is the fairly regular distribution of particles on the periphery of the radiograph in Figure 7. The resolution of the calculation limits the number of cells to about 2 to define the average particle dimension. Consequently, some of the particles will be shapeless masses impacting the target rather than well-defined spheres. At these velocities, however, the initial

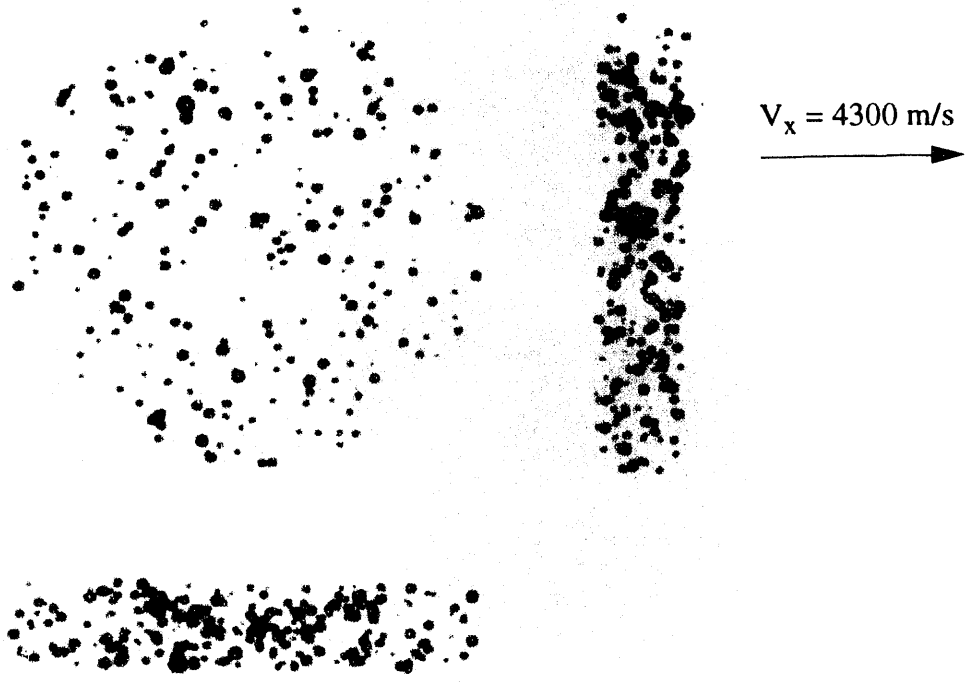

Figure 29. Initial conditions of the 297 debris cloud particles.

shape of the particle is not of primary importance in determining the excavated crater. An edge view of the initial conditions is shown in the upper section of Figure 30.

By 8 μs the craters have all been formed and the steel particles exhausted their momentum in the excavation process. An edge view of the target plate at this time is shown in the lower section of Figure 30. The jagged crater lip formation is evident in this view. No particles have perforated the aluminum target, but a significant bulge is observed to have formed on the back side of the target. A perspective top view of the craters formed is shown in Figure 31. (In this view, the edges have been trimmed from the aluminum plate to include only that material that contains craters.) Although there is clearly significant coupling between craters, extensive contiguous original surface material remains. All these observations are consistent with the recovered witness plate. An estimate of the computed excavation volume of aluminum is 2.75 cm^3. There are many evidences of multiple impacts forming craters, and rare instances of crater connectivity below the surface.

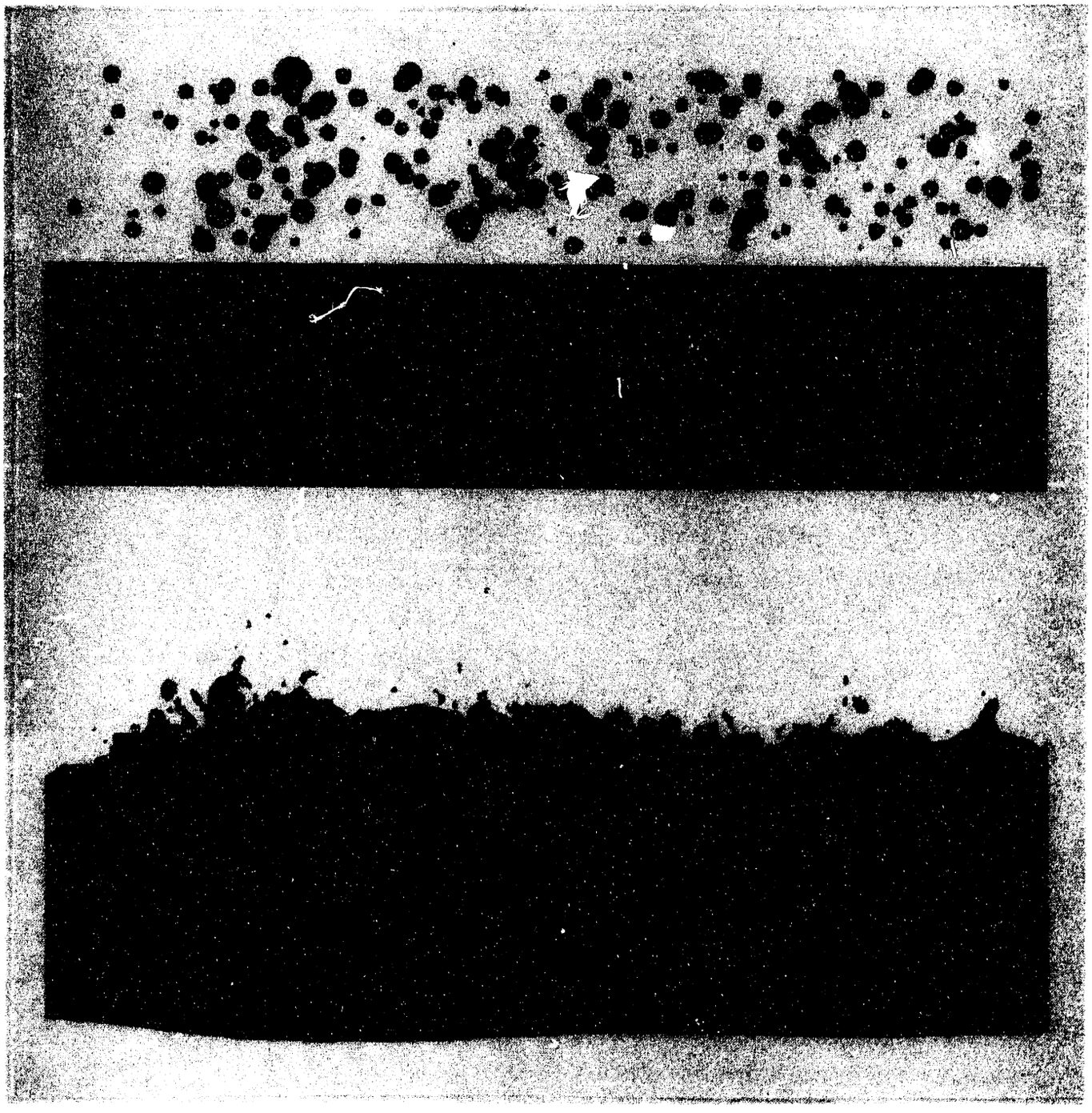

Figure 30. Edge view of the aluminum witness plate at 0 and 8 μs.

Figure 31. Perspective top view of craters at 8 μs (Stereo cross-eyed pair).

III. COPPER SPHERE IMPACT ON STEEL TARGETS

An impact configuration involving two distinct metals for projectile and target was defined with the specific intent of obtaining radiographic diagnostics of the debris cloud shortly after perforation was complete, and to recover the fragments for post-shot analysis. In the present investigation we have undertaken a study of the high-velocity interaction of a copper projectile and a steel plate in the velocity range of 3.5 to 5.0 km/s for the purpose of testing the wave-propagation code. High-resolution radiography has been used to diagnose the crater formation and debris motion within the time frame accessible to computational simulation. Both normal and oblique impact experiments have been performed to test the full three-dimensional capabilities of the wave propagation code. Additional diagnostics have also addressed further details of the fragment size and trajectory properties of the metal debris. The radiographs were successfully obtained. The particles were also successfully captured in foam blocks.

The major effort of this computational wave code analysis was focused on an oblique impact experiment performed at an impact velocity of about 4.5 km/s. Simulated radiographs (projected density plots) were constructed and compared directly with experimental x-ray data.

A. Experimental Configuration and Materials

The experimental configuration for the impact fragmentation tests is shown in Figure 32. Saboted OFHC copper spheres were launched at velocities between about 3 to 5 km/s with a two-stage light-gas gun system. The launch tube diameter was 12 mm. Lexan sabots were separated from the copper spheres through forces produced by a slight back pressure of nitrogen in the gun

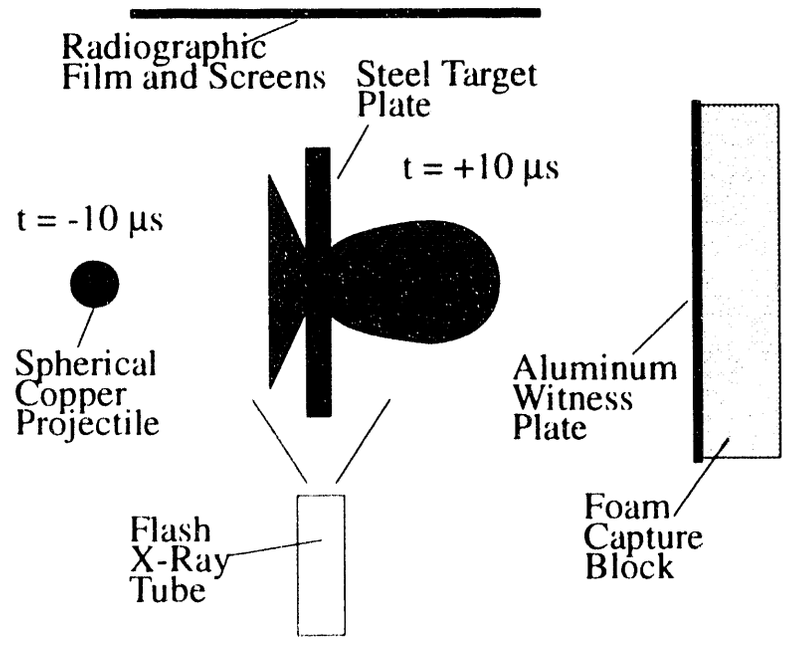

Figure 32. Experimental configuration for radiographic and fragment witness diagnostics of copper-on-steel impact fragmentation experiments. (Timing is representative of a 4.5 km/s impact.)

range section. Sabot segments were trapped upstream and did not reach the target impact chamber. Velocities of the copper spheres were measured to ± 2% accuracy by recording of the time interval during passage between two magnetic coils of known separation. Impact of the copper spheres occurred in the target chamber at approximately the center of a 75 mm by 75 mm square steel target plate of thickness 5.60 mm. Critical experimental parameters are provided in Table 7.

Table 7: Experimental Conditions

Test	Impact Velocity	Copper Mass	Copper Diameter	Plate Thickness	Plate Inclination	X-Ray Times
#	km/s	g	mm	mm	degrees	μs
Test 1	4.96	1.20	6.36	5.61	0.0	11.6
Test 2	4.52	1.20	6.35	5.60	30.8	11.6
Test 3	3.43	1.20	6.36	5.60	0.0	131.4

In the reported experiments, spheres of four nines pure copper with a 0.2% offset yield strength of about 270 MPa were used for the impacting projectiles. Target plates were prepared from 4340 steel (AMS 6359 plate stock) heat treated to a Rockwell hardness of 41-42. In all experiments a copper sphere 6.35 mm (1/4 in.) in diameter was used. The measured mass was 1.20 ± 0.001 grams. The density of the steel is 7850 kg/m^3, yield strength is 2.0 GPa, fracture toughness is 30 to 40 MPa$\sqrt{m}$, and elastic modulus (Young's) is 200 GPa, with a Poisson ratio of 0.29.

Two impact configurations were tested in the present study. In all tests the steel target plate was supported by a bolt attached to one corner. In Tests 1 and 3 the plates were positioned so that the plane of the plate was vertical (identified as 0.0 degrees of inclination in Table 7). Normal impact within ± 1 degree was achieved in these tests. For Test 2 the top of the plate was tilted out of the vertical by 30.8 degrees achieving an oblique impact of the copper sphere on the target plate.

Impact ejecta in Tests 1 and 2 was diagnosed approximately 11.6 μs after impact on the front surface of the target plate. One 150 keV flash x-ray tube, placed approximately 1.5 m from the line of projectile travel, provided orthogonal shadow graphs of the fragment debris, as shown in Figure 32. Impact delays were determined from electrical shorting impact switches placed on the front of the target plate. The x-ray film cassette, using Kodak Direct Exposure film backed by a Quanta Fast Detail screen, was stationed about 15 cm from the debris trajectory.

For Tests 1 and 2 the x-ray image was centered on the target plate and the early-time record provided detailed geometry of crater formation, and both front and back surface ejecta debris. In Test 3 a late-time image of back surface fragments was obtained which provided more detailed information on particle number and disposition.

An assembly to witness and capture behind target fragment debris was also included in the experimental configuration. A block of polyurethane foam (30 cm on a side and 7.5 cm in thickness) with a density of 320 kg/m^3 was positioned 25 cm behind the target plate. A sheet of

30 cm by 30 cm aluminum foil 0.075 mm in thickness was placed on the front of the foam block and provided a witness measurement of the number and distribution of debris fragments. Fragments were captured within the foam block and were interrogated with post-test static radiography.

B. Experimental Results

Radiography

The radiograph for Test 1 at 11.6 μs corresponding to a normal impact at 4.96 km/s is shown in Figure 33. The leading edge of the behind target debris is moving at a velocity of approximately

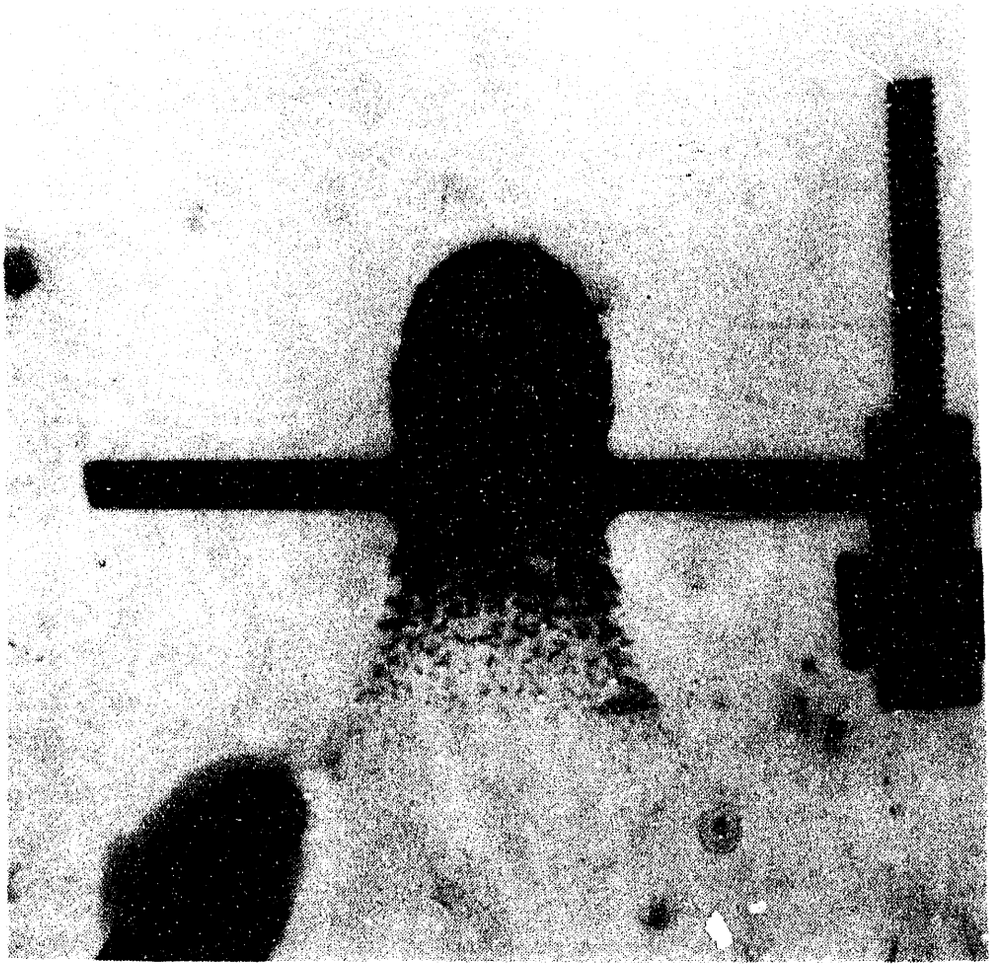

Figure 33. Radiographic record of 4.96 km/s normal impact at 11.6 μs (Test 1).

2.3 km/s, slightly less than half of the initial impact velocity. Velocities in excess of 3 km/s were determined for the highest velocity fragments in the back-splash debris. In contrast, large fragments associated with the lip of the spall ring (both front and back of the target plate), emerging from the peripheral region of the penetration spall crater, indicated an axial velocity component of about 0.4 km/s. At the 11.6 μs time into the motion, fragments appear fully formed although high fragment density precludes resolution of individual particles.

The radiograph resulting from the Test 2 oblique impact experiment at 4.52 km/s is shown in Figure 34. The impact debris in this test was also imaged 11.6 μs after impact. The leading edge of

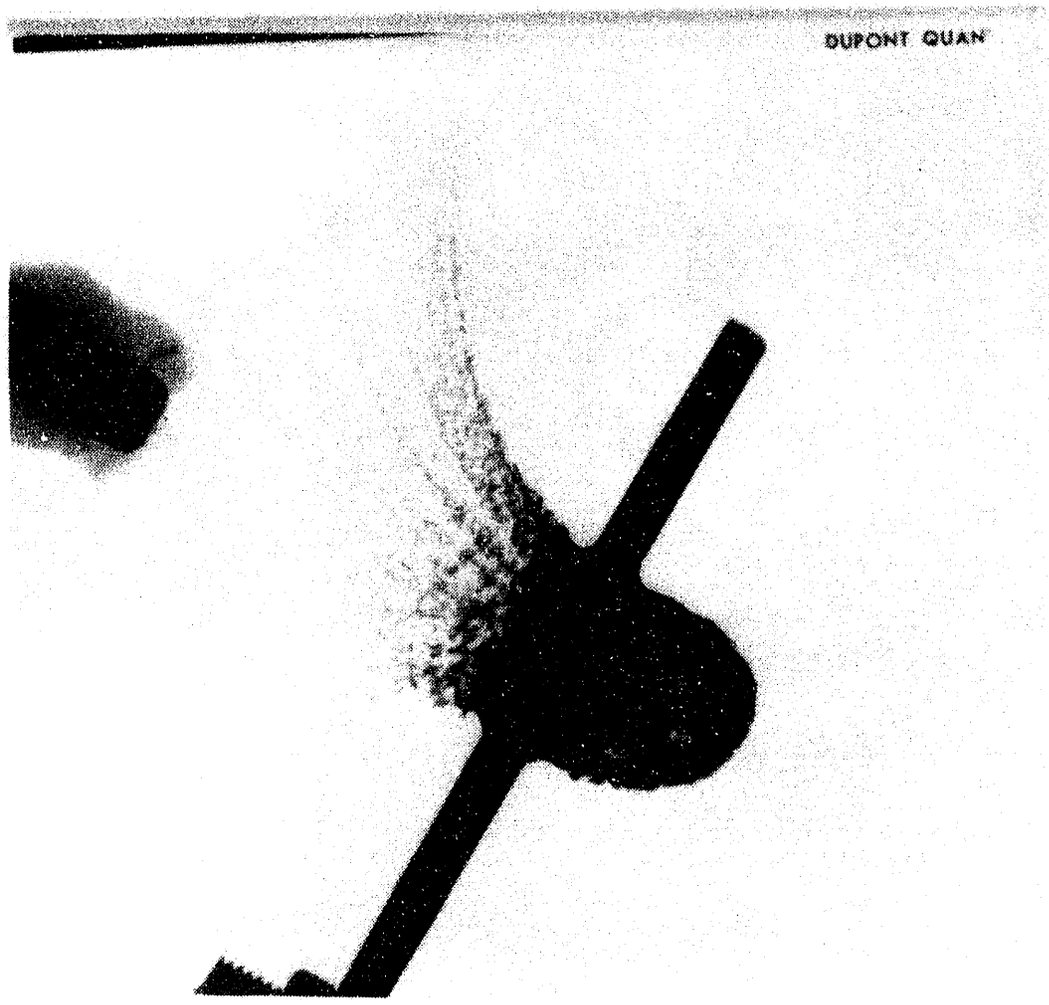

Figure 34. Radiographic record of 4.52 km/s oblique impact at 11.6 μs (Test 2).

the behind-target debris is moving at approximately 1.8 km/s. A slight asymmetry in the envelope of the behind-target ejecta debris due to the oblique impact is noted, and most certainly has more material on the upper side of the cloud than on the lower side, where there are observed to be more spaces between fragments. From the radiograph, it is not possible to discern the interior character of the debris cloud. Details in the back-splash debris from the impact surface associated with jetting caused by the spherical impact are particularly apparent. The curved traces of debris on the impact face of the target originate from a radially increasing crater, and are finest at the time of impact, and increase in size as the crater becomes larger. A ray pattern associated with the circumferential instability and breakup of the jet material is also observed. Note the defined spacing of these rays of debris, their circumferential spacing determined by the strain rates of the expanding crater. Leading fragments in the back-splash debris are traveling at velocities near 6 km/s.

Figure 35. Radiographic record of 3.43 km/s normal impact at 131.4 μs (Test 3).

In Figure 35 the radiograph for Test 3 shows the behind-target debris for a similar normal impact event late in time. The low spatial density of material at this time allows nearly full

resolution of all fragments. Impact velocity for this test was 3.43 km/s, and the velocity of the leading edge of the debris cloud inferred from the radiograph is approximately 1.6 km/s. The majority of the observable fragments are uniformly distributed through an elliptical cloud. They have a statistical mean projected area very close to 1 mm^2 with a remarkably narrow size distribution. Thus these particles would constitute only about 2 grams of the approximately 13 g of the target ejecta and projectile mass. The remaining mass would be the back splash fragments and, primarily, the large spall ring fragments residing close to the target plate in the Figure 35 radiograph.

Penetration Crater

Photographs of the impact and exit side of the penetration crater for the oblique impact experiment (Test 2) are shown in Figure 36. Structure of the normal impact crater for Tests 1 and

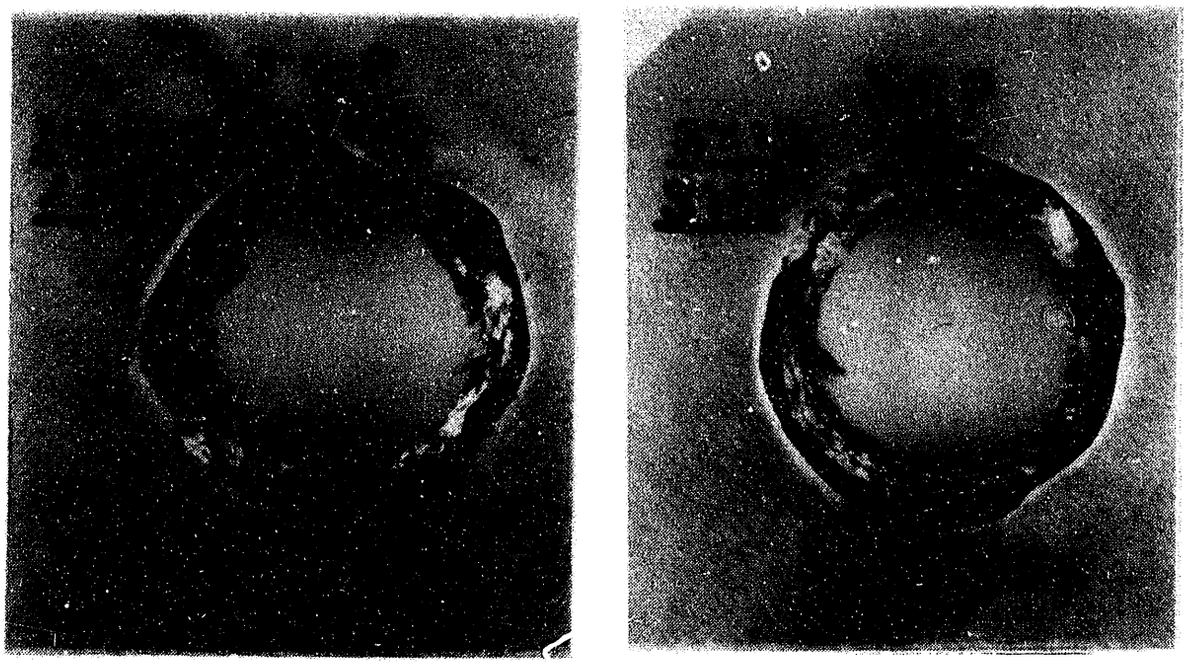

Figure 36. Penetration crater for 4.52 km/s oblique impact experiment.

3 were visually identical to that shown in Figure 36. In Test 2 the top of the plate was tilted away from the projectile trajectory to achieve the approximately 30 degree oblique impact configuration. The crater shows an approximately circular penetration hole and a spall ring region on both impact and exit sides out to a somewhat larger spall lip radius. Penetration damage on exit and impact sides

showed no visual differences. Crater hole and spall lip diameters for the three impact tests are provided in Table 8.

Table 8: Experimental Parameters

Test	Initial Plate Mass	Plate Mass Loss	Hole Diameter	Crater Lip Diameter
#	g	g	mm	mm
Test 1	250.9	19.3	19 ± 1	27 ± 2
Test 2	251.7	16.6	18 ± 1	26 ± 2
Test 3	250.0	10.7	15 ± 1	22 ± 2

Target plates for impact Tests 1 and 2 were also sectioned through the center of the crater and polished for metallographic examination. For the Test 2 specimen the crater was sectioned vertically to expose possible asymmetry in the damage modes due to the oblique impact. The photograph of the Test 1 target plate shown in Figure 37 is representative of the results. The extent

Figure 37. Metallographic section through center of penetration crater for 4.96 km/s normal impact experiment.

of the spall ring region is indicated. Close examination revealed extensive shear banding and small-scale cracking. The central spall crack seen in Figure 37 circumscribed the penetration crater, extending into the plate about 3 to 10 mm. This central spall crack was not observed in the oblique impact experiment.

Mass loss from the crater region was determined by weighing target plates before and after the impact tests. Results provided in Table 8 show a consistent monotone increasing trend with impact velocity.

Witness Plate and Capture Data

The passive methods used to interrogate the behind-target fragment debris were also informative. The foam block and foil positioned behind the target were sufficient to intercept a majority of the high-velocity behind-target debris. The large spall ring fragments which were ejected with a large angle with respect to the projectile trajectory were not captured by this method.

First, the aluminum foil placed at the front of the foam block provided an excellent diagnostic of the fragmentation pattern and intensity. Penetration craters in the foil provided only a rough indication of size, however, since the hole areas were somewhat larger than the corresponding projected fragment area. The number density of fragments was readily determined from the witness foil, however, and provided valuable data for validating computational fragmentation codes since the mass flux at a point in space is readily calculated in the wave-code analysis, and hence couples fragment size and number.

It should be noted that the qualitative fragment size distribution, as inferred from hole size data in the witness foil, was strongly bimodal in character. A broad spread (covering most of the witness foil) of larger fragments (holes) ranging from about 1 mm to about 5 mm in size was observed. In addition an intense spray of very fine particles (hole size between 20-200 μm) within about a 10 cm central region was witnessed by the foil. This effect was intense in Tests 1 and 2, but very weak in the lowest velocity Test 3.

A particle number density for fragment hole sizes of approximately 0.5 mm and larger was determined from witness foils from the three tests. These fragment number data are plotted in Figure 38. The data are plotted as a function of radius from the line of projectile travel. This representation is appropriate for Tests 1 and 3 because the normal impact conditions imply rotational symmetry. For Test 2 slight skewing of the debris pattern was noted due to the oblique impact, thus number density both vertically upward and downward from the projectile line are plotted in Figure 38.

Static radiographs of the foam blocks used to capture the debris ejected from the target plate were taken. Views in the direction of impact are shown in Figure 39 and Figure 40. Note the distribution of particles through the diameter of the cloud. There is a large contrast in the apparent average fragment size between Figure 39 and Figure 40. The large impact velocity of Test 1 (4960 m/s) results in relatively small fragments, and many deep craters in the foam (Figure 39). The much lower impact velocity of Test 3 (3430 m/s) results in an apparently larger average fragment size, and considerably fewer deep craters in the foam block (Figure 40). The center region of the higher

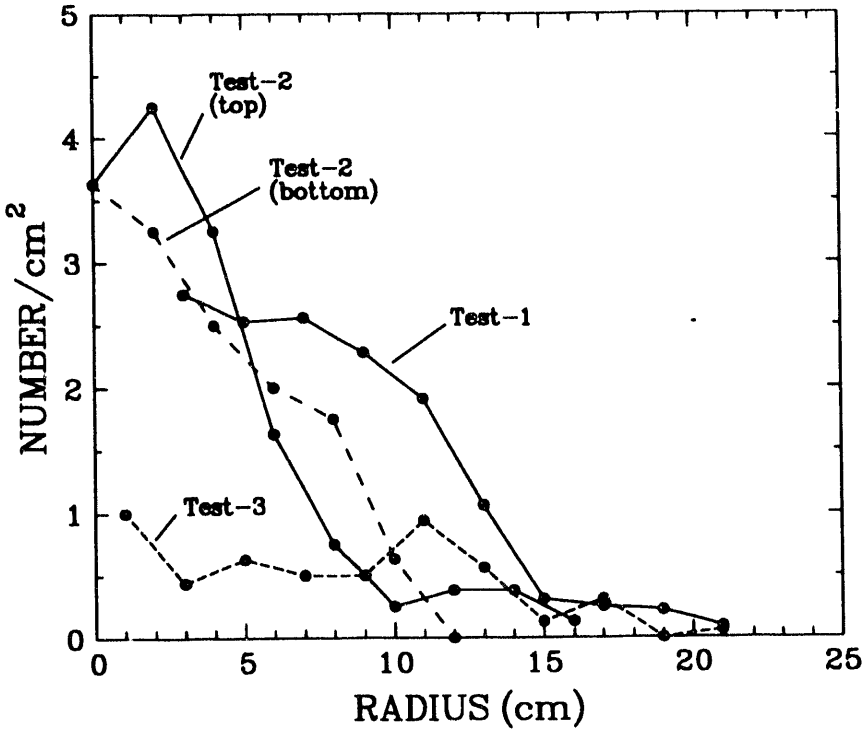

Figure 38. Number of fragment density data determined from penetration craters in aluminum witness foils.

velocity impact is nearly devoid of larger fragment sizes, those appearing in an annular ring about the center.

The radiographs were image processed (See Appendix C) and the fragment areas reduced to digitized data (Figure 41). The abscissa is projected area of the fragment. The higher impact velocity has nearly 600 fragments recorded, whereas the lower impact velocity has only about 300 fragments recorded in the foam blocks. There is a crossing of distributions in the cumulative number data shown in Figure 41. This is a consequence of approximately equal masses of material being partitioned into two distributions - one with a larger number than the other. The distribution with more fragments has the mass concentrated nearer the small fragment end, with a steeper slope to the large fragment end (assuming exponential distributions). In fact the data are quite linear in over much of the fragment area range, and are represented quite readily with an exponential distribution. The larger chunky fragments are presumed to be pieces of the spall ring that break off and move at relatively slow velocities compared to the rest of the fragments.

At these impact velocities, there is sufficient shock heating locally to cause melt of some of the metal (primarily copper), and the penetration of these fine particles causes a network of fine holes in the aluminum witness foil (Figure 42). A representative section of the impact foil from Test 2 was image-processed, and the size distribution data (actually foil hole areas) are provided in Figure 42. The dominant hole diameter is about 50 μm, approximately consistent with predicted break-up sizes of liquid melt fragments.

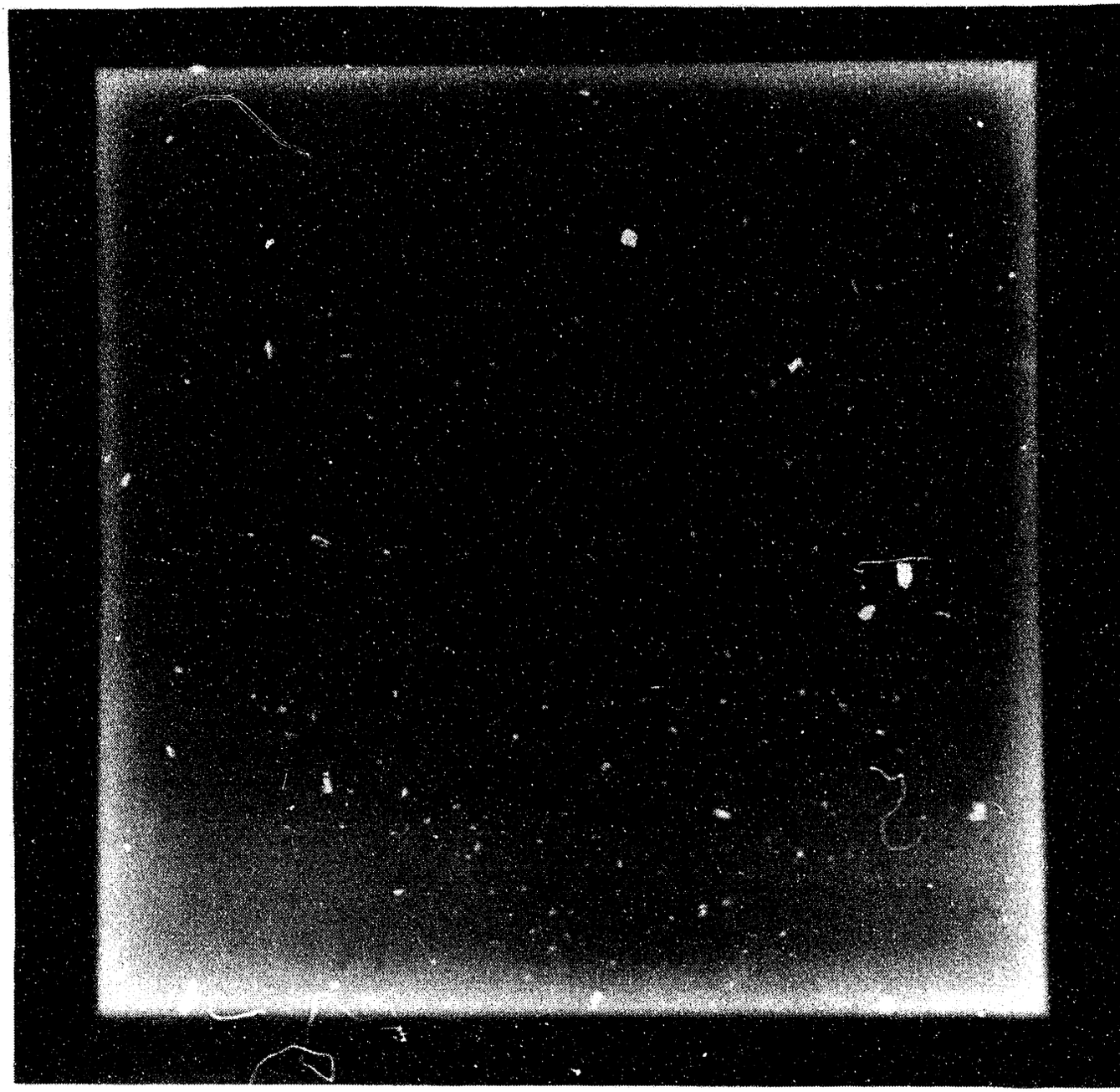

Test 1 Static Radiograph of Debris in 12" by 12" Foam Block ~

6.36 mm Copper Sphere Impact Velocity:	4960 m/s
Steel Target Thickness:	5.61 mm

Figure 39. Static radiograph of foam block used to capture behind-target ejecta fragments: Test 1 (Copper sphere impact velocity = 4960 m/s).

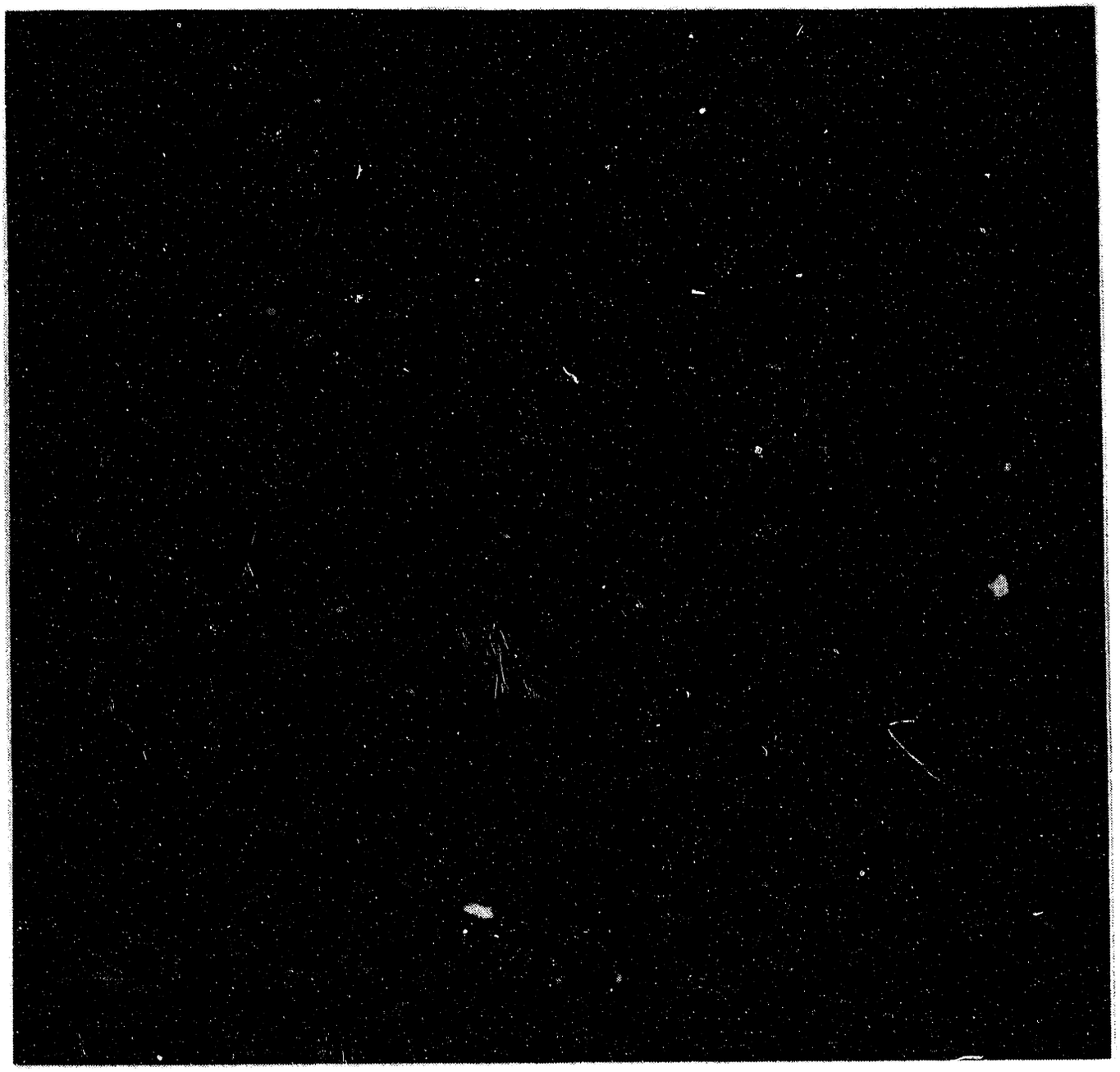

Test 3 Static Radiograph of Debris in 12" by 12" Foam Block ~

6.36 mm Copper Sphere Impact Velocity:	3430 m/s
Steel Target Thickness:	5.60 mm

Figure 40. Static radiograph of foam block used to capture behind-target ejecta fragments: Test 3 (Copper sphere impact velocity = 3430 m/s).

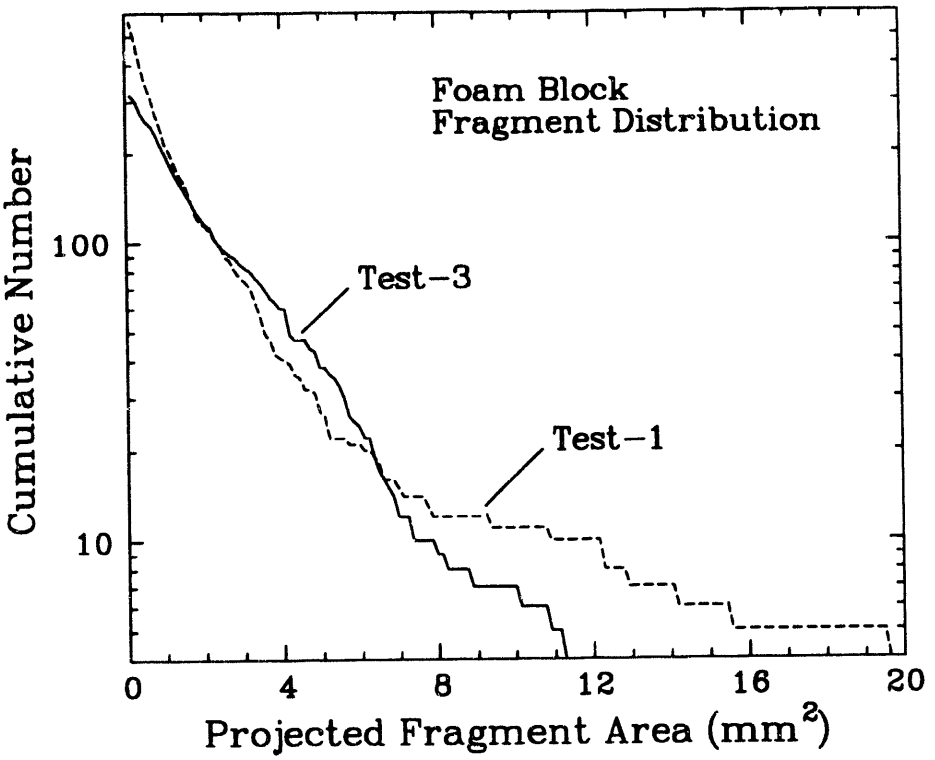

Figure 41. Fragment distribution data for normal impact Tests 1 and 3 determined from static radiographs of fragments captured in foam blocks.

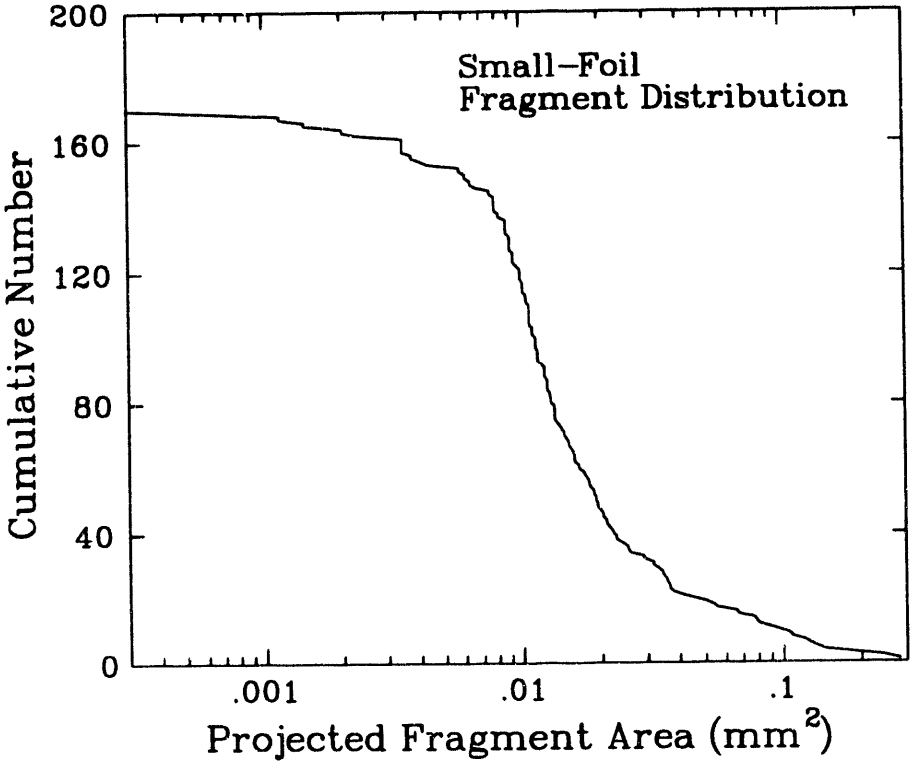

Figure 42. Statistical particle size data for fine spray particles determined from aluminum witness foil.

C. Numerical Analysis of the Copper Sphere Impact

The primary objective of the impact penetration experiments and radiographic diagnostics was to provide spatially resolved data of the crater formation process and impact ejecta motion for the purpose of validating three-dimensional (3-D) computational codes in the regime of high-velocity material interaction. The Eulerian wave propagation code CTH (McGlaun, *et al.*, 1990) was again the computational tool of choice in the present investigation. The computational study focused primarily on the oblique impact experiment (Test 2) which provided the most stringent test of the 3-D features of the wave propagation code.

In the oblique impact geometry that was simulated, there is one plane of symmetry, a plane through the axis of impact, appearing in plan view like the sketch in Figure 32. A computational resolution of 0.2 mm was the best that could be obtained, based on available computer storage. This resulted in just over 6 million computational cells, each 0.2 mm cubes. The material properties for the copper and steel are provided in Table 9. The $\alpha \leftrightarrow \varepsilon$ solid-solid polymorphic phase transformation was included for the steel, a phase transformation that occurs at about 13 GPa, and has been shown to be an important factor in certain kinds of impact scenarios (Bertholf, *et al.*, 1975). The low- and high-pressure linear shock velocity - particle velocity parameters are included in Table 9. The deviatoric behavior was modeled as elastic - perfectly plastic, with the yield strengths indicated in Table 9. Fracture in the computational analysis was treated by introducing void into the computational cell when a principal stress exceeded the tensile fracture stress until the stress state in that cell was reduced to zero.

Table 9: Material Parameters Used For Copper Sphere Impact

	Copper	Hard Steel
Density (kg/m^3)	8920	7850
Bulk sound speed (m/s)	3904	4620
Linear shock velocity - particle velocity slope	1.489	1.74 α-iron 1.64 ε-iron
Gruneisen coefficient	1.99	1.75
Yield strength (GPa)	0.7	2.0
Poisson ratio	0.351	0.29
Fracture stress (GPa)	0.3	1.2

The calculation was initiated with the copper sphere in contact with, and surface tangent to, the steel target plate. The initial velocity vector of all cells within the copper sphere was directed into the target plate 30 degrees from the target normal, and with a magnitude of 4.52 km/s. Impact stresses are nearly 120 GPa. A sequence of images at the symmetry plane is recorded in Figure 43. In these figures, the sphere is moving from bottom to top. At 2 μs, the crater has begun to form, and the rear of the target is bulging. At 4 μs, the target is nearly perforated, with a spall region visible in the steel layer at the top of the bubble. Although the impact was oblique, already there is

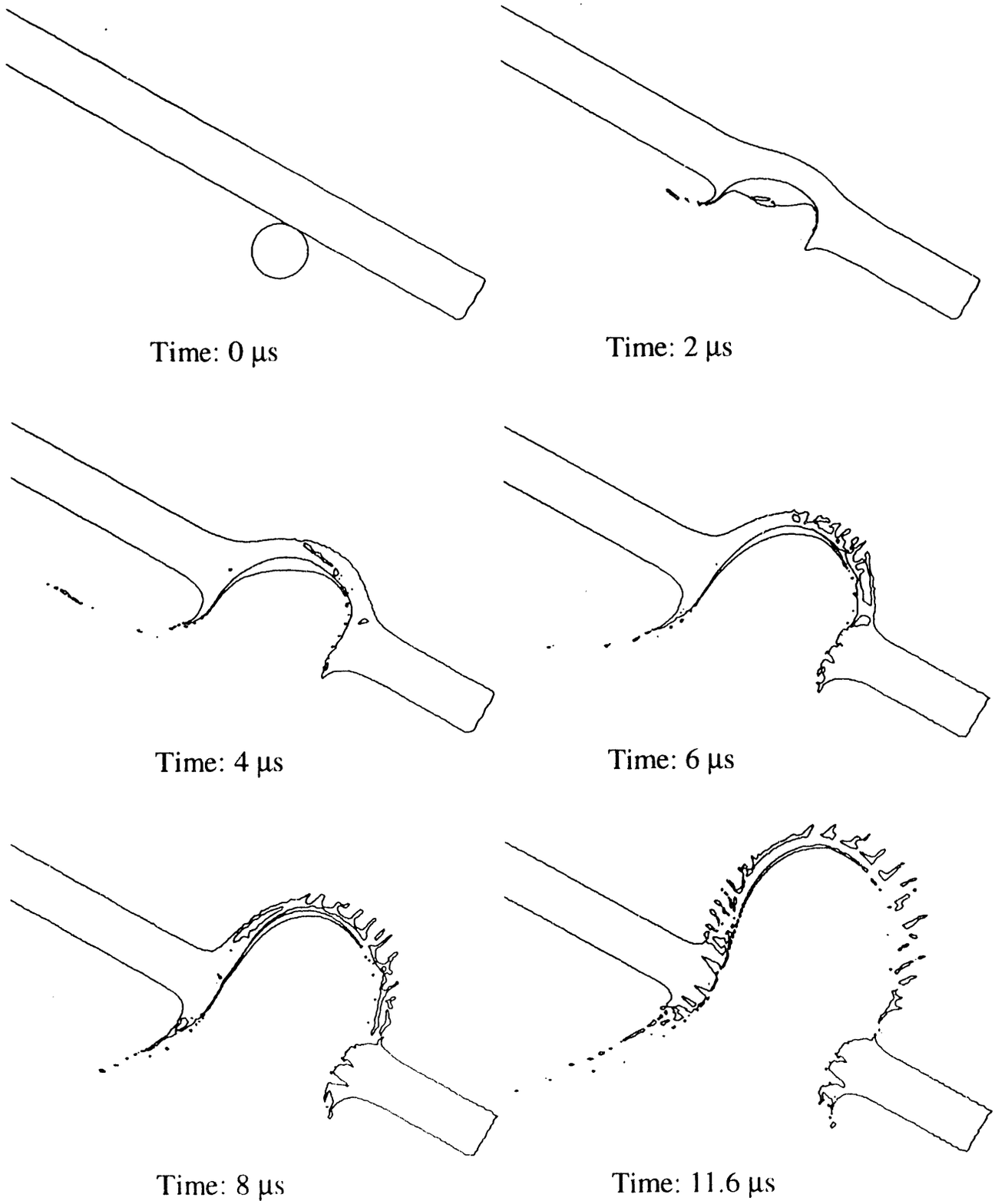

Figure 43. Symmetry plane views of the impact of the copper sphere onto an inclined steel target. Times are 0, 2, 4, 6, 8, & 11.6 μs.

evidence of hole symmetry forming that has the appearance of normal impact. The copper is preferentially layered on the steel about the impact axis. By 8 μs, the debris cloud is nearly completely formed. At the final computed time of 11.64 μs, which corresponds to the time of the radiograph, the debris cloud has completely separated from the rear of the steel target, with a copper layer that has remained contiguous over a substantial section of the inside of the debris. The target hole still has the appearance of a normal impact, but the debris cloud is asymmetric, with more material contained on the left than on the right of the cloud. This is more clearly seen in the edge view of the target at 11.64 μs (Figure 44) where all the material on one side of the symmetry

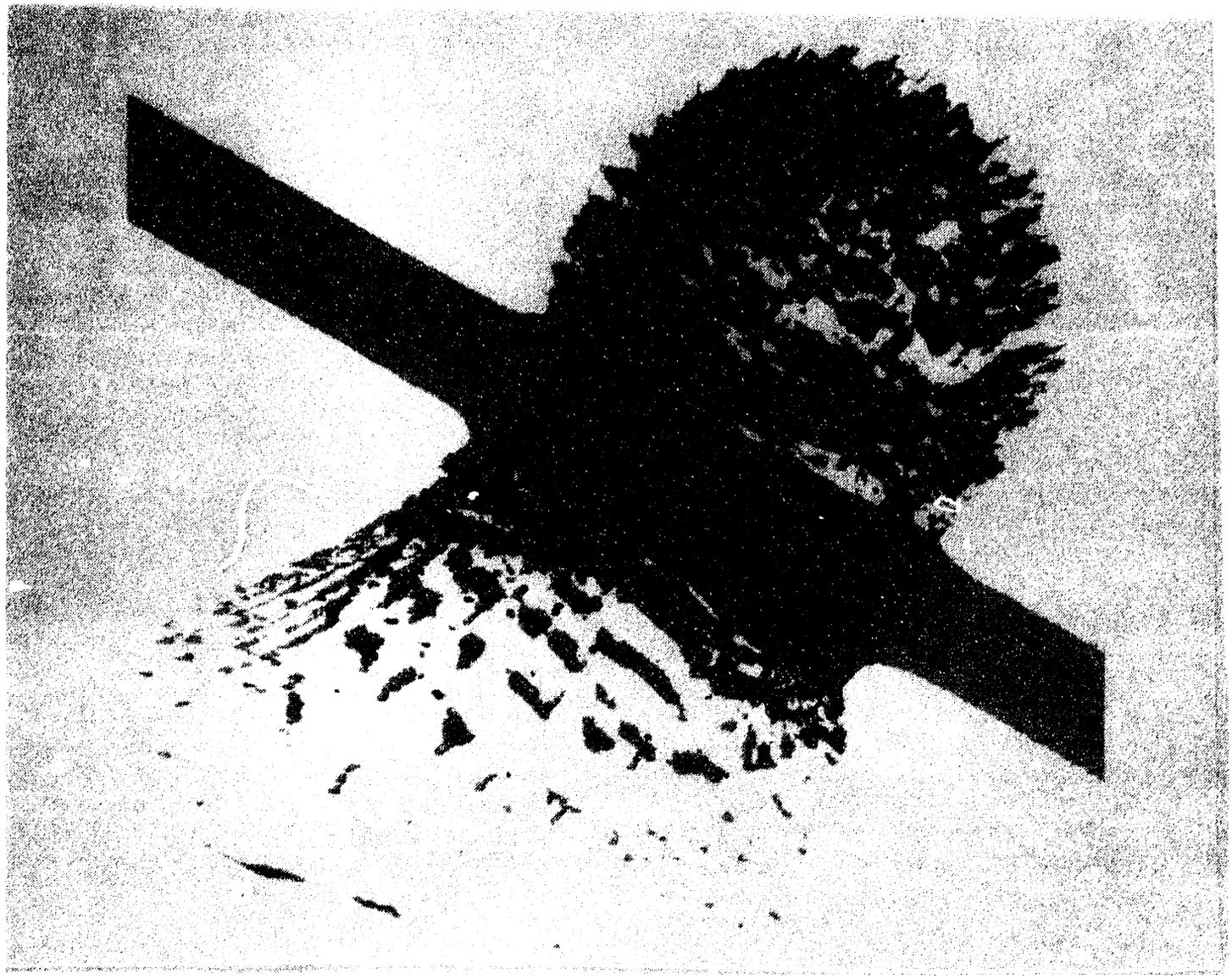

Figure 44. Edge view of the target at 11.64 μs (the darker material is copper).

plane has been removed revealing the interior of the crater and the bubble of debris ejecta. Much of the copper (the darker material) is continuing to thin and has not yet undergone instability breakup. On the other hand, all of the ejecta steel has fragmented by this time. The size and shape

of the fragments reflect in part the way the material is convected by the code, and the method of representing the data (half volume fractions). The fragment sizes were not computed in this instance. The cross-section (Figure 44) also shows the presence of spall rings formed at the front and rear of the target, as well as cracks penetrating the target. Hydrodynamic spreading of the copper occurs over the interior of the expanding steel debris shortly after impact and, late in time, interface separation between the steel and copper is achieved because of the difference in mechanical impedance. Artificial contributions to this separation may also come from the interface tracking algorithm in the code. Recent code modifications eliminate this material separation (Hertel, 1992).

Another representation of the oblique copper-on-steel impact calculation was provided by constructing a projected density normal to the symmetry plane at the final computational time of 11.6 μs. This simulated radiograph was then compared directly with the measured flash x-ray record at the corresponding time for the oblique impact experiment (Figure 45). The calculated profile of both the forward and backward ejected debris along with the mass density distribution throughout the debris cloud were in excellent agreement with the measured radiographic data. This nearly perfect overlay of the material boundaries indicates that the material motion in the impact has been properly computed. The presence of the larger mass of material at the top and left of the debris cloud is consistent with the densities of material observed in the radiograph (Figure 34).

The upward directed back-splash jet clearly observed in the x-ray image (Figure 34) is also prominent in the numerical simulation (Figure 44 and Figure 45). Although rapid instability particulation is observed, trajectories and velocities of about 7.5 km/s are consistent with the radiographic record. (Velocity of the observed leading jet fragments in Figure 34 was about 6 km/s.) The jet is comprised of both copper and steel material.

A final view of the impact event at 11.6 μs is a stereo (cross-eye) perspective provided by the pair of images in Figure 46. Note that the debris bubble is indeed hollow, and that there is copper mixed with steel in the impact-surface ejecta.

Due to entropy production in the primary shockwave in the copper projectile, substantial temperature increases occur. The calculated residual temperatures in the copper (at 11.6 μs) are below incipient melt (~1356 K) for nearly all of the mass (Figure 47). Approximately 0.16 g (13%) of the copper remains in the melted state. Only traces of the steel are calculated to remain melted.

At approximately 5 μs into the calculation, breakup of the behind target ejecta initiates (*cf.* Figure 43). Breakup is not a consequence of the tensile fracture model. Rather, it is thought to be a result of kinematic instabilities in the rapidly thinning shell of ejecta probably stimulated by numerical perturbations. Fragmentation of the copper occurs later in time than the steel, consistent with the expected effect of the substantially lower plastic flow stress of the copper on instability breakup. The trend of material to align on 45 degree planes is a consequence of preferential material convection in the interface tracking algorithm.

Fractures which initiated at later times (Figure 43) in the plane of the 4340 steel target plate, on the other hand, are a consequence of stress states exceeding the tensile fracture criterion. These fractures are consistent in trend with the fractures observed in sectioned target plates used in the

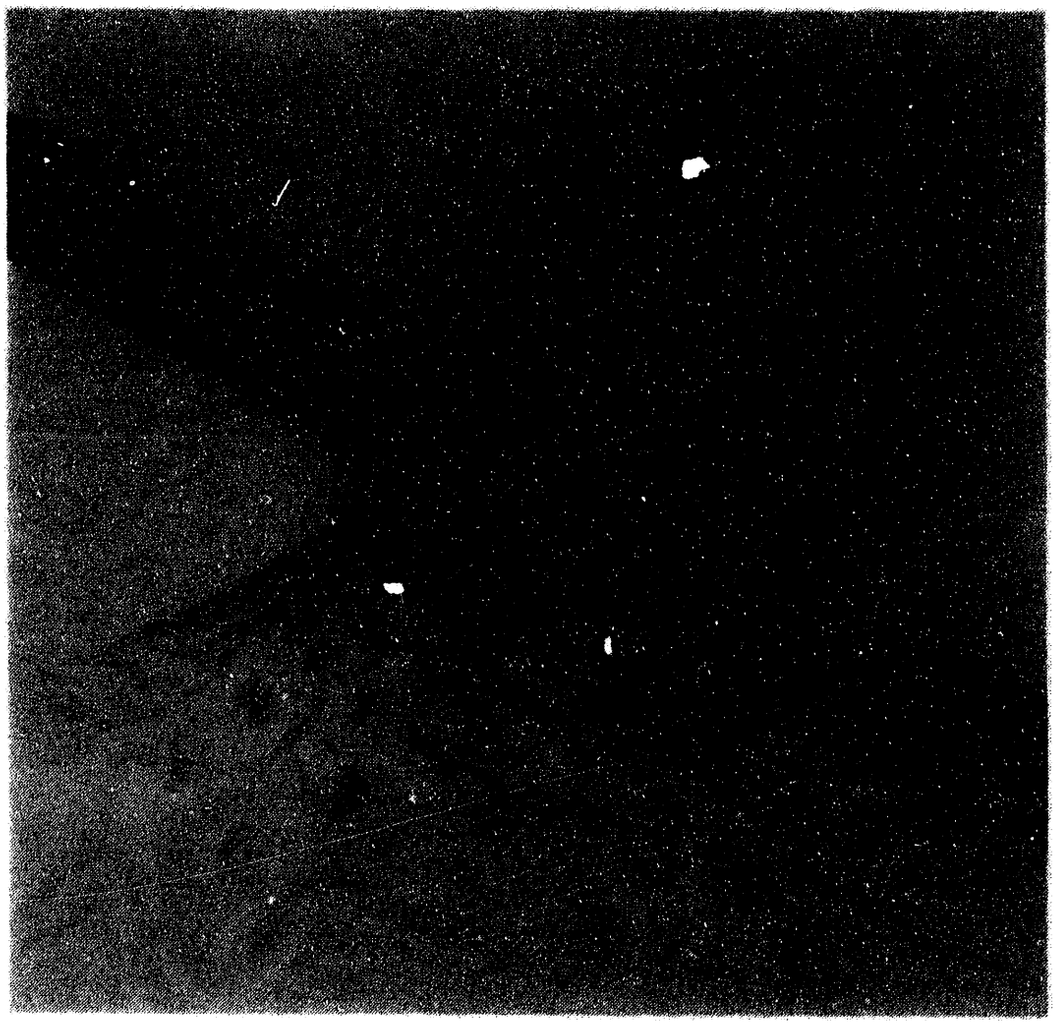

Figure 45. Simulated radiograph from the calculation, at 11.6 μs.

Figure 46. Stereo perspective of the oblique impact at 11.6 μs.

IV. CONCLUSIONS

The experiments and calculations reported here provide insight into the nature of debris formed during impact and penetration of a target.

The experiments with PMMA targets provide a clear definition of the steel debris cloud formed by the impact of a steel sphere. The spectrum of impact velocities and target thicknesses provide sufficient basis to establish trends in debris cloud formation. Some aspects of the fragmenting steel sphere data are represented quite well by the calculations, particularly the axial velocity decrease and the radially divergent velocity imparted to the sphere. The former property, the axial velocity decrease, is primarily a function of the hydrodynamics of impact; the radial velocity acquired by the particles of the sphere is more sensitive to the modeling of the fracture, particularly the time at which the material separates. The ability to calculate detailed fragment size distributions is the first step in defining quantitative properties of debris clouds for subsequent interactions. The quantitative comparisons of debris characterization will require some additional refinement of the data from the radiographs. The simulations have also demonstrated that there is additional work required on the fracture model used here to more precisely determine the time of fracture and the condition of the steel at breakup.

High-resolution radiographic images of ejecta motion and fragmentation caused by impact of copper spheres on steel plates at 3 to 5 km/s are a principle result of the present study. The images were obtained at times after impact which are amenable to, and for the purpose of, verification of computational simulation of the impact event. Simulations with the 3-D Eulerian hydrocode CTH were in good agreement with all major features of the radiographic data. The study uncovered minor numerical difficulties for which improvements were implemented over the course of the research.

The remarkably good agreement in the size and character of material breakup in the computational simulation with radiographic data remains incompletely understood. A reasonable understanding of the plastic instability breakup mechanisms of expanding debris bubbles and stretching jets is beginning to emerge (e.g. Grady, 1987; Romero, 1989). Whether instability breakup of material in the computational simulation captures a measure of the correct physical instability mechanisms, or is strictly a numerical instability issue, remains to be worked out.

Passive fragmentation diagnostics were successfully implemented in the present experimental study in terms of witness foils and low-density foam fragment capture devices. Interrogation with static radiography and image processing methods provided statistical size, number density and trajectory data. Implementation of energy-based fragmentation models within the 3-D CTH hydrocode has provided a tool for the analysis of debris breakup in the hypervelocity impact event (Kipp, *et al.*, 1993).

The extrapolation of the debris characterization to subsequent targets is a step that requires additional technique development.

This report provides experimental and analytic research in support of the 1990-1992 Laboratory Directed Research and Development program on behind armor debris. The effort was

focused on providing an experimental foundation and an understanding of material response in dynamic fragmentation for the purpose of the validation and expansion of computational fragmentation modelling and calculation. Tasks remaining which would enhance our understanding of the debris formed in these impact events include:

1. Image processing of fragmentation radiographs to extract statistical fragment size data,
2. Measure spall crater profiles on representative primary target impact plates,
3. Completion of several tests in which recovery of the fragment debris will be accomplished and statistical size analysis performed on the recovered data.

V. REFERENCES

Ang, J. A. (1992). Sandia National Laboratories, Personal communication.

Backman, M. E. and W. Goldsmith (1978). The Mechanics of Penetration of Projectiles and Targets. *Int. J. Engng. Sci.*, 16, 1-99.

Backman, M. E. and S. A. Finnegan (1984). A Phenomenological Investigation of the Impact of Compact Projectiles Against Plates at Speeds up to 3 km/s. Proceedings of Eighth International Symposium on Ballistics, October 23-25, 1984, Orlando.

Bertholf, L. D., L. D. Buxton, B. J. Thorne, R. K. Byers, A. L. Stevens, and S. L. Thompson (1975). Damage in Steel Plates from Hypervelocity Impact. II. Numerical Results and Spall Measurement, *J. Appl. Phys.*, 46, 3776-3782.

Brown, W. K. (1989). *J. Astrophys. Astr.*, 10, 89-112.

Chhabildas, L. C., E. Hertel, and S. Hill (1993). Hypervelocity Impact Tests and Simulations of Single Whipple Bumper Shield Concepts at 10km/s. *Int. J. Impact Engng.*, (in press).

Cour-Palais, B. G. (1987). Hypervelocity Impact in Metals, Glass, and Composites. *Int. J. Impact Engng.*, 5, 221-237.

Englman, R., Z. Jaeger, and A. Levi (1984). Percolation Theoretical Treatment of Two-Dimensional Fragmentation in Solids. *Phil. Mag. B*, 50, 307-315.

Glenn, L. A. and A. Chudnovsky (1986). Strain Energy Effects on Dynamic Fragmentation. *J. Appl. Phys.*, 59, 1379-1380.

Grady, D. E. (1982). Local Inertia Effects in Dynamic Fragmentation. *J. Appl. Phys.*, 53, 322-325.

Grady, D. E. (1987). Fragmentation of Rapidly Expanding Jets and Sheets. *Int. J. Impact Engng.*, 5, 285-292.

Grady, D. E. (1988). The Spall Strength of Condensed Matter. *J. Mech. Phys. Solids*, 36, 353-384.

Grady, D. E. (1990). Particle Size Statistics in Dynamic Fragmentation. *J. Appl. Phys.*, 68, 6099-6105.

Grady, D. E. and M. E. Kipp (1985). Geometric Statistics and Dynamic Fragmentation. *J. Appl. Phys.*, 58, 1210-1222.

Grady, D. E. and M. E. Kipp (1989). Fragmentation of Solids Under Dynamic Loading, *Structural Failure*, (ed. T. Wierzbicki & N. Jones), John Wiley & Sons, Inc.

Grady, D. E. and S. L. Passman (1990). Stability and Fragmentation of Ejecta in Hypervelocity Impact. *Int. J. Impact Engng.*, 10, 197-212.

Grady, D. E., J. E. Dunn, J. L. Wise, and S. L. Passman (1990a). Analysis of Prompt Fragmentation. Sandia National Laboratories Report, SAND90-2015.

Grady, D. E., J. W. Swegle, and J. A. Ang (1990b). Analysis of Prompt Fragmentation Oct 89-Sept. 90. SAND91-0483.

Herrmann, W. and J. S. Wilbeck (1987). Review of Hypervelocity Penetration Theories. *Int. J. Impact Engng.*, 5, 307-322.

Hertel, E. S. Jr. (1992). A Comparison of the CTH Hydrodynamics Code with Experimental Data. Sandia National Laboratories Report, SAND92-1879.

Hohler, V. and A. J. Stilp (1987). Hypervelocity Impact of Rod Projectiles with L/D from 1 to 32. *Int. J. Impact Engng.*, 5, 323-331.

Johnson, W. A. and R. F. Mehl (1939). Reaction Kinetics in Processes of Nucleation and Growth. *Trans. A. I. M. M. E.*, 135, 416-458.

Johnson, G. R., R. A. Stryk, T. J. Holmquist, and O. A. Souka (1990). Recent EPIC Code Developments for High Velocity Impact: 3D Element Arrangements and 2D Fragment Distributions. *Int. J. Impact Engng.*, 10, 281-294.

Kipp, M. E. and D. E. Grady (1985). Dynamic Fracture Growth and Interaction in One Dimension. *J. Mech. Phys. Solids*, 33, 399-415.

Kipp, M. E., D. E. Grady, and J. W. Swegle (1993). Numerical and Experimental Studies of High-Velocity Impact Fragmentation. *Int. J. Impact Engng.*, (in press).

Lawrence, R. J. (1992). A Simple Approach for the Design and Optimization of Stand-off Hypervelocity Particle Shields. AIAA Space Programs and Technologies Conference, Paper AIAA 92-1465, March 24-27, 1992, Huntsville, AL.

McGlaun, J. M., S. L. Thompson, and M. G. Elrick (1990). CTH: A Three-Dimensional Shock Wave Physics Code. *Int. J. Impact Engng.*, 10, 351-360.

Melosh, H. J., E. V. Ryan, and E. Asphaug (1992). Dynamic Fragmentation in Impacts: Hydrocode Simulation of Laboratory Impacts. *J. Geophys. Res. - Planets*, 97, No. E9.

Piekutowski, A. J. (1992). Properties of Largest Fragment Produced by Hypervelocity Impact of Aluminum Spheres with Thin Aluminum Sheets, AIAA 92-1588, AIAA Space Programs and Technologies Conference, March 24-27, 1992, Huntsville, Alabama.

Romero, L. (1989). The Instability of Rapidly Stretching Jets. *J. Appl. Phys.*, 65, 3006-3016.

Schuler, K. W. and J. W. Nunziato (1974). The Dynamic Mechanical Behavior of Polymethyl Methacrylate. *Rheol. Acta* 13, 265-273.

Smith, V. (1989). Kaman Sciences Corporation, Personal communication.

Trucano, T. G. and D. E. Grady (1985). Study of Intermediate Velocity Penetration of Steel Spheres into Deep Aluminum Targets. Sandia National Laboratories Report SAND82-2338, March 1985.

APPENDIX A - Debris Cloud Data (Steel Impacts onto PMMA Targets)

The data extracted from the radiographs which was deemed useful for purposes of validating analytic modelling or computational simulation of the impact fragmentation events are included in the present appendix. Appropriate experimental data for the debris cloud position and timing for the tests are provided in Table A. In a number of the earlier tests only the distance between the position of the fragment cloud in the first and second radiograph, and the corresponding transit times were recorded. In later experiments (Test 17 to 24) the distance from the front of the PMMA plate to the positions of the fragment cloud in the first radiograph was also determined and is included in Table A. Positions are to the geometric center of the fragment cloud with the exceptions of Tests 19, 23, and 24 where distances are to the front of the cloud.

Table A: Radiograph Debris Cloud Position and Timing Measurement Data[a]

Test	V_i	d_p	x_1	Δx	Δt	Test	V_i	d_p	x_1	Δx	Δt
#	m/s	mm	mm	mm	μs	#	m/s	mm	mm	mm	μs
1	4460	3.28	—	—	—	13	4430	5.37	—	127	31.9
2	4460	3.28	—	—	—	14	4060	5.36	—	183	49.1
3	4450	1.74	—	—	—	15	3310	5.38	—	138	45.1
4	4700	1.74	—	155	34.1	16	4080	5.37	—	143	38.1
5	4570	3.38	—	143	33.2	17	4520	3.25	205	155	35.9
6	3460	3.28	—	141	43.1	18	4430	4.71	156	147	35.9
7	4160	3.44	—	149	38.0	19	4610	5.39	166[b]	151[b]	35.9
8	3950	1.49	—	141	37.0	20	4040	4.75	169	142	38.0
9	3460	1.51	—	148	45.1	21	3750	4.78	171	150	42.9
10	3410	0.63	—	151	45.1	22	4700	0.99	183	161	34.9
11	3920	0.64	—	143	37.1	23	4060	11.23	142[b]	124[b]	37.9
12	4470	0.69	—	140	32.0	24	4030	9.47	159[b]	144[b]	42.9

[a] x_1 = distance from front of PMMA plate to position of fragment cloud in the first radiograph. Δx = distance between fragment cloud in first and second radiograph. Δt = time between first and second radiograph.

[b] Measured to the front of the fragment cloud.

APPENDIX B - Radiographs (Steel Impacts onto PMMA Targets)

The radiographic data acquired in each of the impact fragmentation events are included in the present appendix. The original radiograph is the upper left image in the figure. Each radiograph has been image-processed, and the results from those operations are included also: the upper right image is the digitized radiograph; the lower left is the same image with the encompassing envelope; and the lower right is the digitized outline of the radiograph. A size scale is provided in each figure to define the dimensions of the fragment cloud. Note that for most of the experiments, both the early and late time radiographs are present, but have been scaled to approximately the same image size. The relevant fragment sizes and numbers determined from these radiographs have been tabulated in Table 3. The areas A_{reg}, A_{obs} used to compute average fragment sizes in this table are acquired from the lower left image in the following figures. The total encompassed region, shown in white, is A_{reg}. The dark region within this image is identified as A_{obs}.

The single exception is for Test 12, which is represented only with the radiographs. The impact resulted in a small spall cap that was ejected from the trailing end of the ball, and no image processing was done.

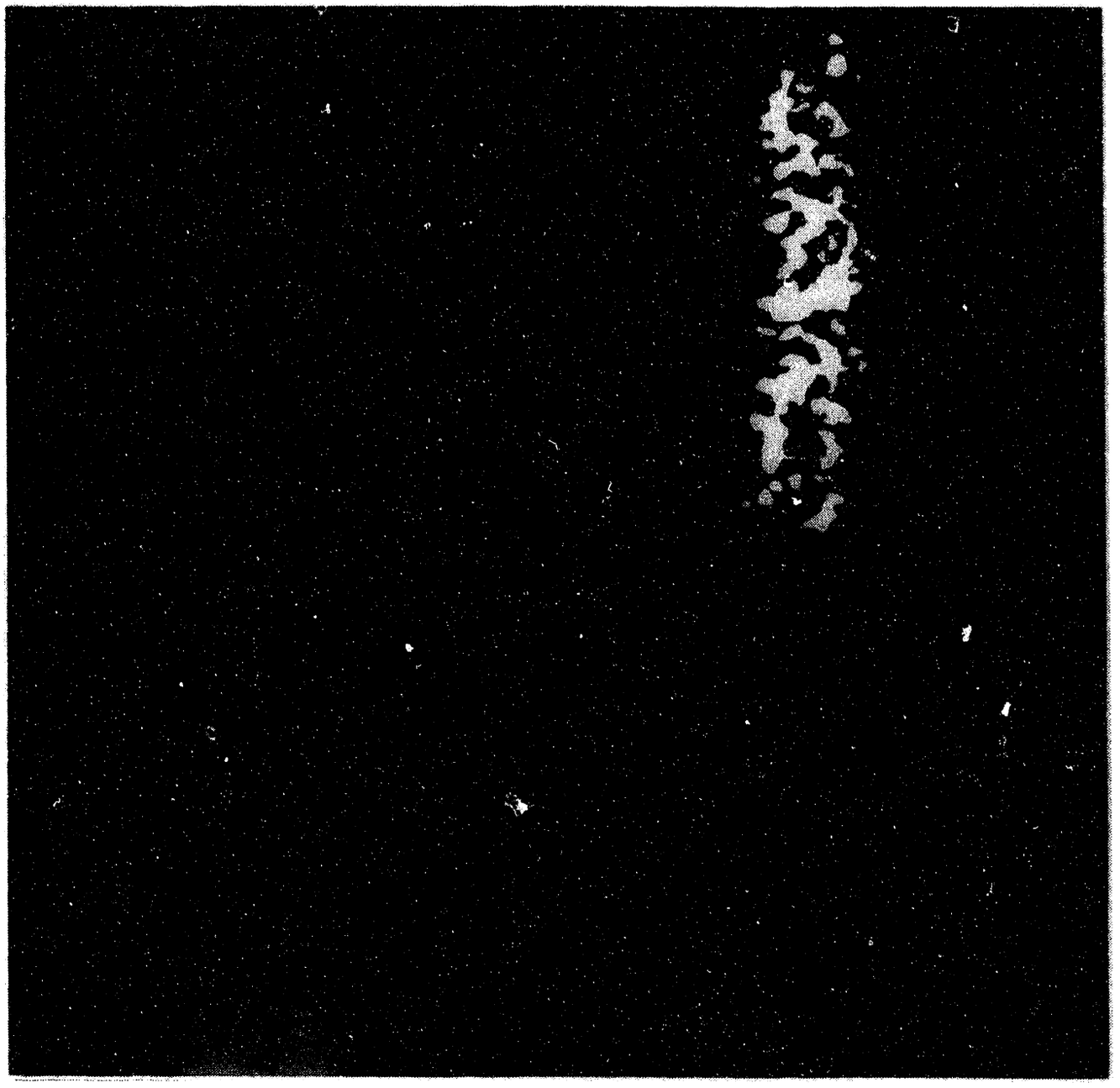

Test 1, Radiograph ~

20 mm

6.35 mm Steel Sphere Impact Velocity: 4460 m/s
PMMA Target Thickness: 3.28 mm

Figure B1. Test 1, Radiograph.

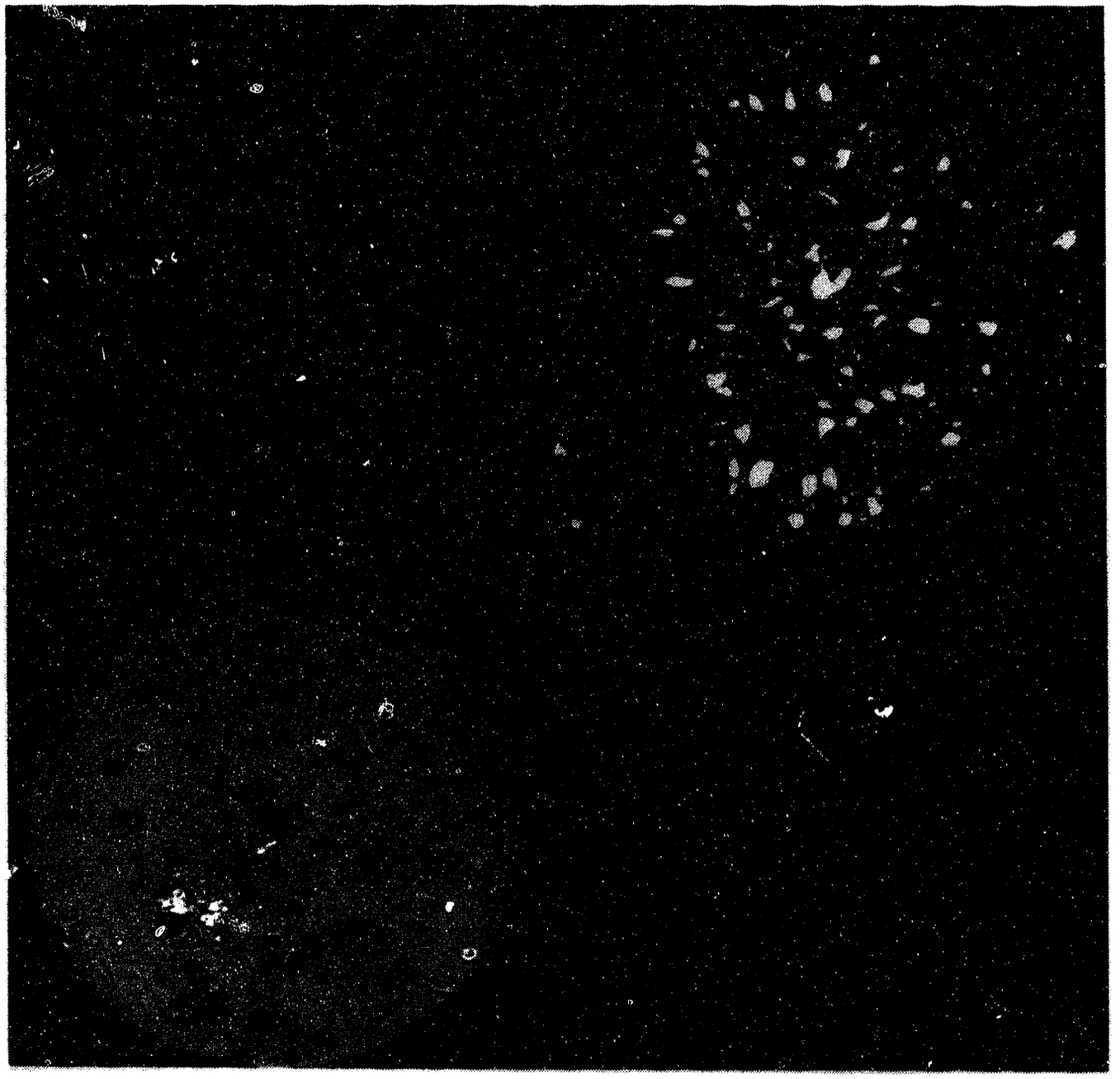

Test 2, Radiograph ~

20 mm

6.35 mm Steel Sphere Impact Velocity: 4450 m/s
PMMA Target Thickness: 3.28 mm

Figure B2. Test 2, Radiograph.

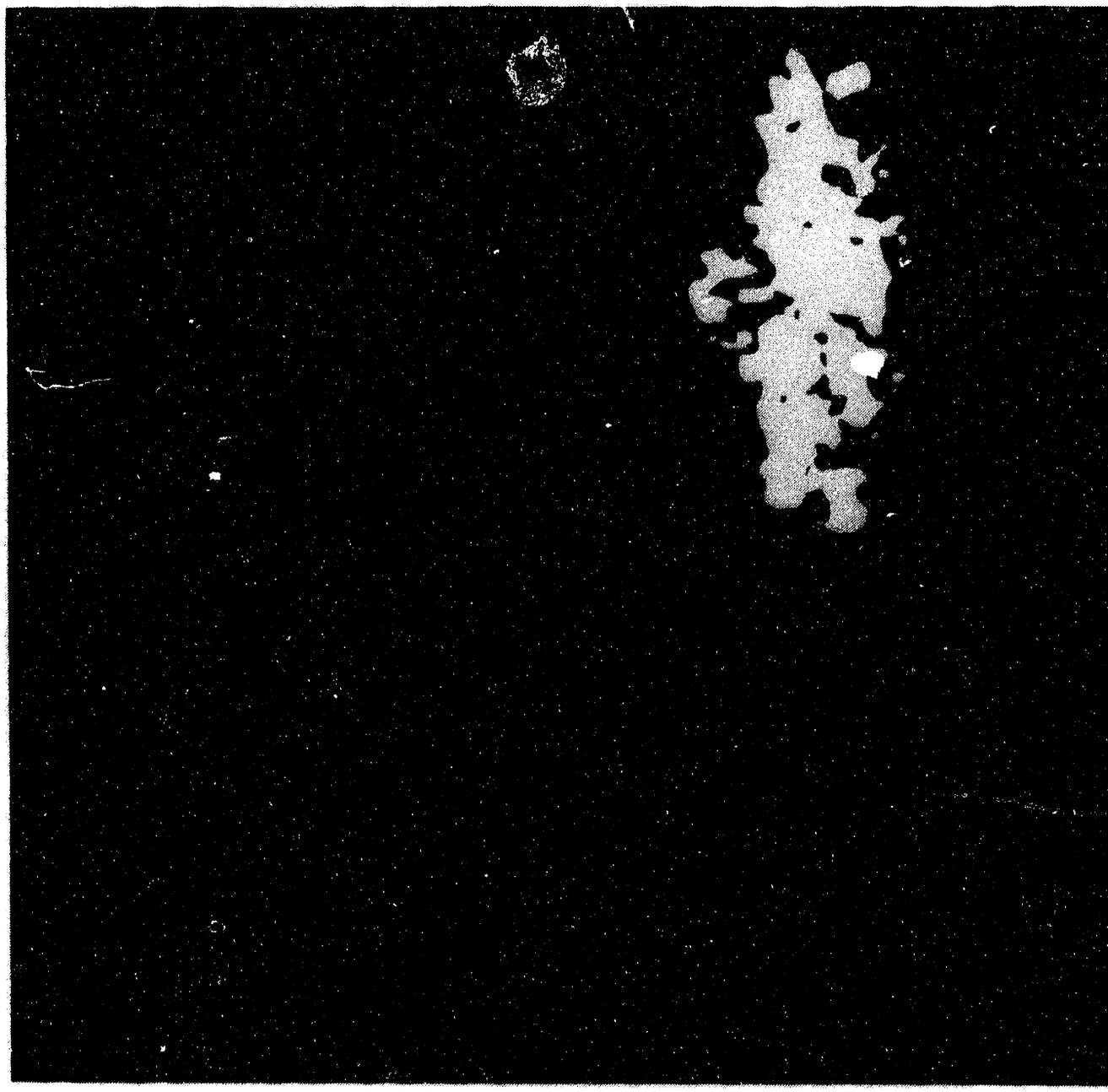

Test 3, Radiograph -

10 mm

6.35 mm Steel Sphere Impact Velocity: 4450 m/s
PMMA Target Thickness: 1.74 mm

Figure B3. Test 3, Radiograph.

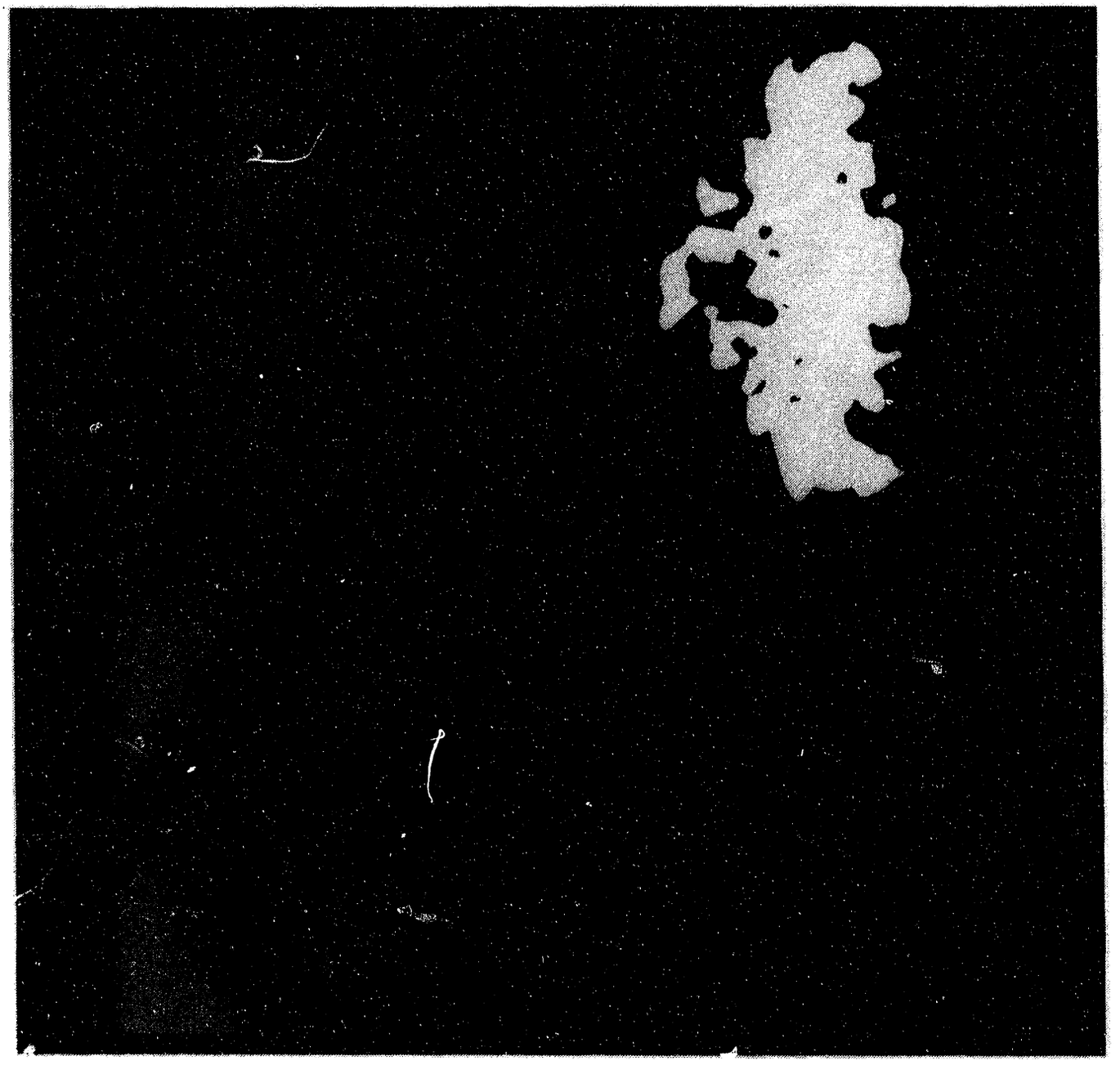

Test 4, Radiograph a ~

10 mm

6.35 mm Steel Sphere Impact Velocity: 4700 m/s
PMMA Target Thickness: 1.74 mm

Figure B4. Test 4, Radiograph a.

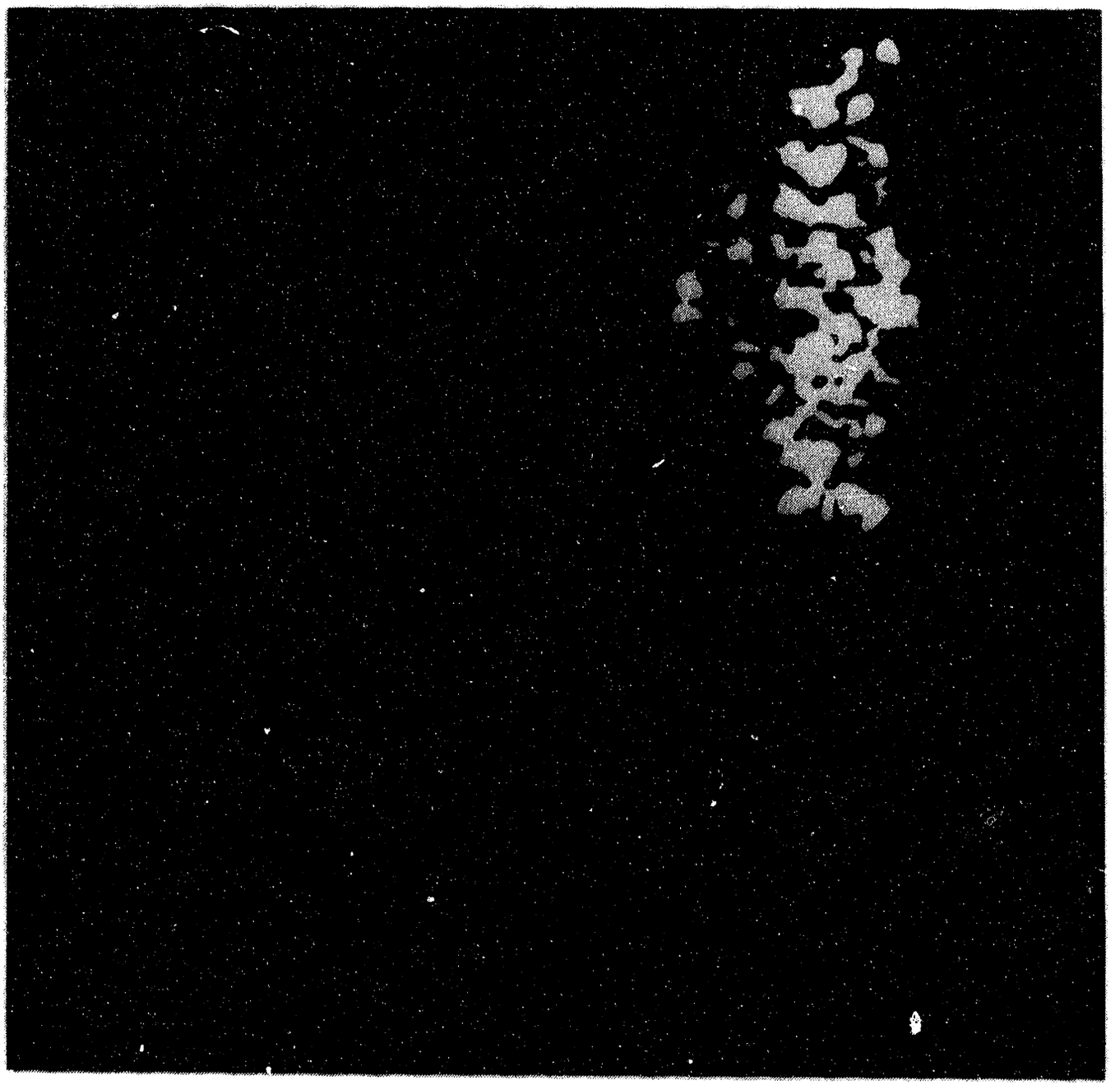

Test 4, Radiograph b ~

10 mm

6.35 mm Steel Sphere Impact Velocity: 4700 m/s
PMMA Target Thickness: 1.74 mm

Figure B5. Test 4, Radiograph b.

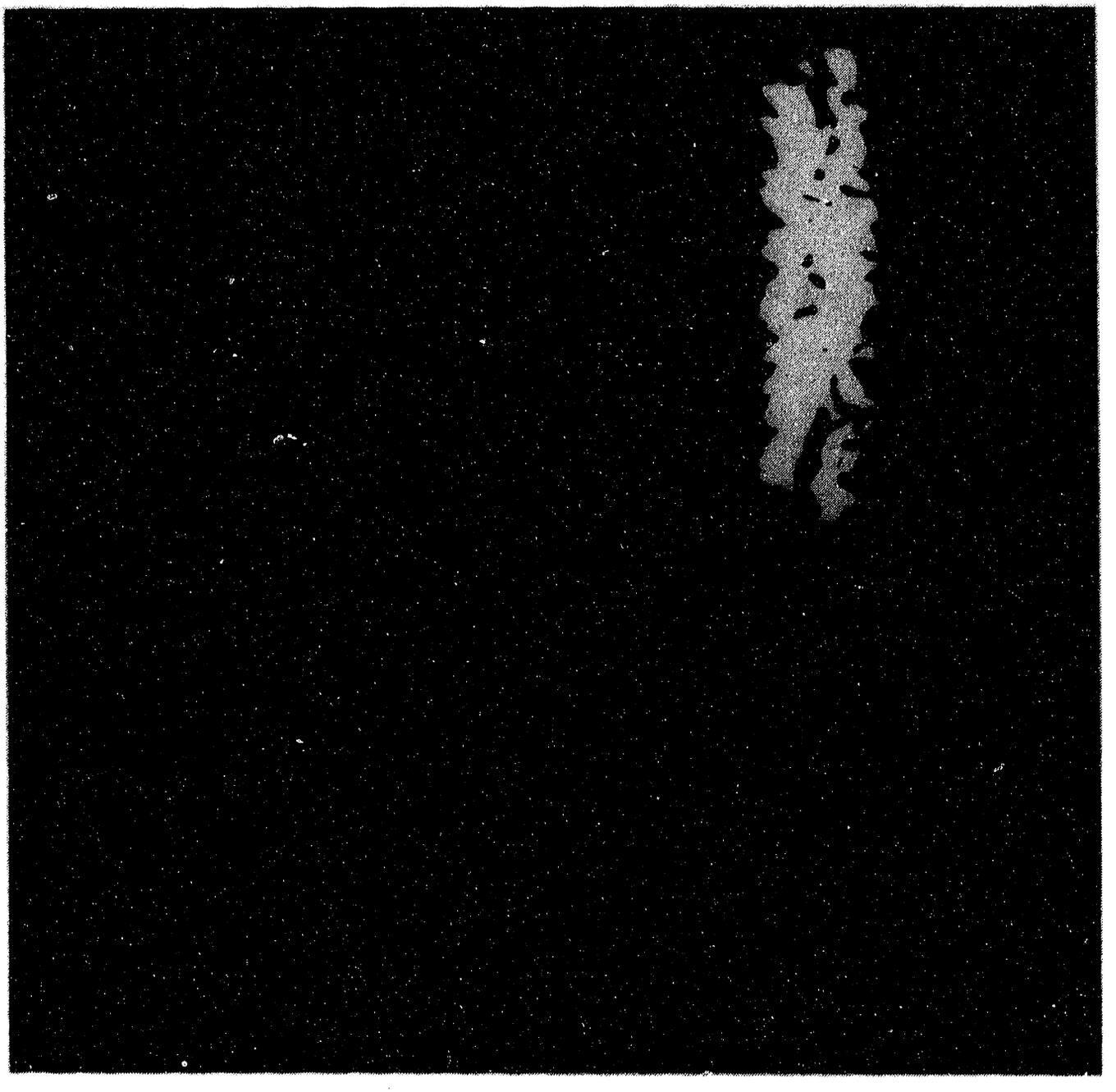

Test 5, Radiograph a ~

10 mm

6.35 mm Steel Sphere Impact Velocity: 4570 m/s
PMMA Target Thickness: 3.38 mm

Figure B6. Test 5, Radiograph a.

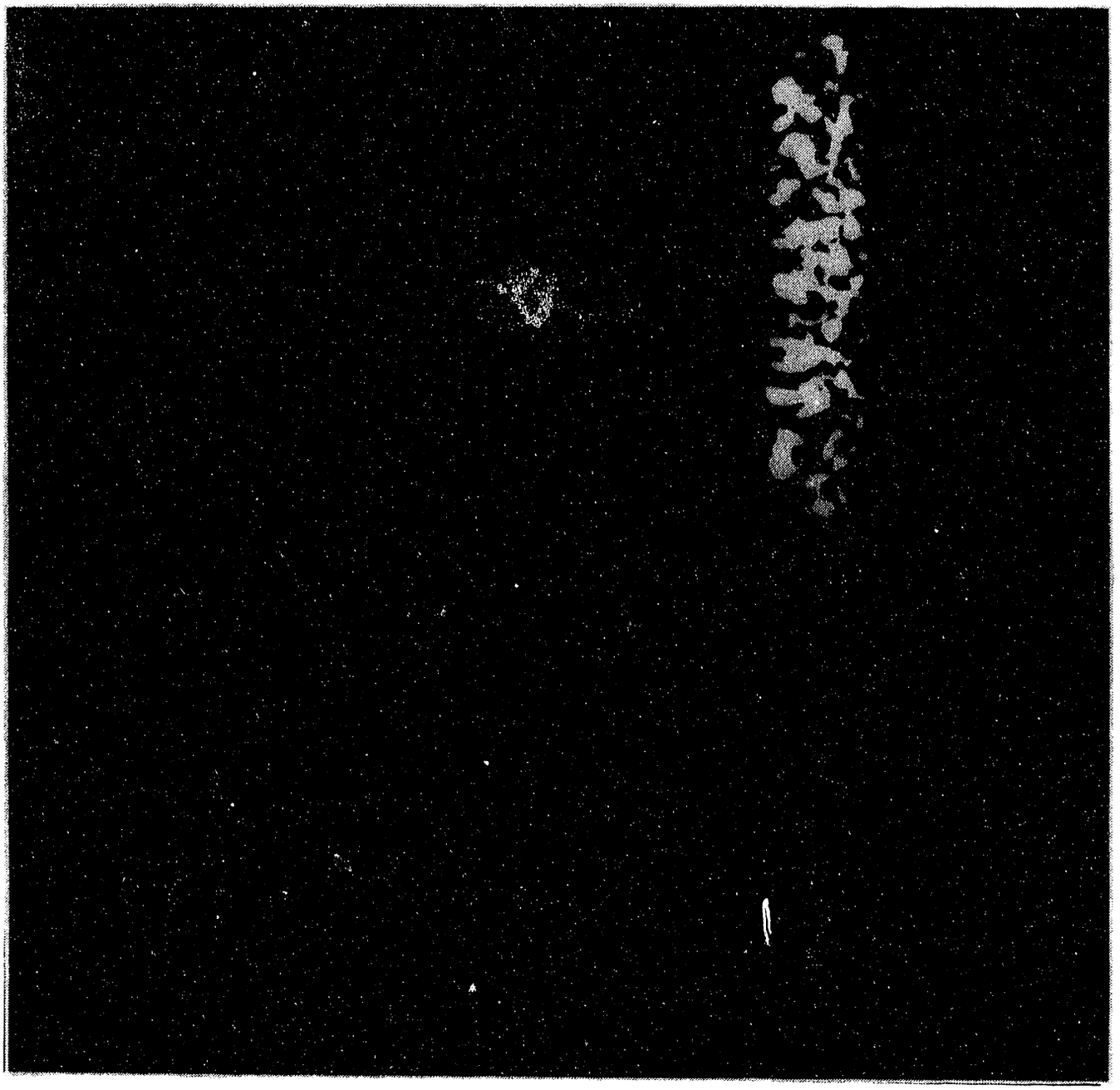

Test 5, Radiograph b ~

10 mm

6.35 mm Steel Sphere Impact Velocity: 4570 m/s
PMMA Target Thickness: 3.38 mm

Figure B7. Test 5, Radiograph b

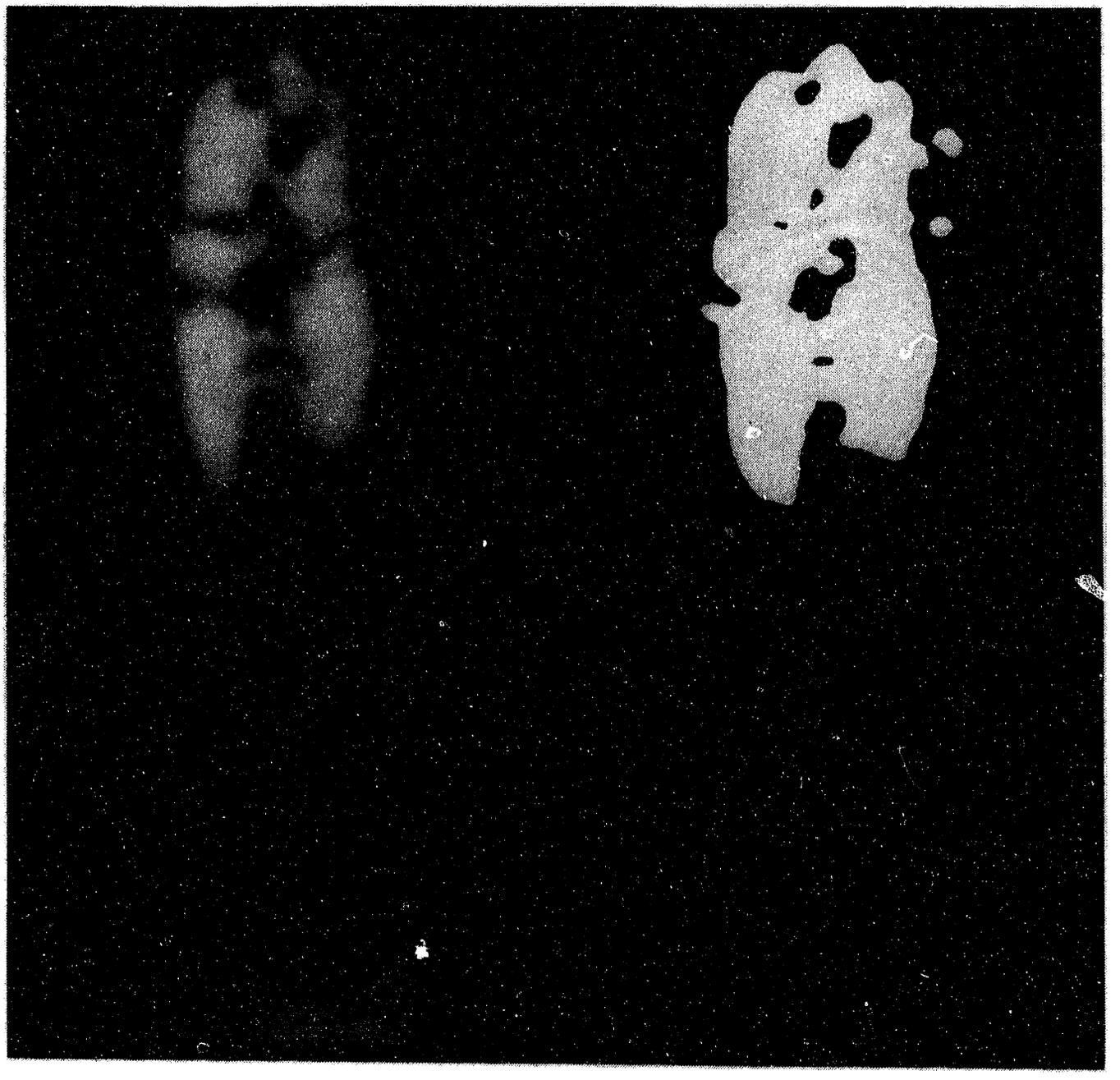

Test 6, Radiograph a ~

10 mm

6.35 mm Steel Sphere Impact Velocity: 3460 m/s
PMMA Target Thickness: 3.28 mm

Figure B8. Test 6, Radiograph a.

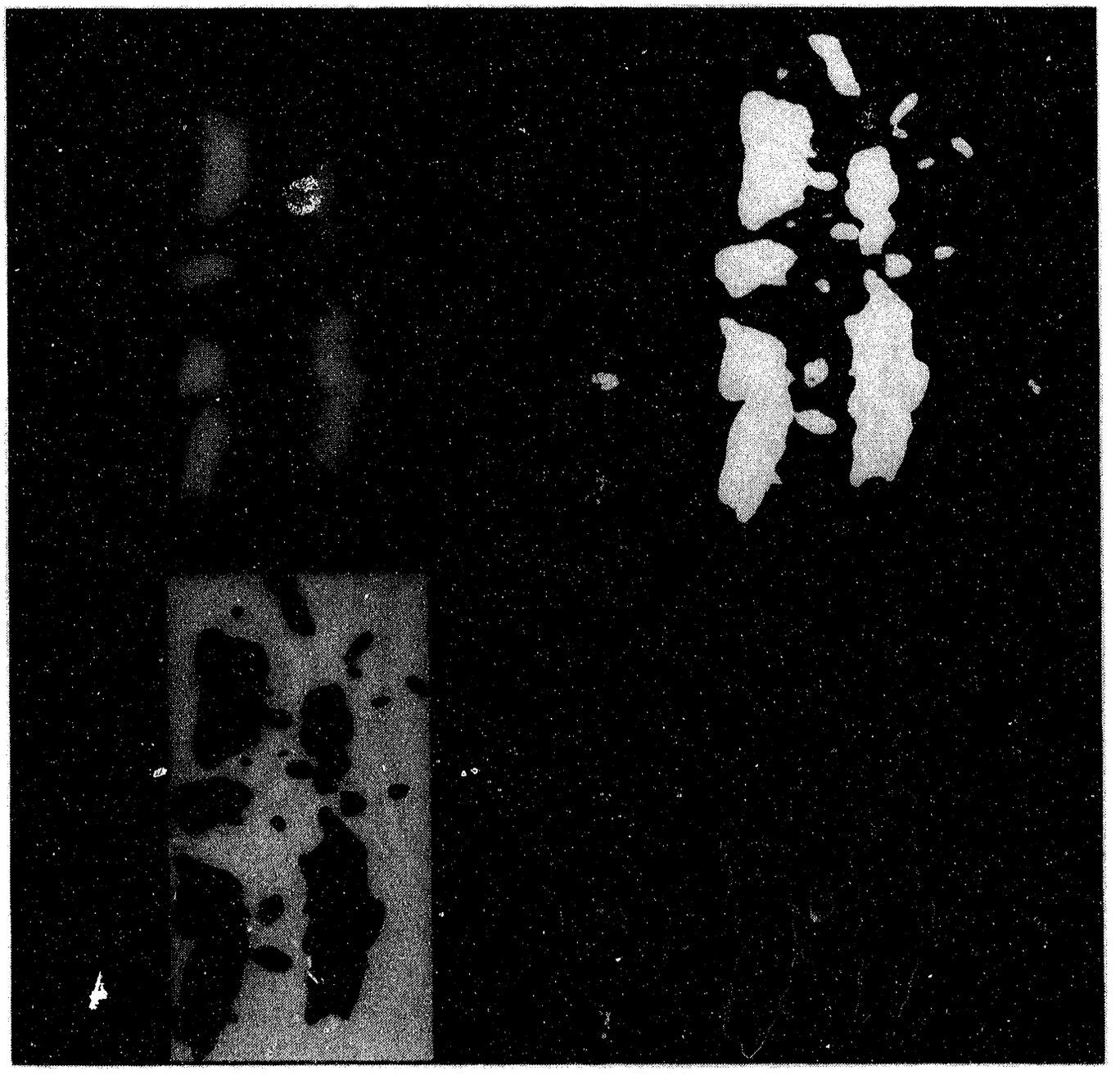

Test 6, Radiograph b ~

10 mm

6.35 mm Steel Sphere Impact Velocity: 3460 m/s
PMMA Target Thickness: 3.28 mm

Figure B9. Test 6, Radiograph b.

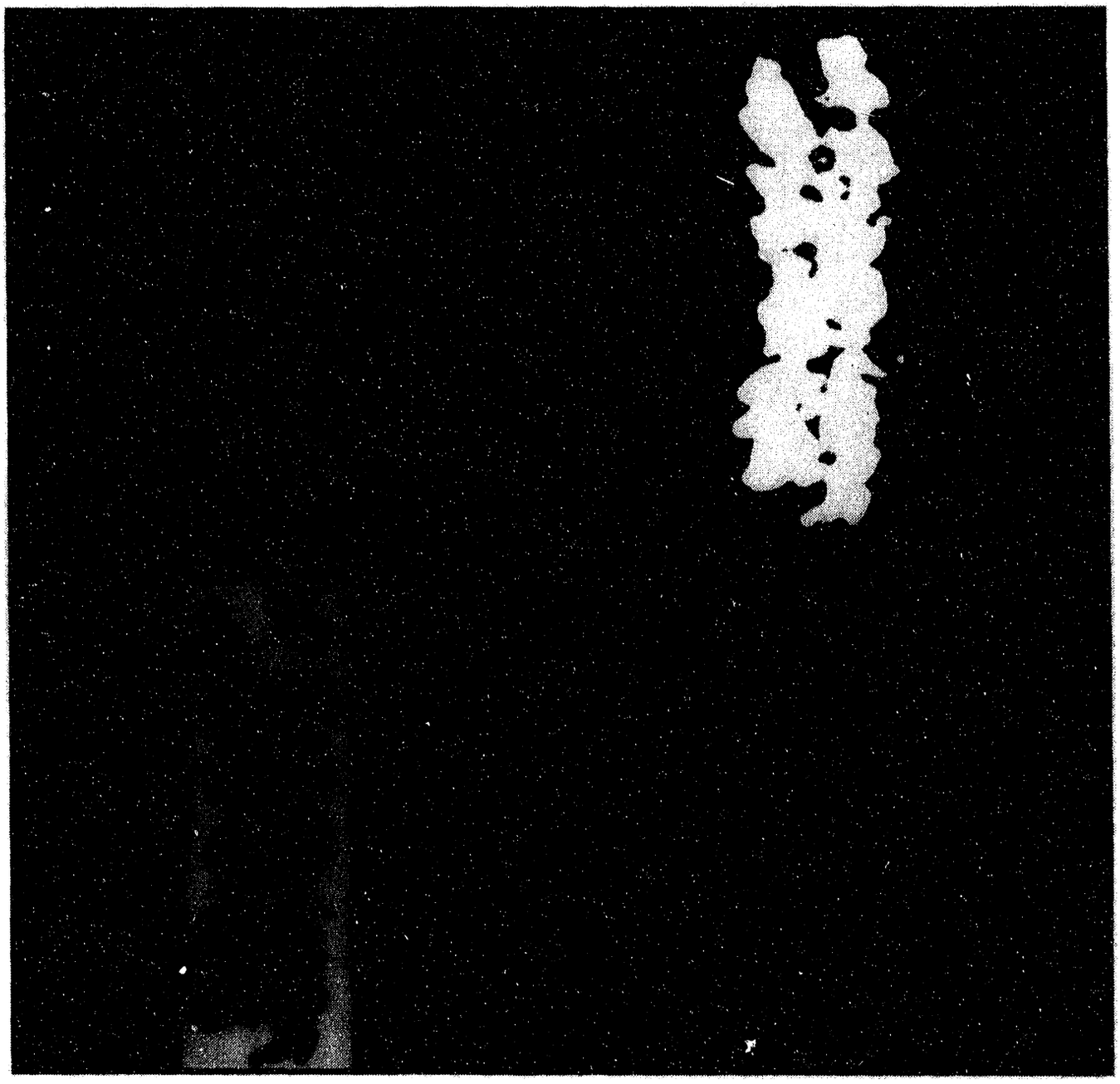

Test 7, Radiograph a ~

10 mm

6.35 mm Steel Sphere Impact Velocity: 4160 m/s
PMMA Target Thickness: 3.44 mm

Figure B10. Test 7, Radiograph a.

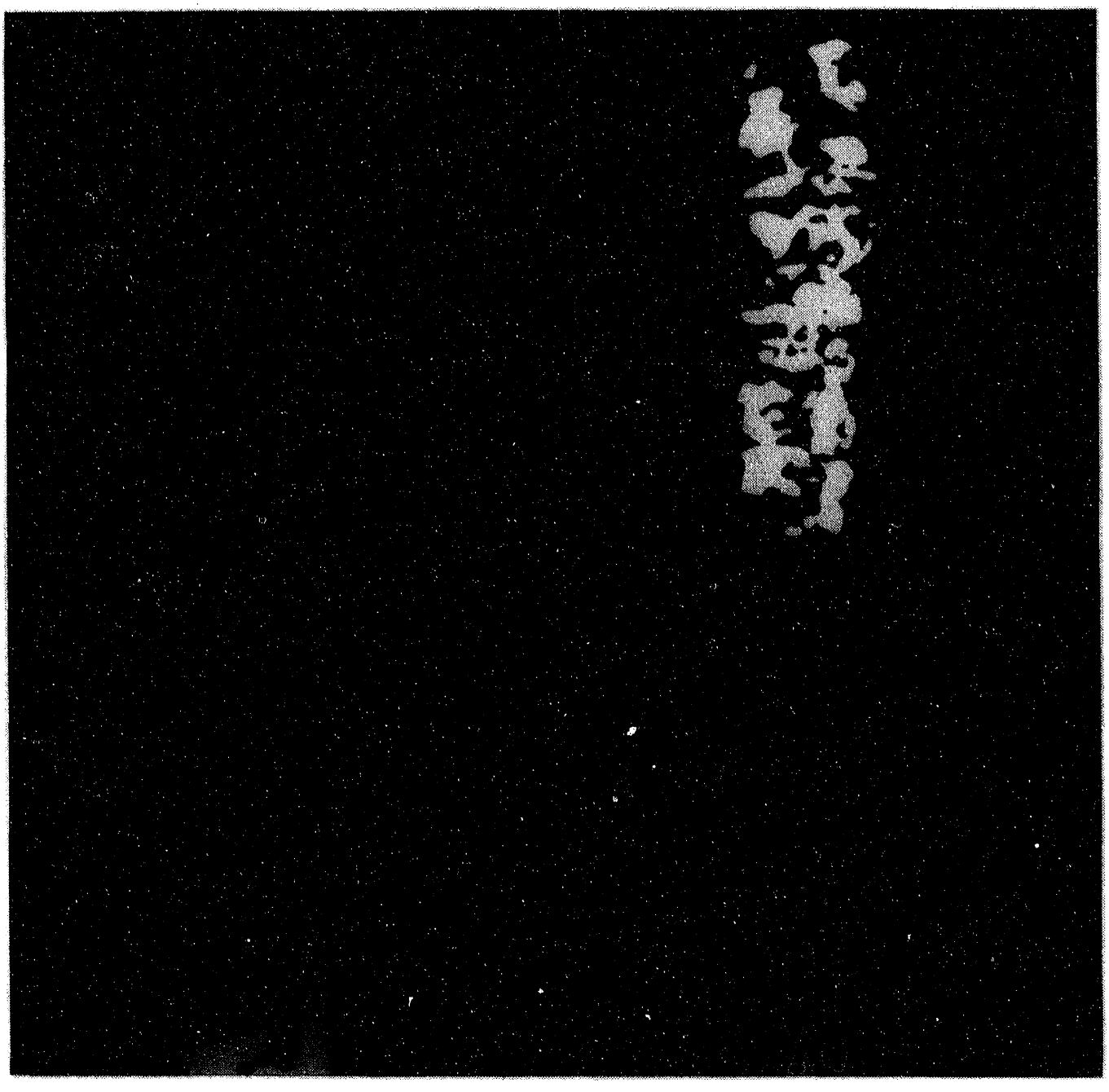

Test 7, Radiograph b ~

6.35 mm Steel Sphere Impact Velocity: 4160 m/s
PMMA Target Thickness: 3.44 mm

10 mm

Figure B11. Test 7, Radiograph b.

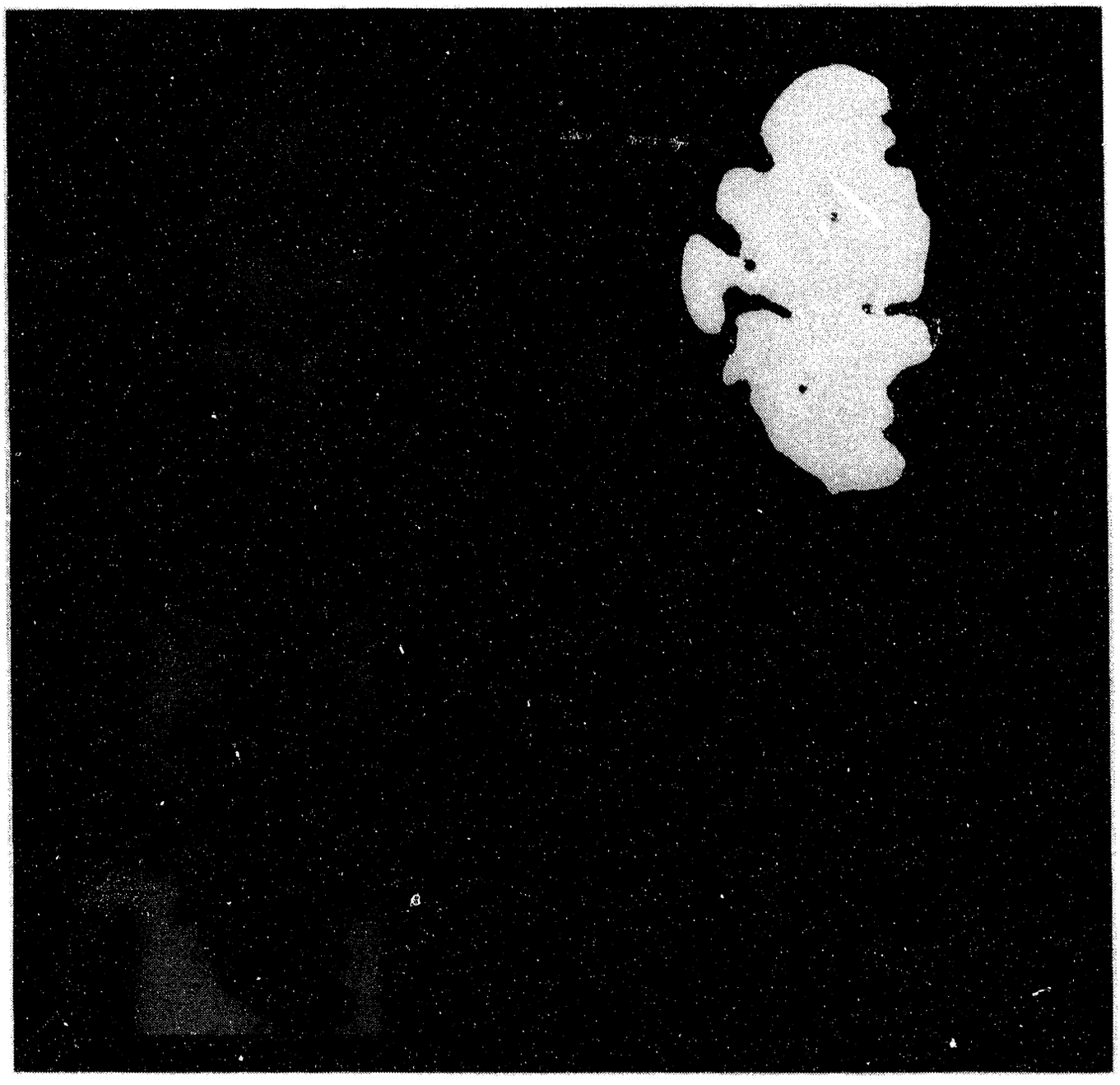

Test 8, Radiograph a ~

10 mm

6.35 mm Steel Sphere Impact Velocity: 3950 m/s
PMMA Target Thickness: 1.49 mm

Figure B12. Test 8, Radiograph a.

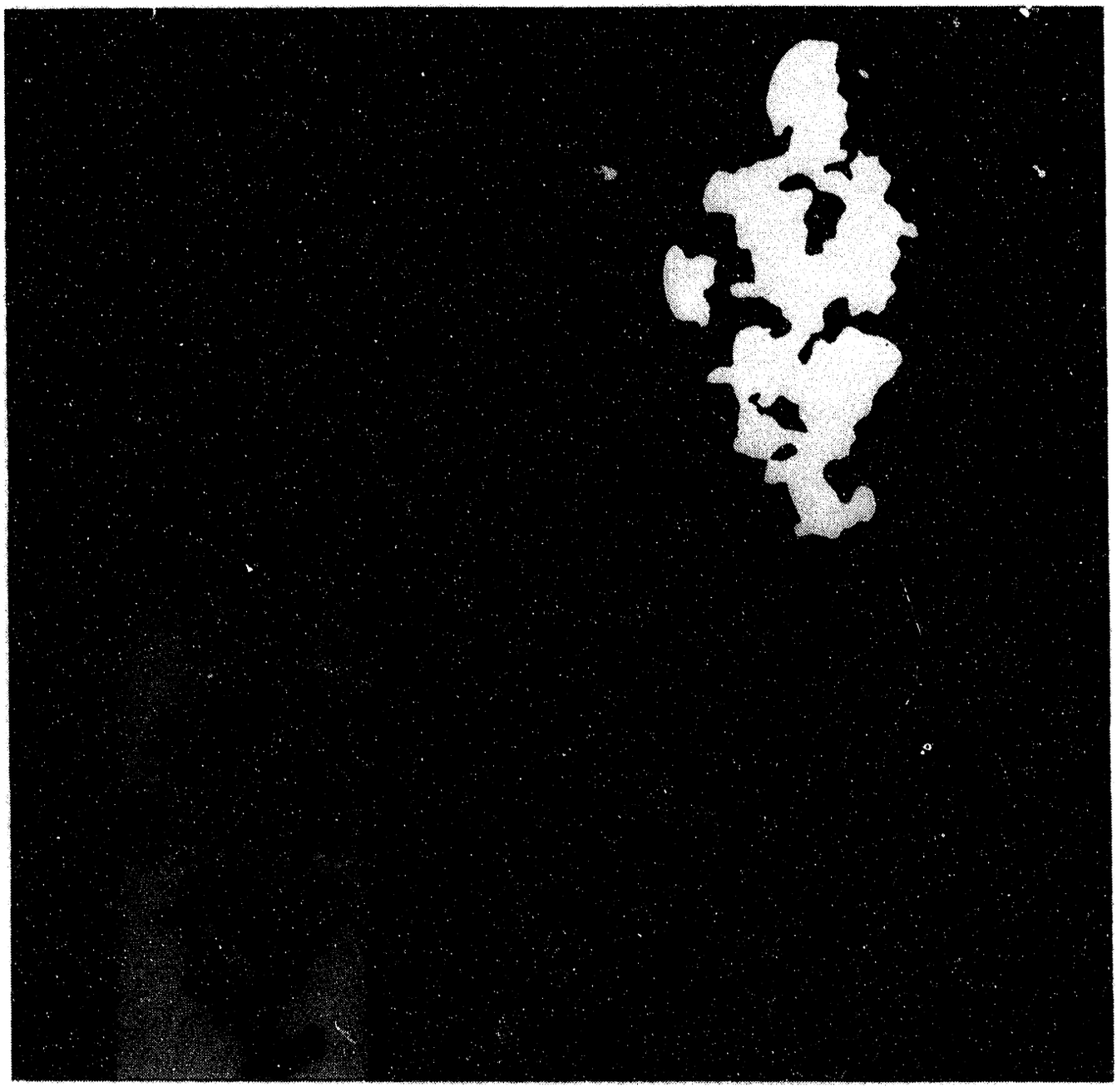

Test 8, Radiograph b ~

10 mm

6.35 mm Steel Sphere Impact Velocity: 3950 m/s
PMMA Target Thickness: 1.49 mm

Figure B13. Test 8, Radiograph b.

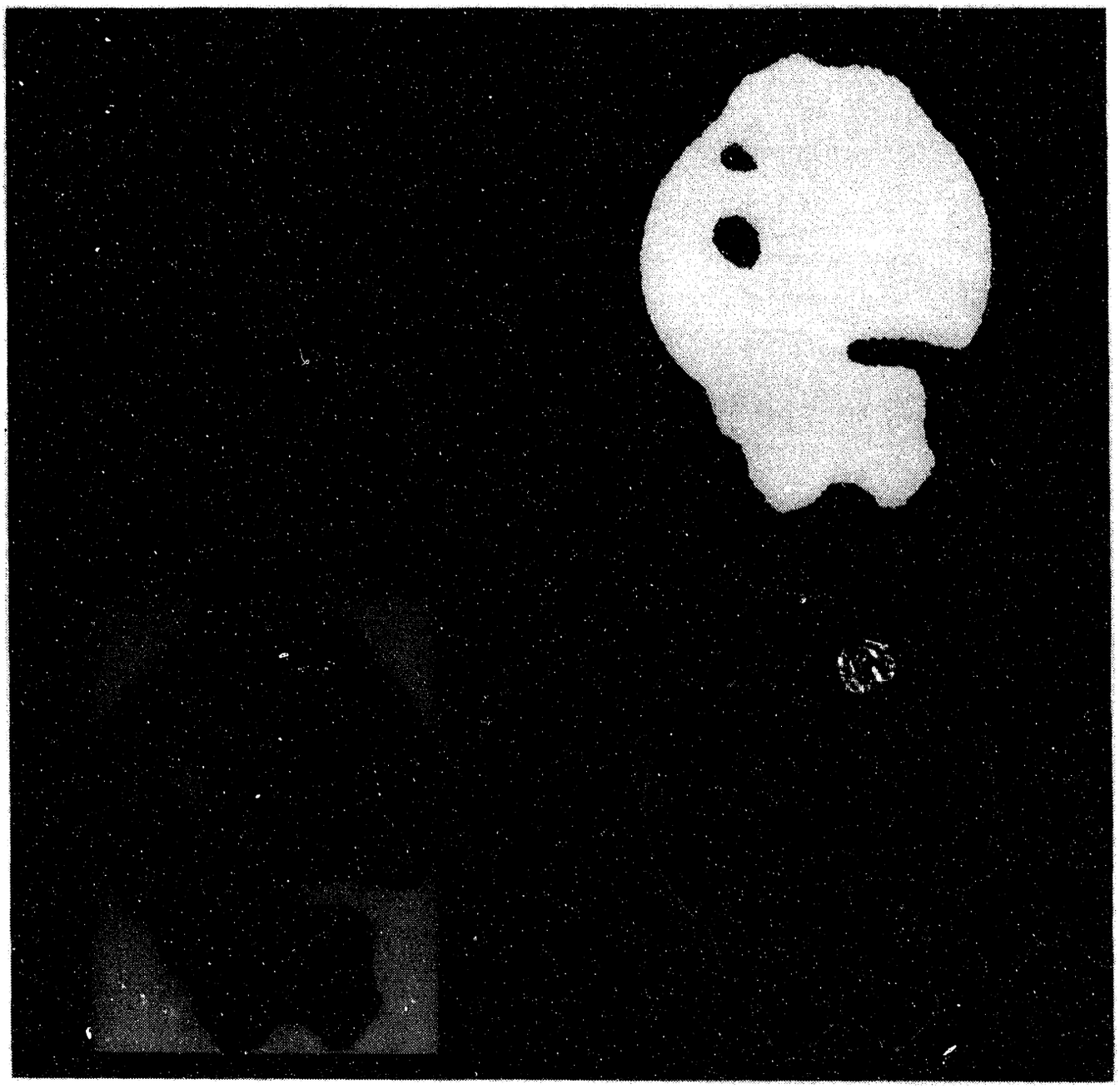

Test 9, Radiograph a ~

5 mm

6.35 mm Steel Sphere Impact Velocity: 3460 m/s
PMMA Target Thickness: 1.51 mm

Figure B14. Test 9, Radiograph a.

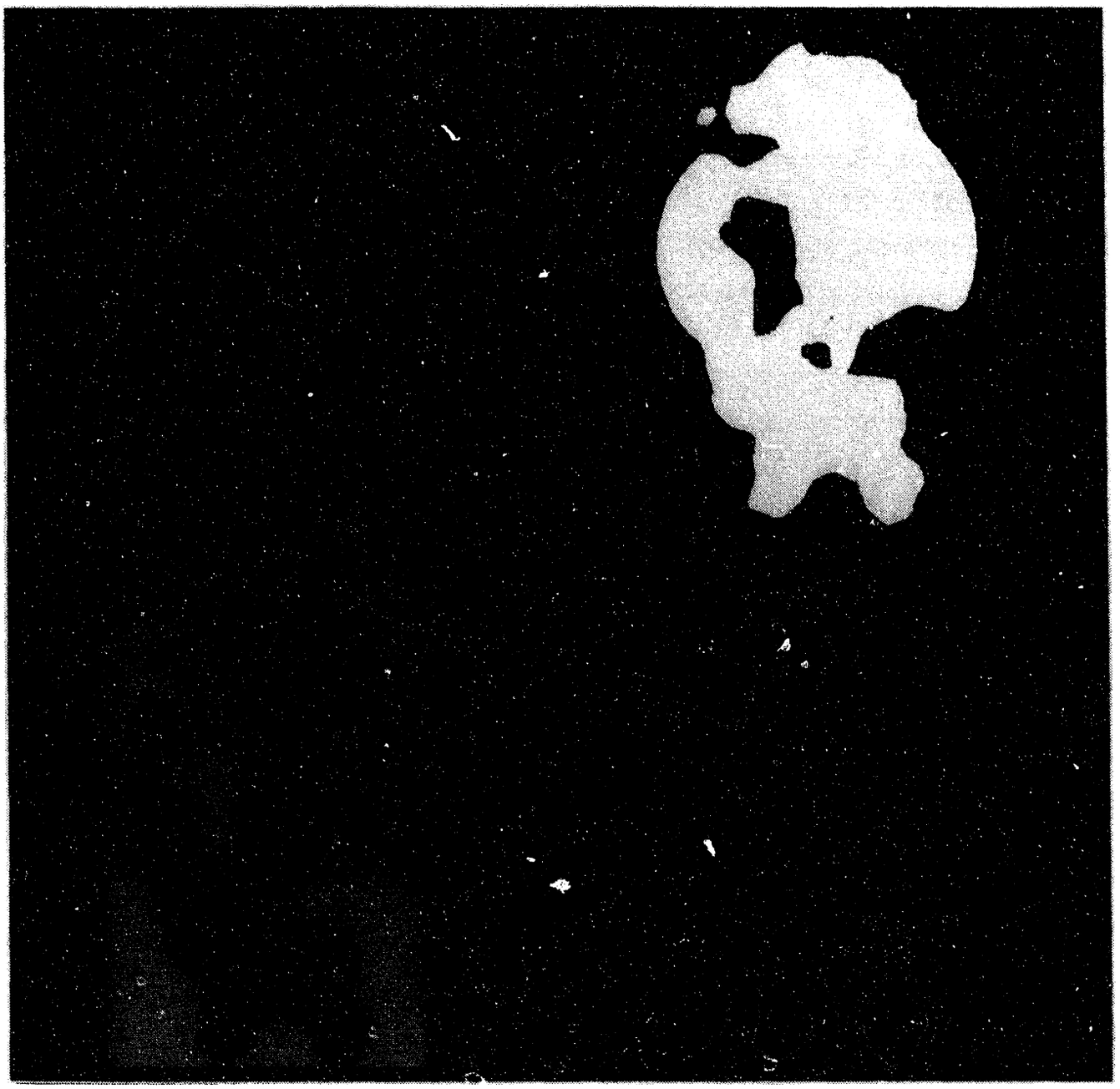

Test 9, Radiograph b ~

5 mm

6.35 mm Steel Sphere Impact Velocity: 3460 m/s
PMMA Target Thickness: 1.51 mm

Figure B15. Test 9, Radiograph b.

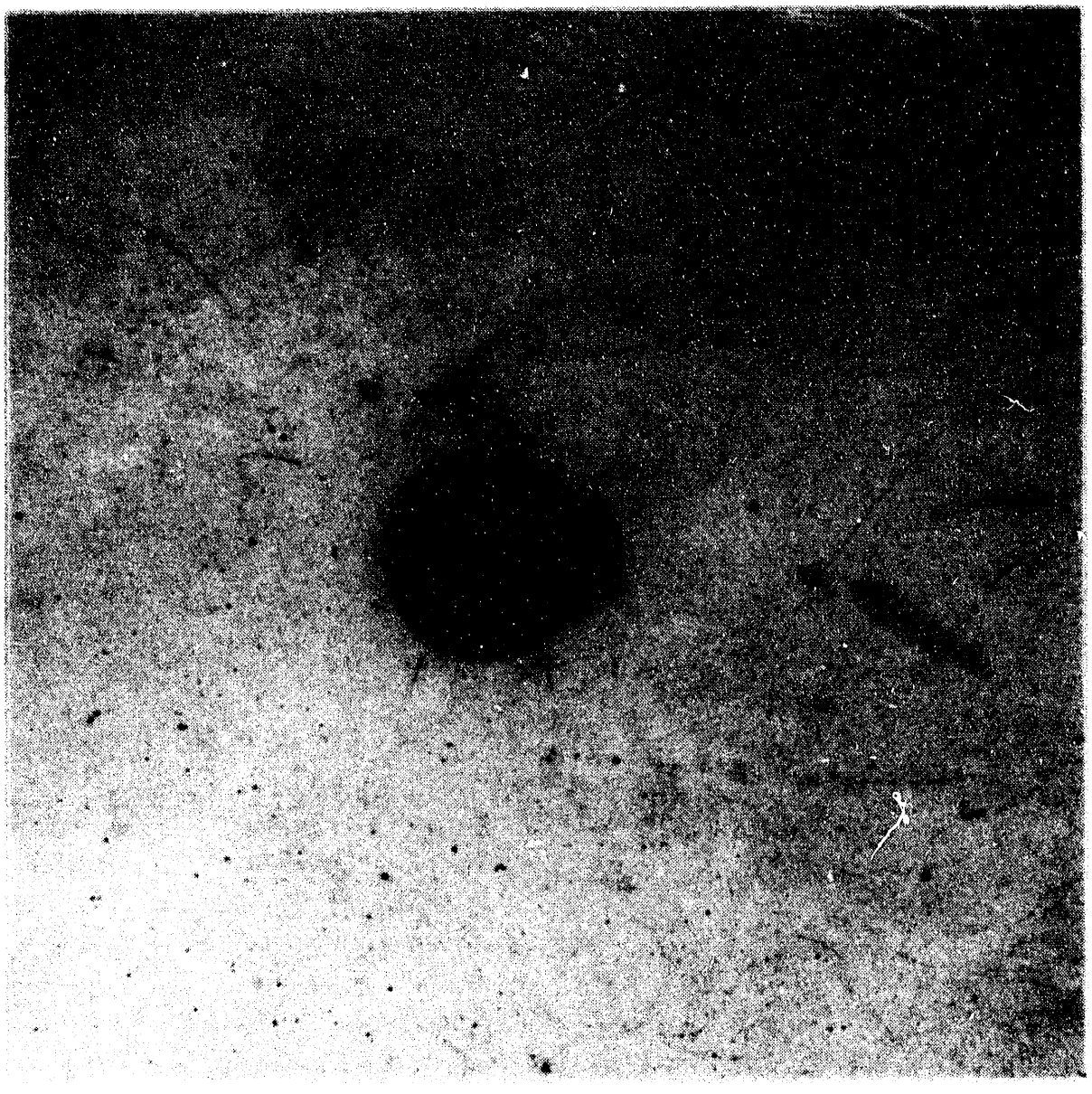

Test 12, Radiograph a ~

6.35 mm Steel Sphere Impact Velocity:	4470 m/s	5 mm
PMMA Target Thickness:	0.69 mm	

Figure B16. Test 12, Radiograph a.

Test 12, Radiograph b ~

6.35 mm Steel Sphere Impact Velocity:	4470 m/s	5 mm
PMMA Target Thickness:	0.69 mm	

Figure B17. Test 12, Radiograph b.

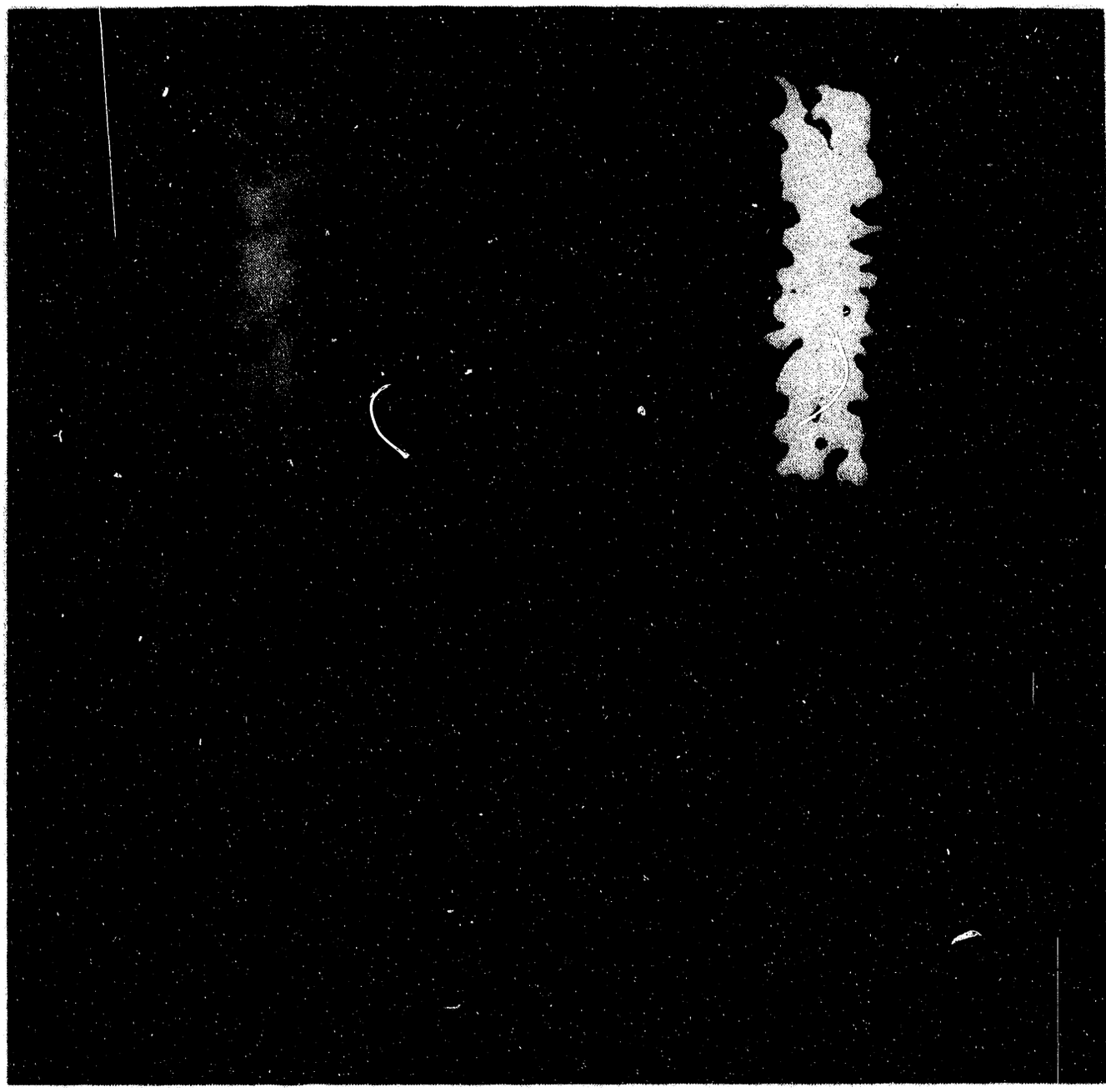

Test 13, Radiograph a ~

10 mm

6.35 mm Steel Sphere Impact Velocity: 4430 m/s
PMMA Target Thickness: 5.37 mm

Figure B18. Test 13, Radiograph a.

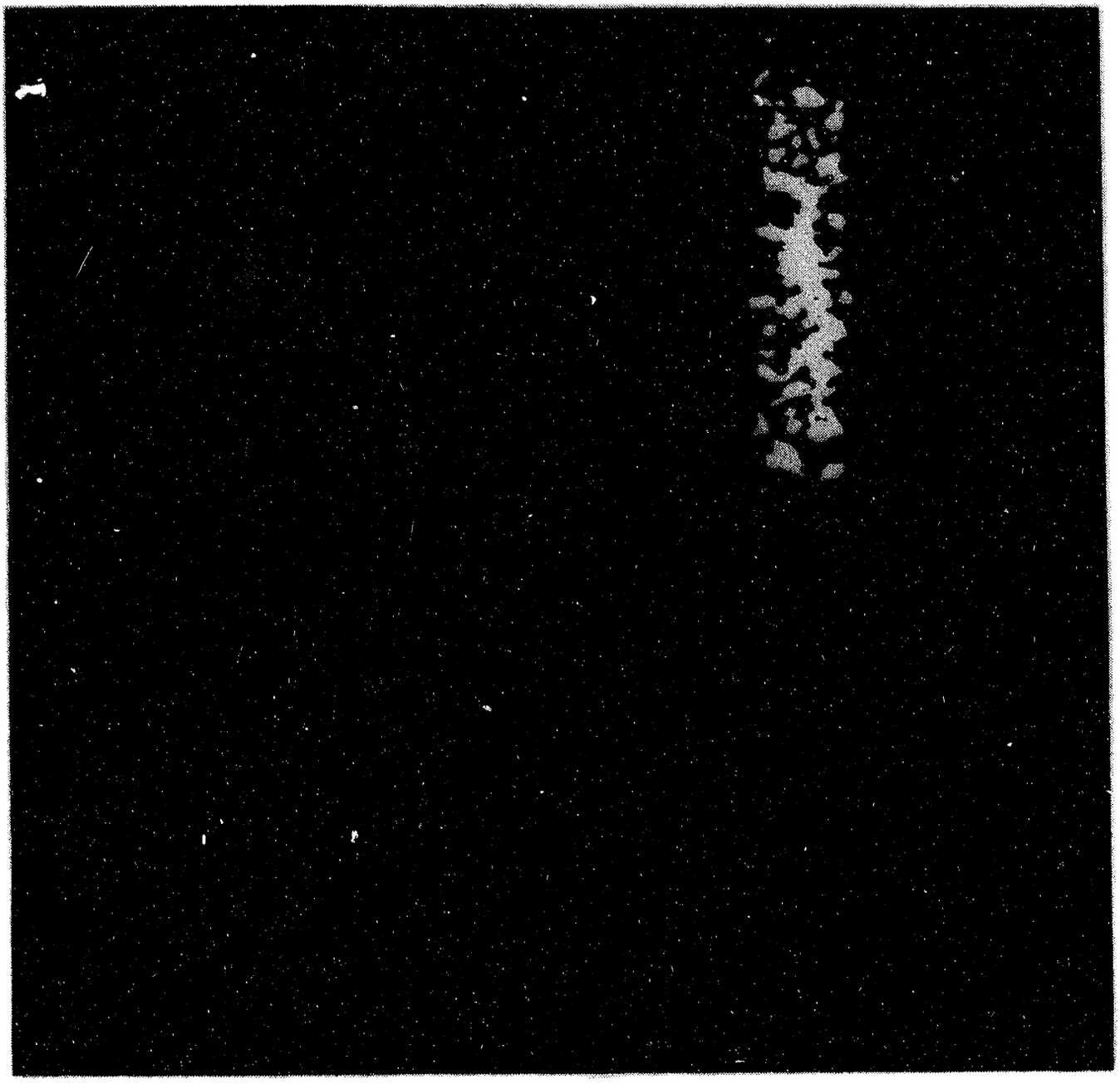

Test 13, Radiograph b ~

20 mm

6.35 mm Steel Sphere Impact Velocity: 4430 m/s
PMMA Target Thickness: 5.37 mm

Figure B19. Test 13, Radiograph b.

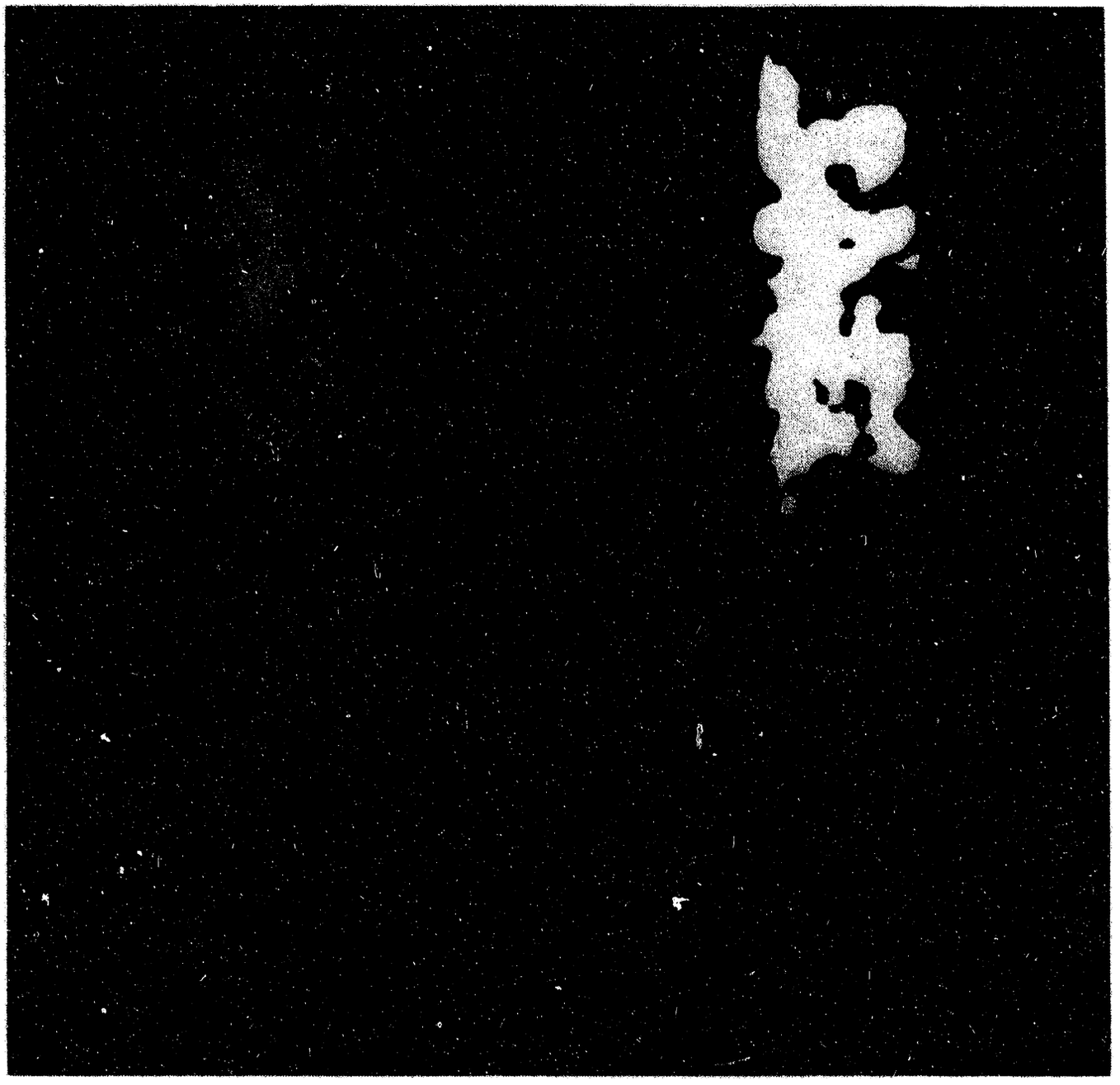

Test 14, Radiograph a ~

10 mm

6.35 mm Steel Sphere Impact Velocity:	4060 m/s
PMMA Target Thickness:	5.36 mm

Figure B20. Test 14, Radiograph a.

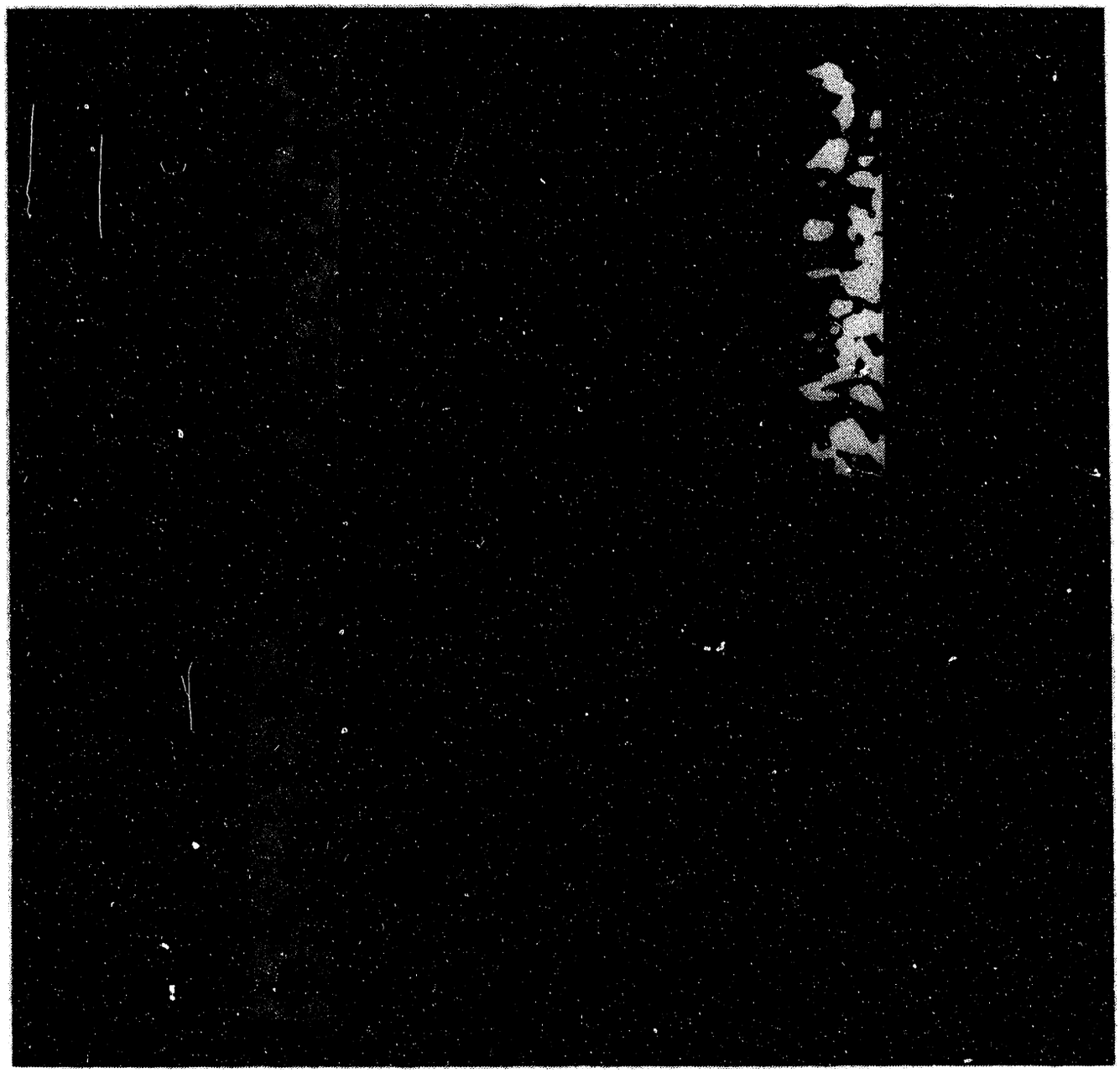

Test 14, Radiograph b ~

6.35 mm Steel Sphere Impact Velocity:	4060 m/s
PMMA Target Thickness:	5.36 mm

20 mm

Figure B21. Test 14, Radiograph b.

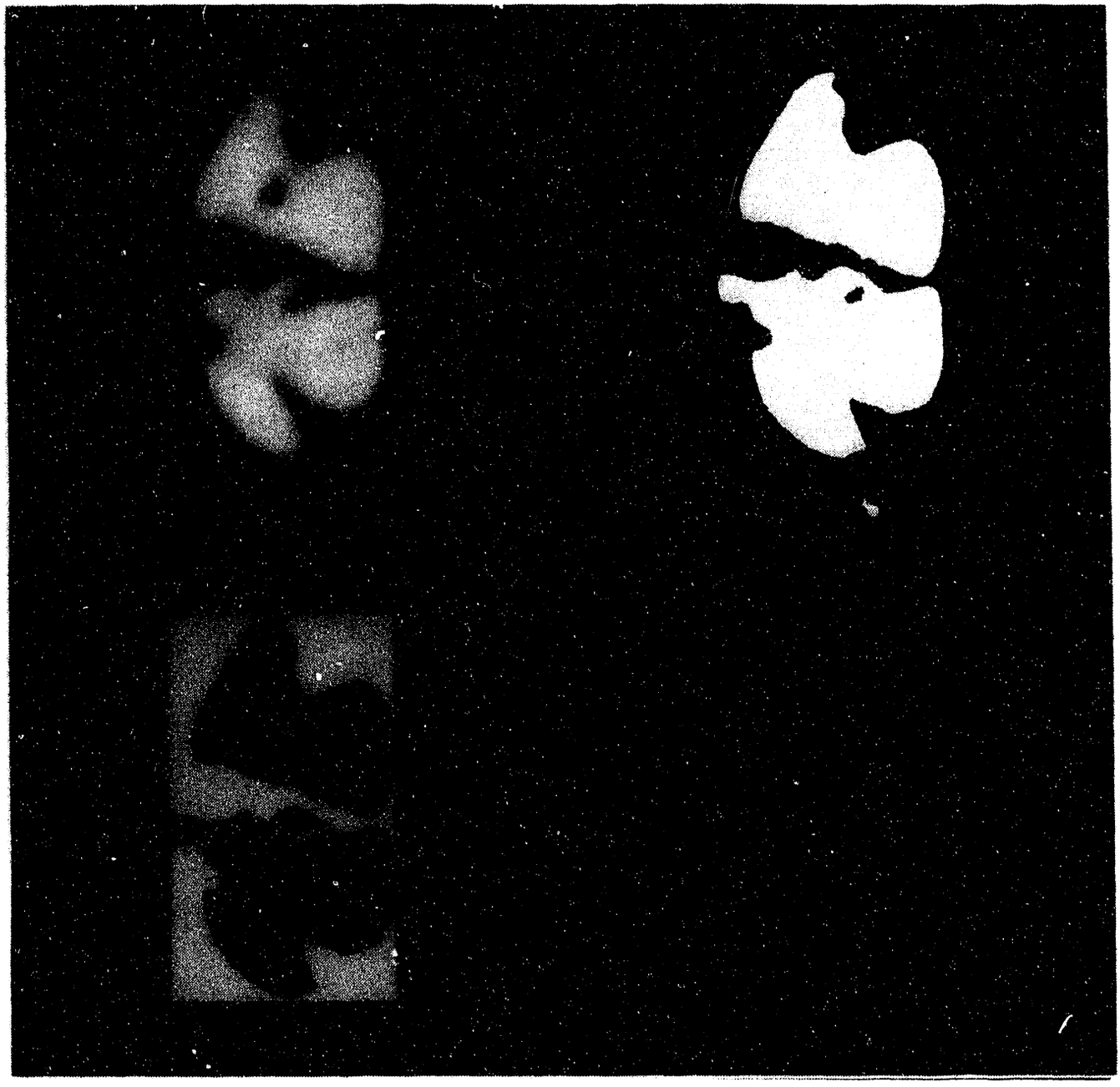

Test 15, Radiograph a ~

5 mm

6.35 mm Steel Sphere Impact Velocity: 3310 m/s
PMMA Target Thickness: 5.38 mm

Figure B22. Test 15, Radiograph a.

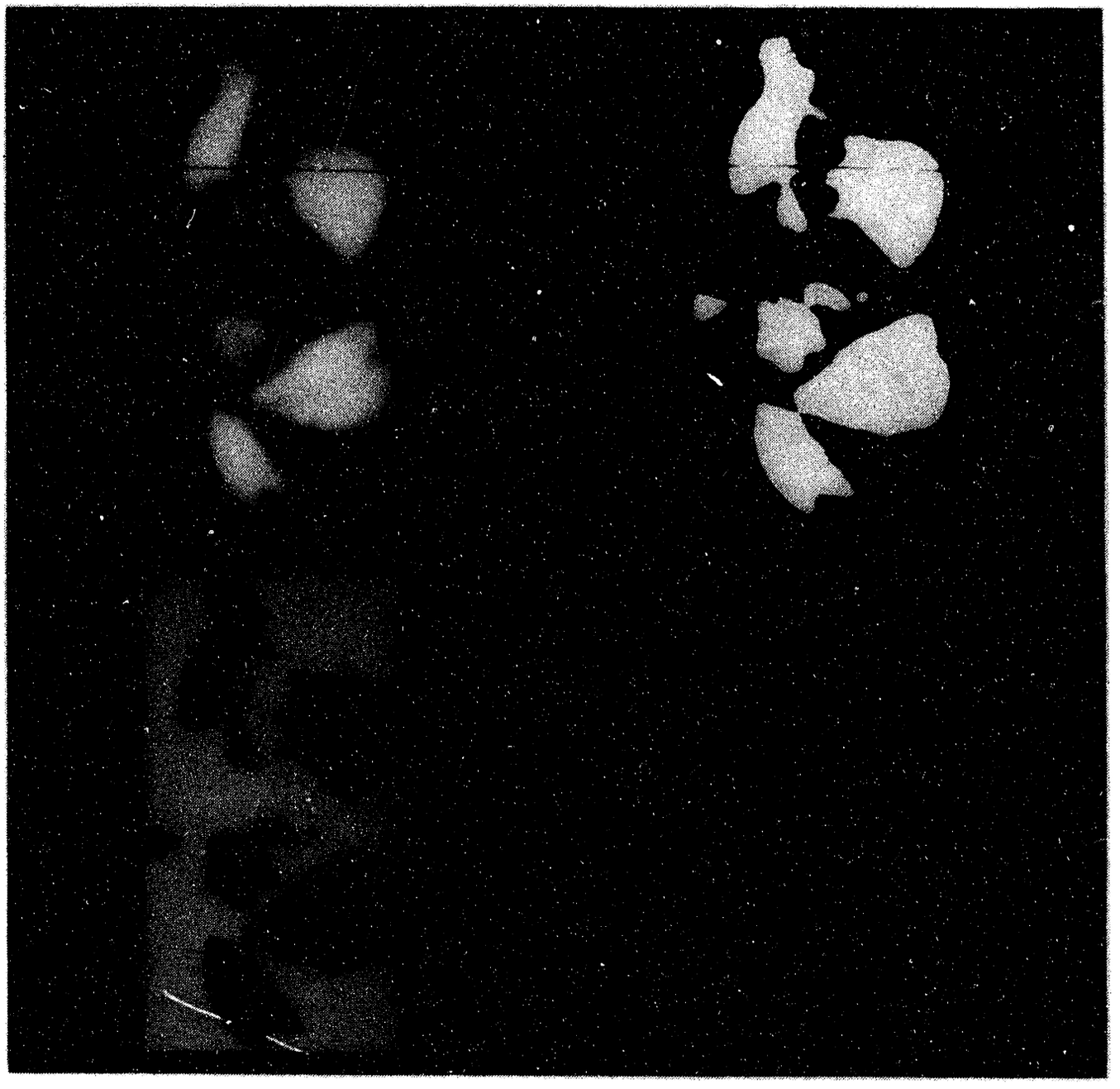

Test 15, Radiograph b ~

6.35 mm Steel Sphere Impact Velocity:	3310 m/s
PMMA Target Thickness:	5.38 mm

10 mm

Figure B23. Test 15, Radiograph b.

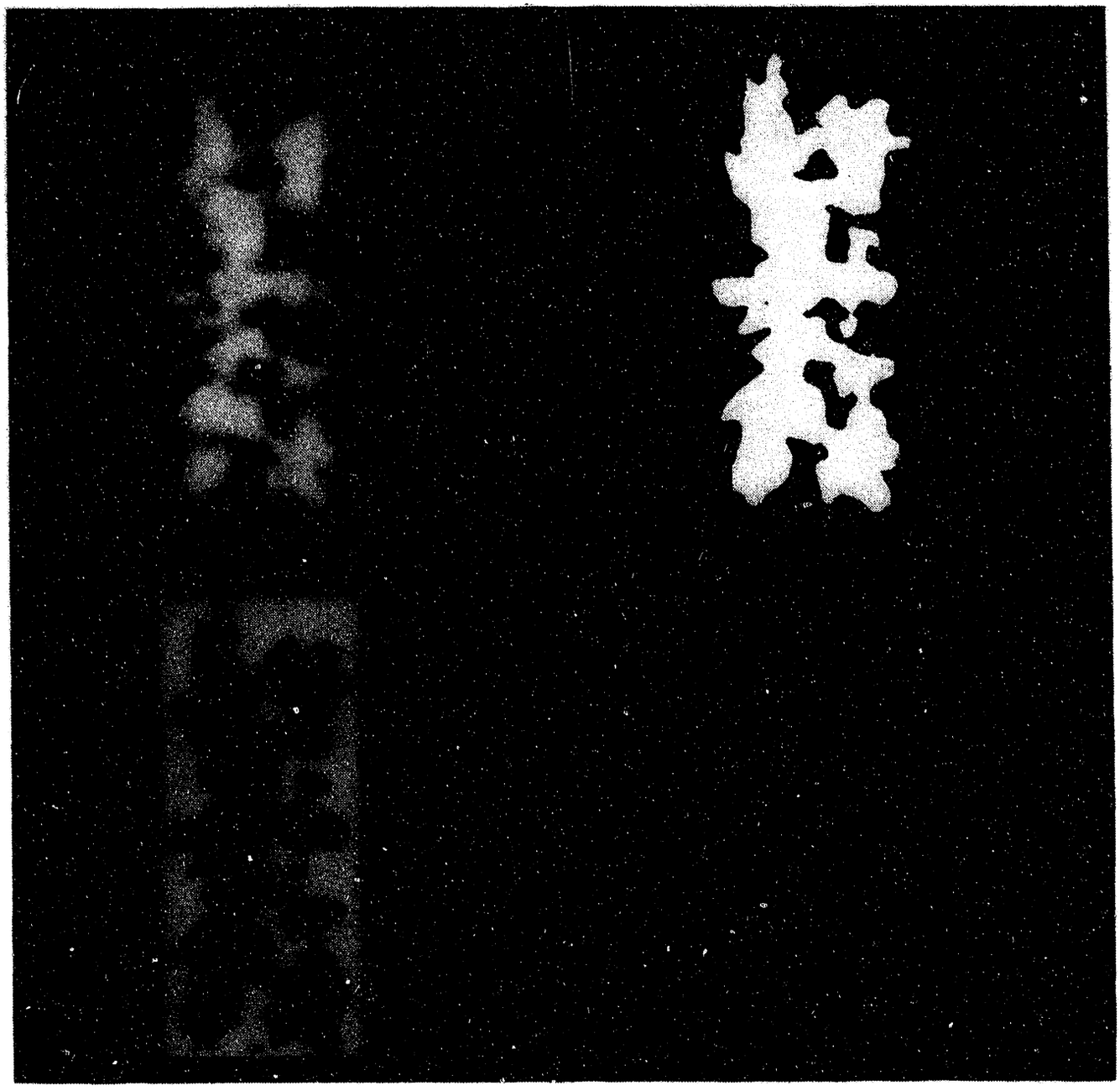

Test 16, Radiograph a ~

10 mm

6.35 mm Steel Sphere Impact Velocity:	4080 m/s
PMMA Target Thickness:	5.37 mm

Figure B24. Test 16, Radiograph a.

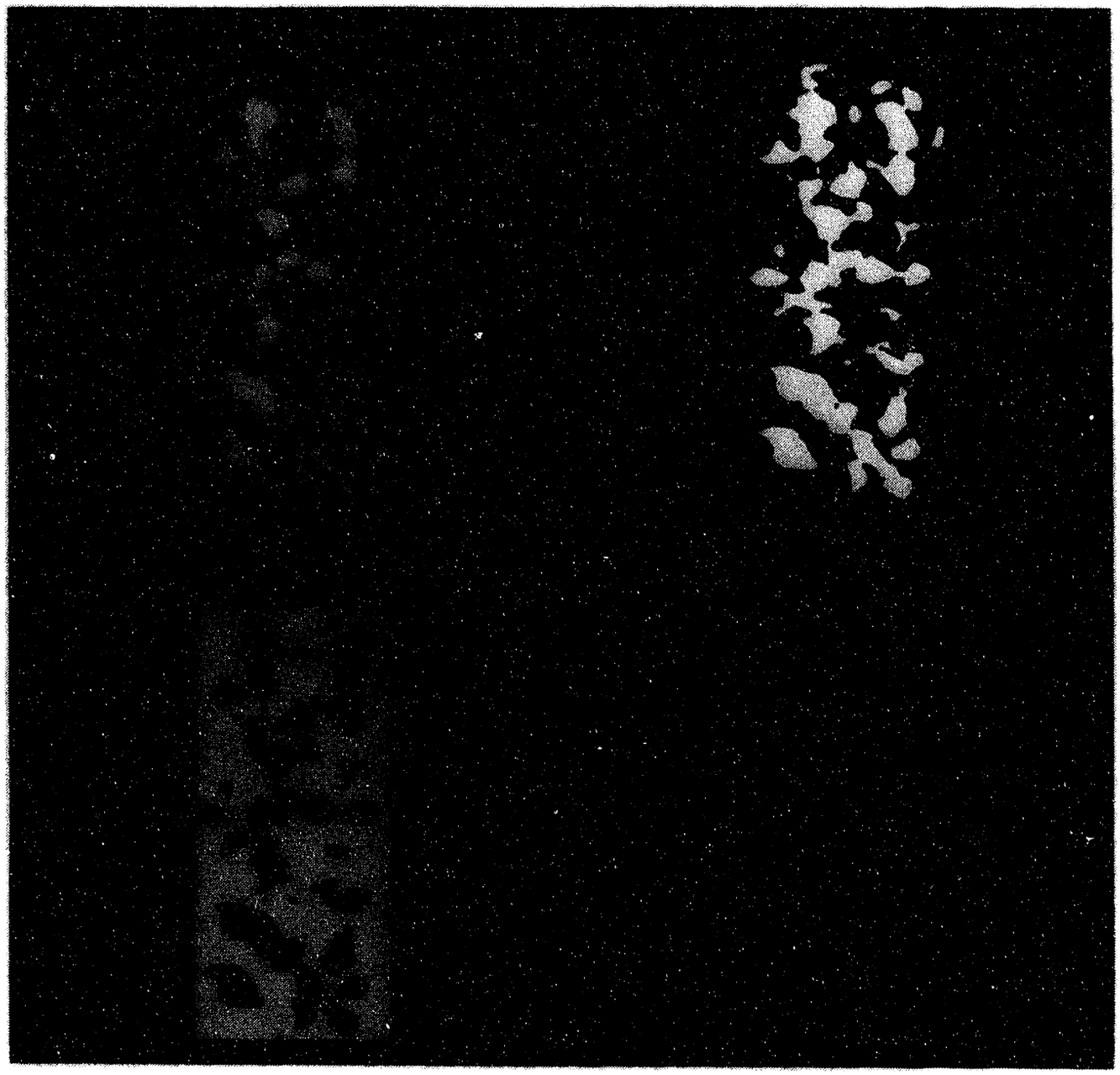

Test 16, Radiograph b ~

20 mm

6.35 mm Steel Sphere Impact Velocity: 4080 m/s
PMMA Target Thickness: 5.37 mm

Figure B25. Test 16, Radiograph b.

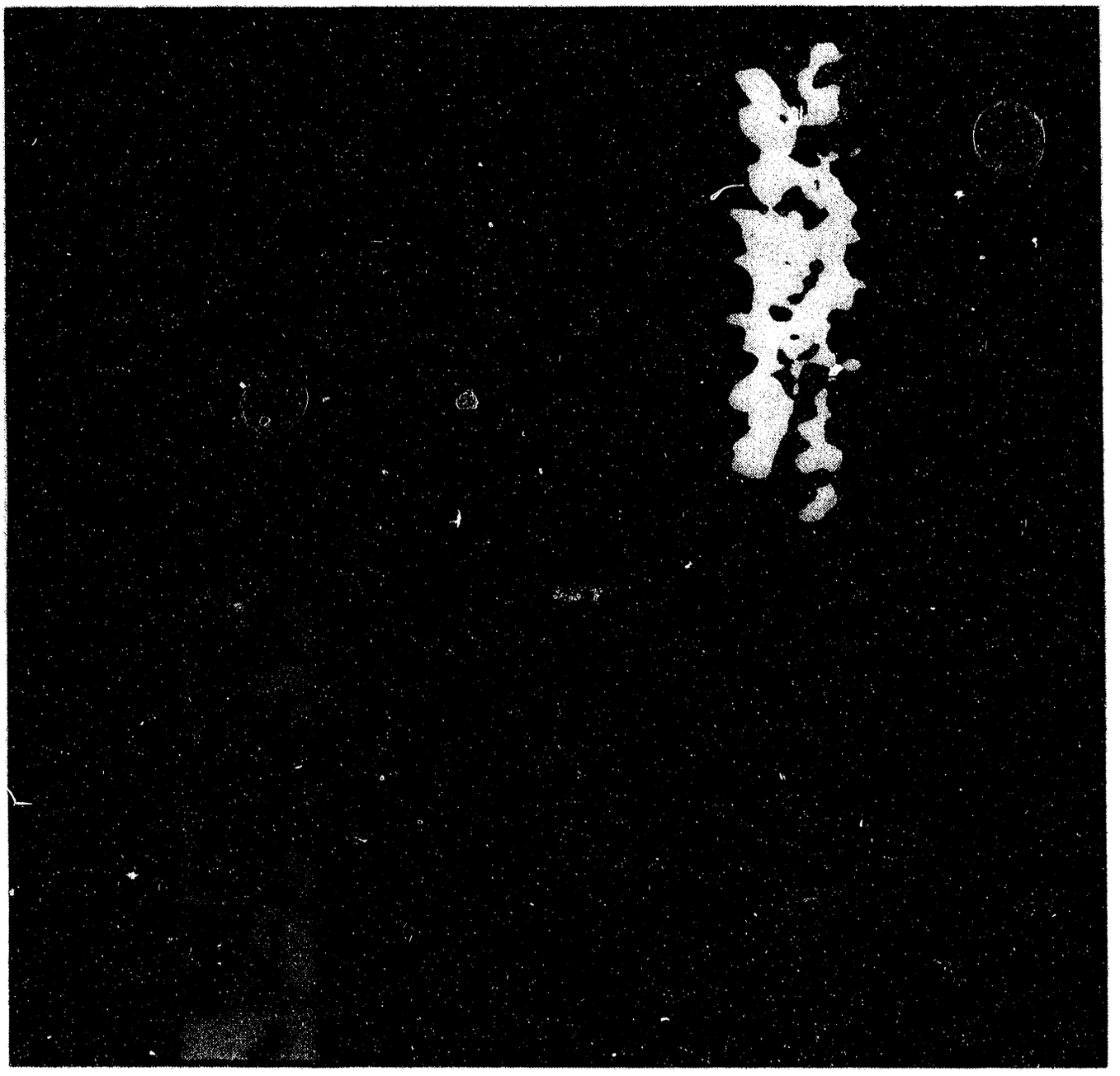

Test 17, Radiograph a ~

10 mm

6.35 mm Steel Sphere Impact Velocity:	4520 m/s
PMMA Target Thickness:	3.25 mm

Figure B26. Test 17, Radiograph a.

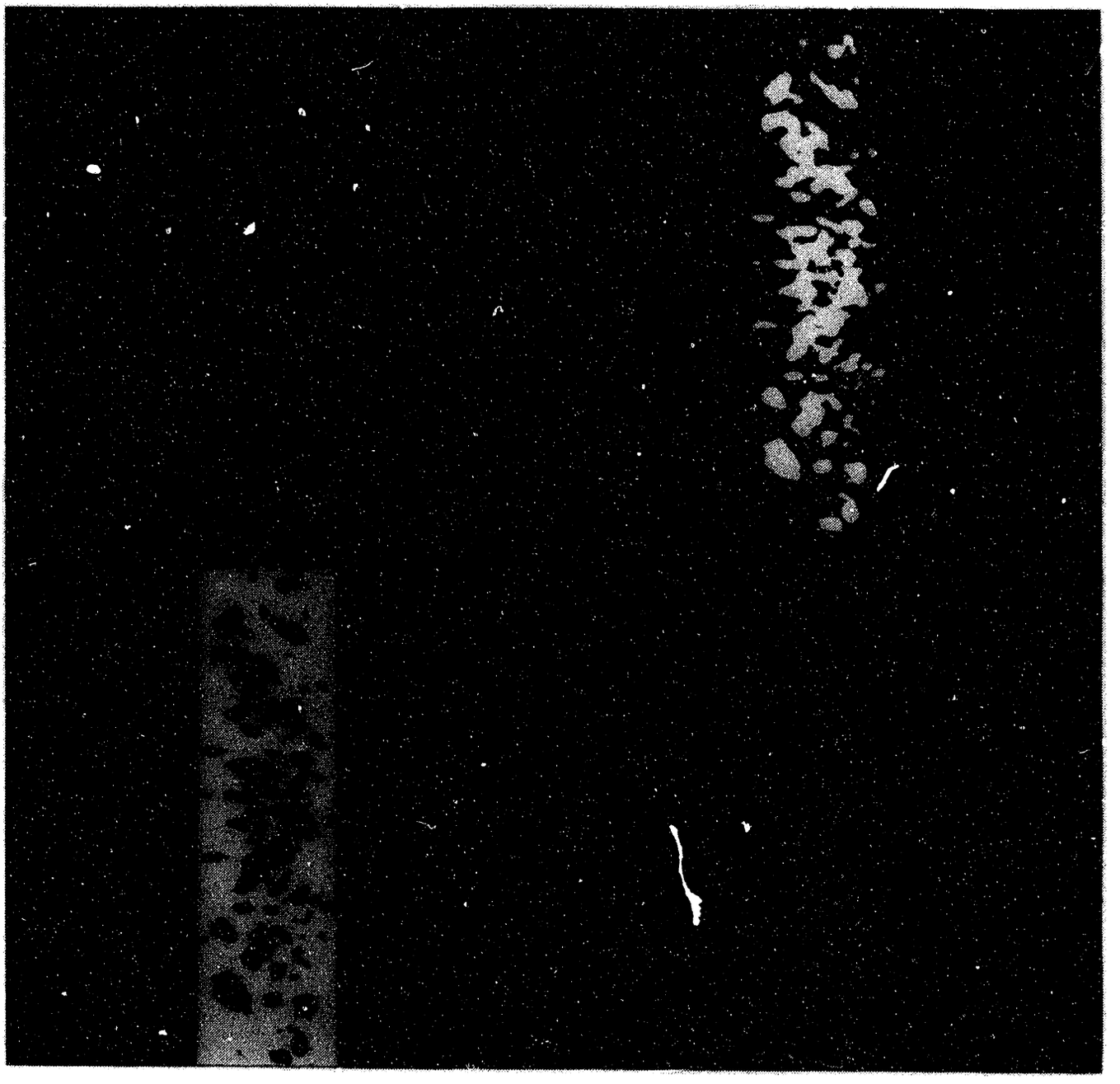

Test 17, Radiograph b ~

20 mm

6.35 mm Steel Sphere Impact Velocity:	4520 m/s
PMMA Target Thickness:	3.25 mm

Figure B27. Test 17, Radiograph b.

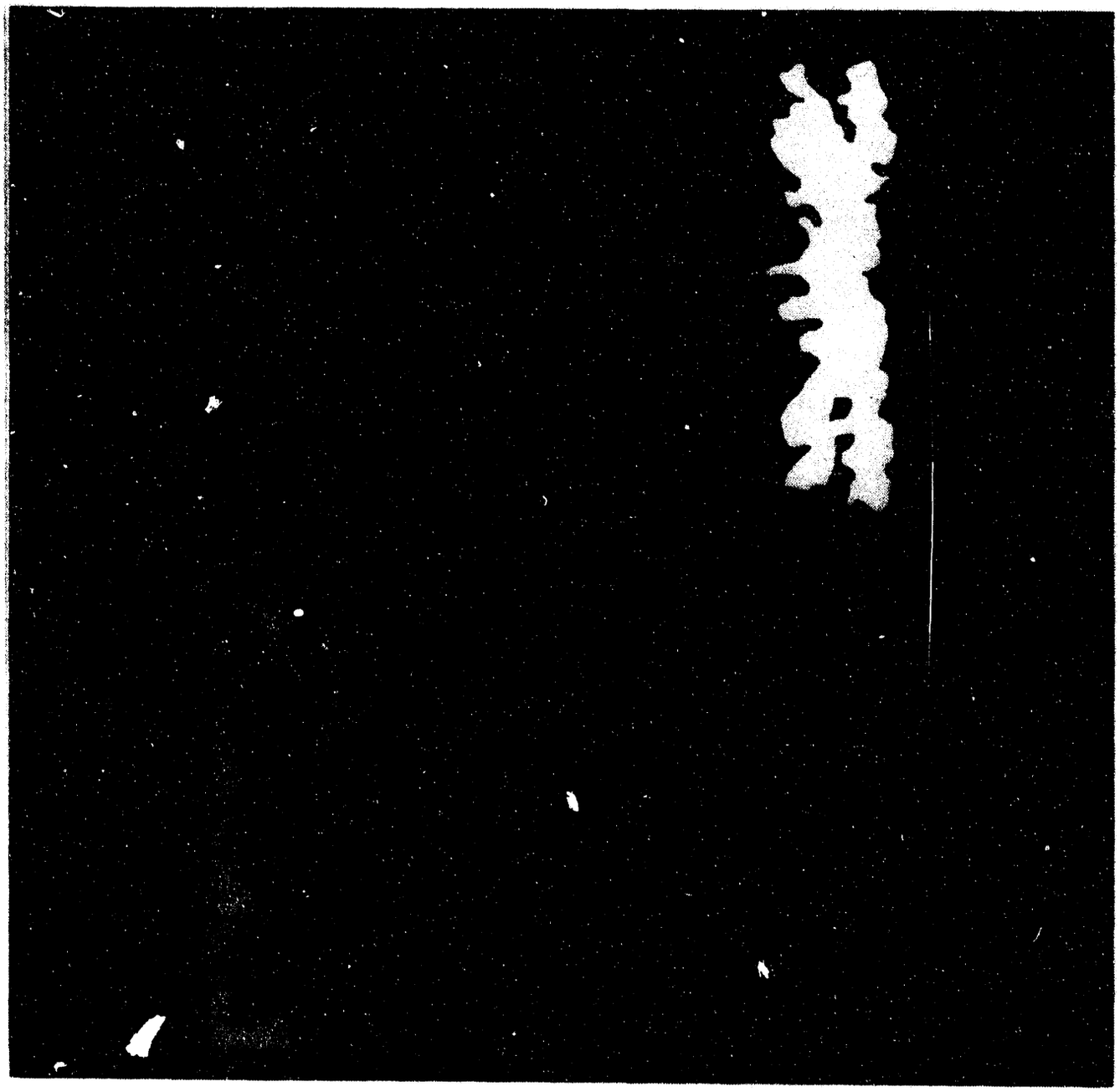

Test 18, Radiograph a ~

6.35 mm Steel Sphere Impact Velocity:	4430 m/s
PMMA Target Thickness:	4.71 mm

10 mm

Figure B28. Test 18, Radiograph a.

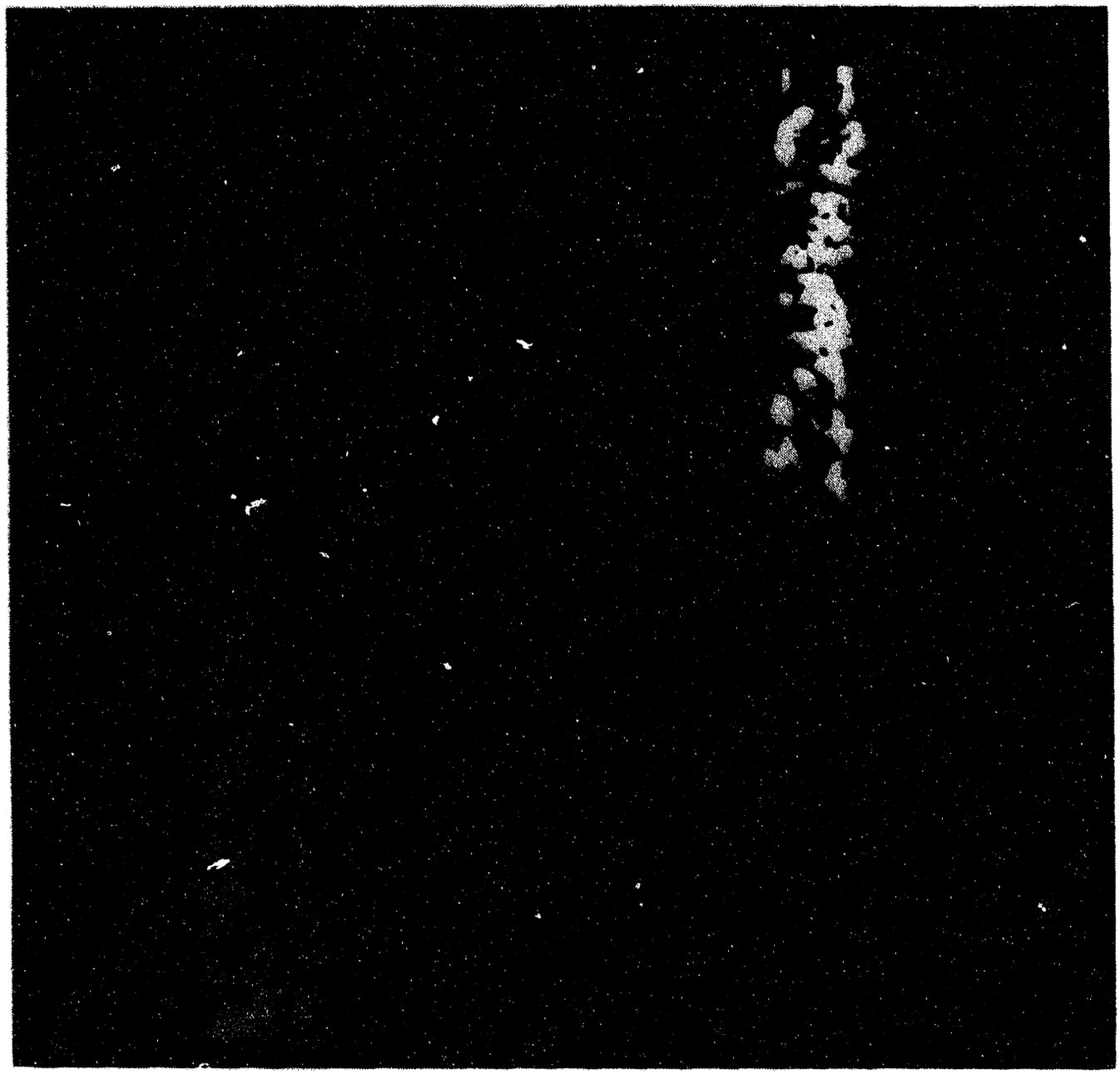

Test 18, Radiograph b ~

20 mm

6.35 mm Steel Sphere Impact Velocity: 4430 m/s
PMMA Target Thickness: 4.71 mm

Figure B29. Test 18, Radiograph b.

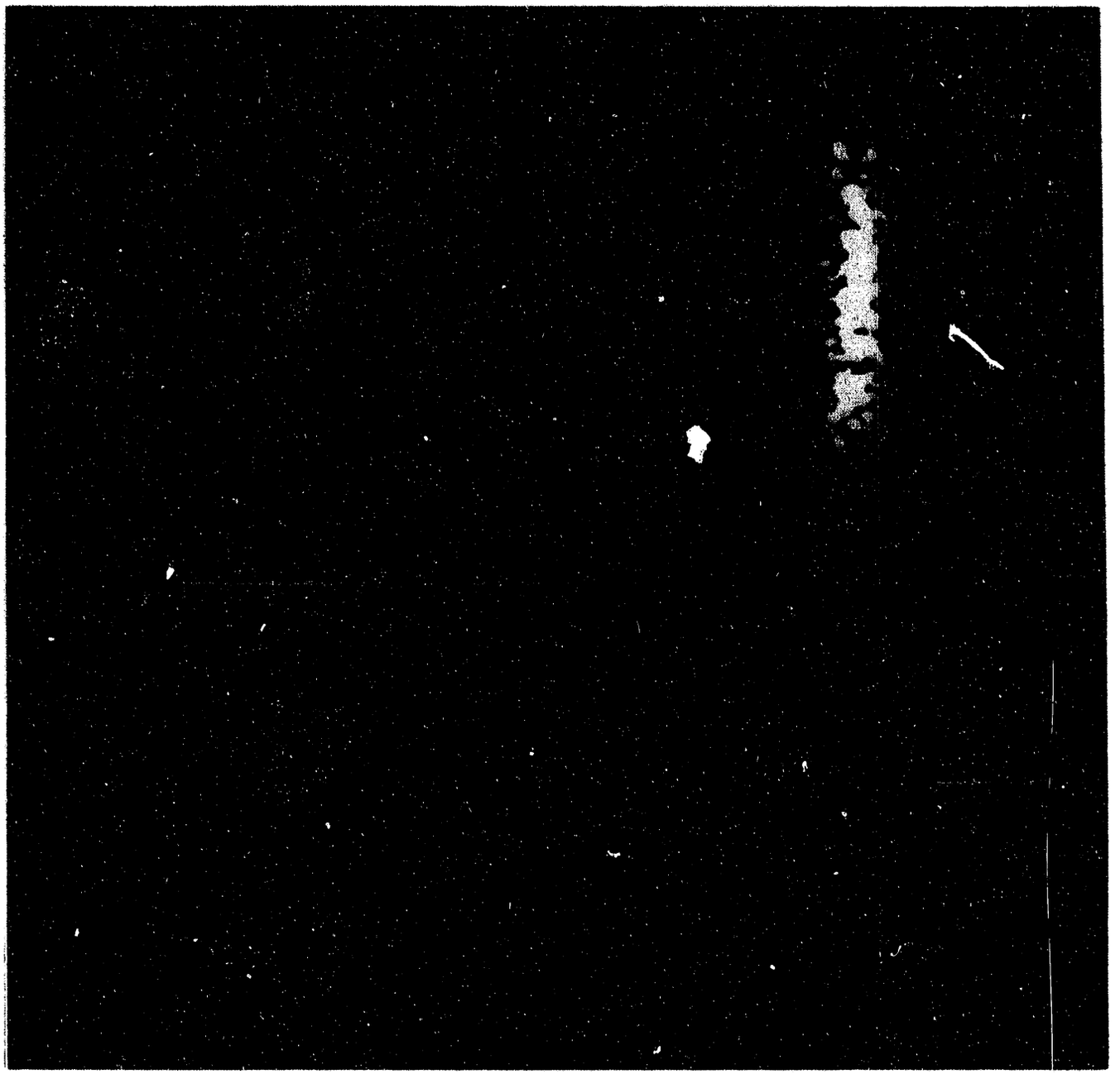

Test 19, Radiograph a ~

30 mm

6.35 mm Steel Sphere Impact Velocity: 4610 m/s
PMMA Target Thickness: 5.39 mm

Figure B30. Test 19, Radiograph a.

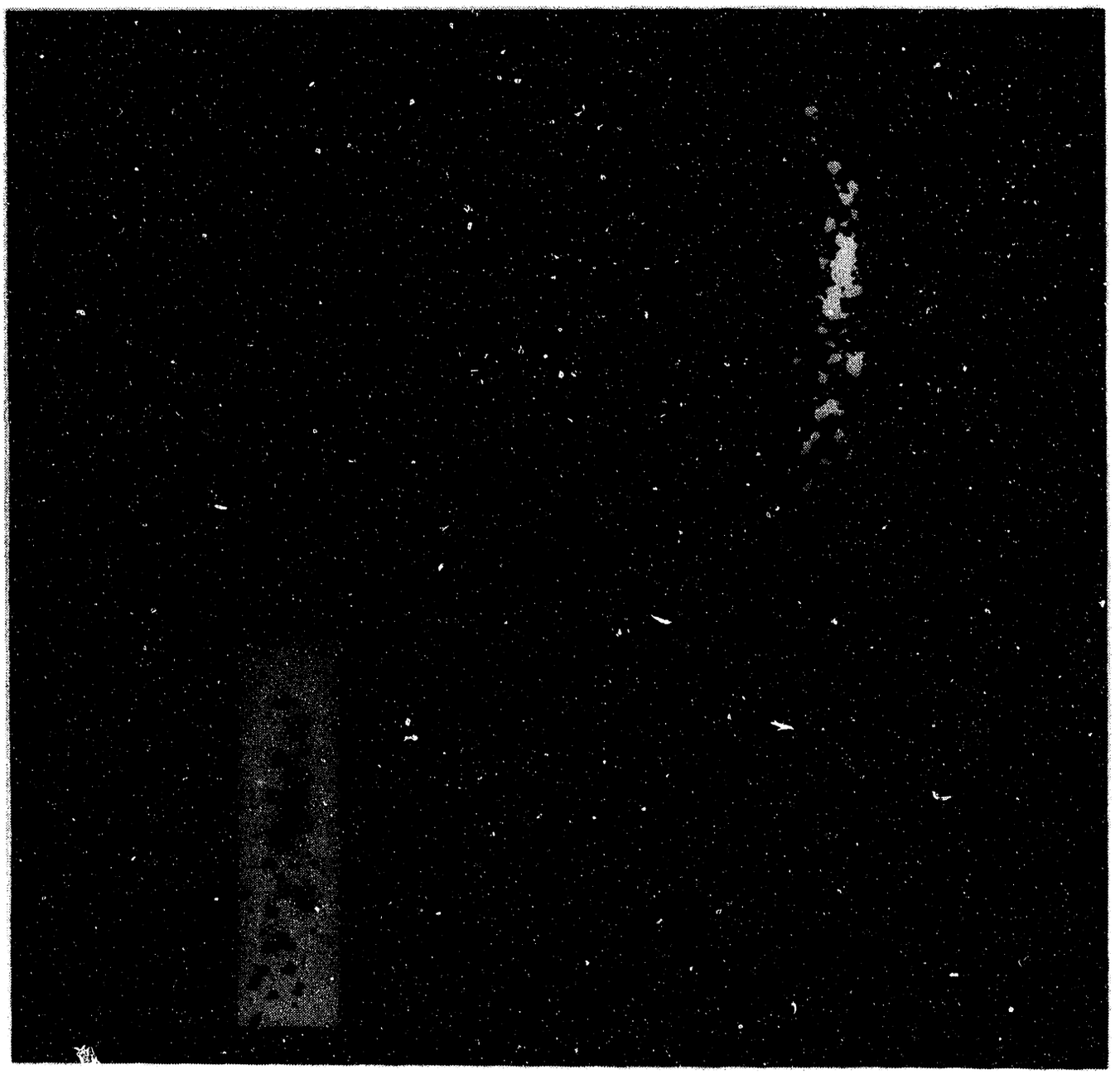

Test 19, Radiograph b ~

30 mm

6.35 mm Steel Sphere Impact Velocity: 4610 m/s
PMMA Target Thickness: 5.39 mm

Figure B31. Test 19, Radiograph b.

Test 20, Radiograph a ~

10 mm

6.35 mm Steel Sphere Impact Velocity:	4040 m/s
PMMA Target Thickness:	4.75 mm

Figure B32. Test 20, Radiograph a.

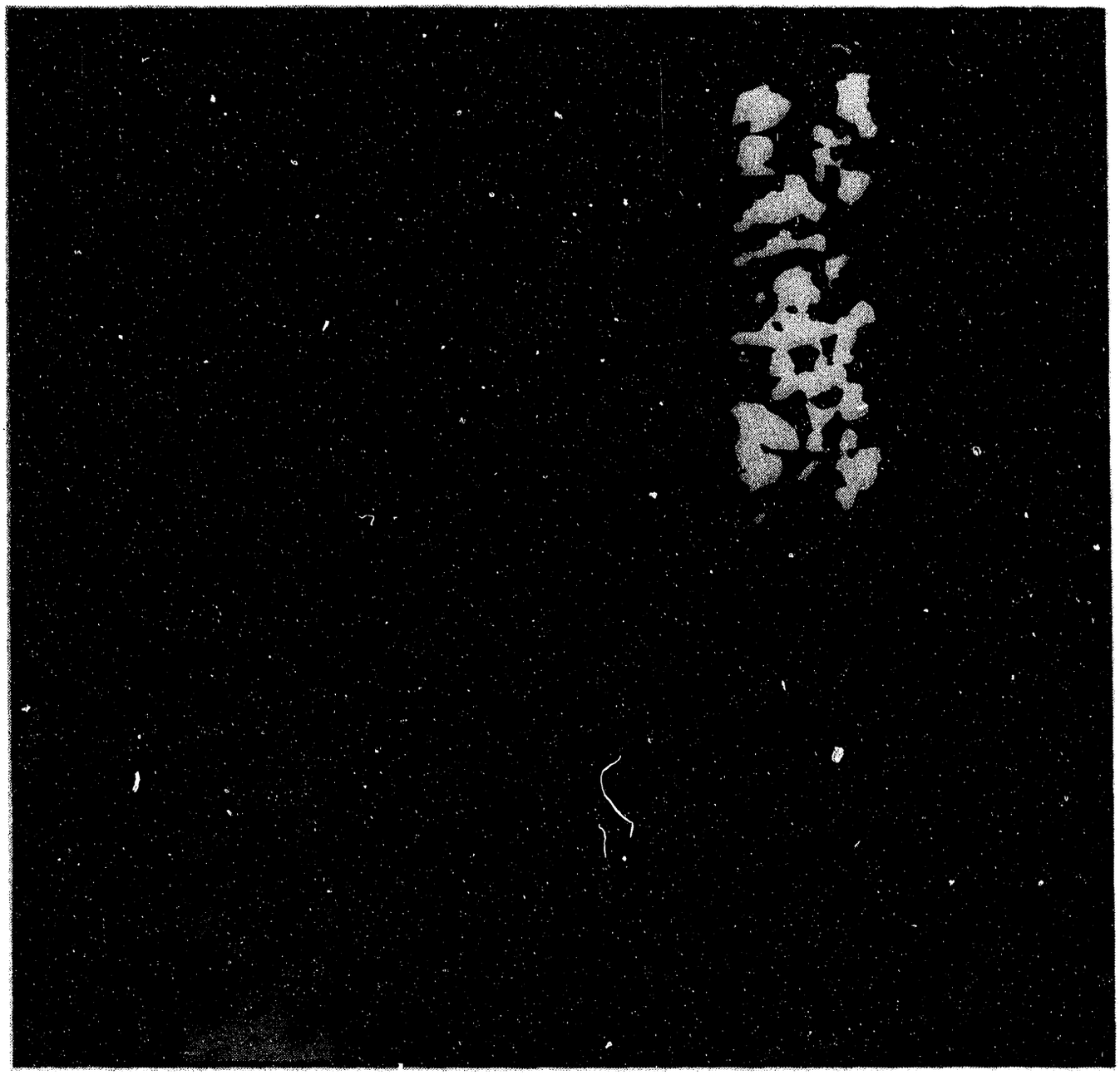

Test 20, Radiograph b ~

20 mm

6.35 mm Steel Sphere Impact Velocity: 4040 m/s
PMMA Target Thickness: 4.75 mm

Figure B33. Test 20, Radiograph b.

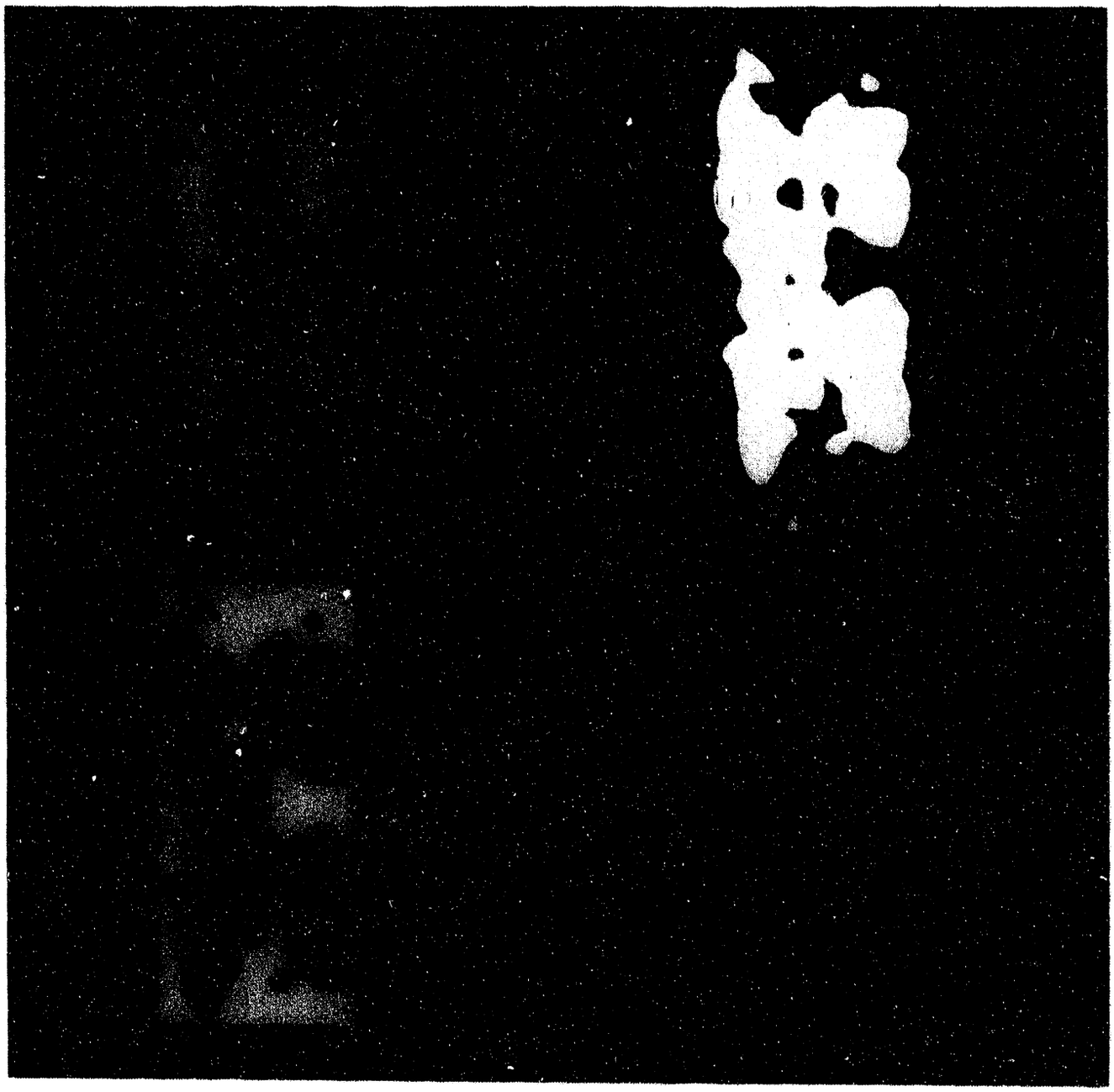

Test 21, Radiograph a ~

10 mm

6.35 mm Steel Sphere Impact Velocity: 3750 m/s
PMMA Target Thickness: 4.78 mm

Figure B34. Test 21, Radiograph a.

Test 21, Radiograph b ~

10 mm

6.35 mm Steel Sphere Impact Velocity: 3750 m/s
PMMA Target Thickness: 4.78 mm

Figure B35. Test 21, Radiograph b.

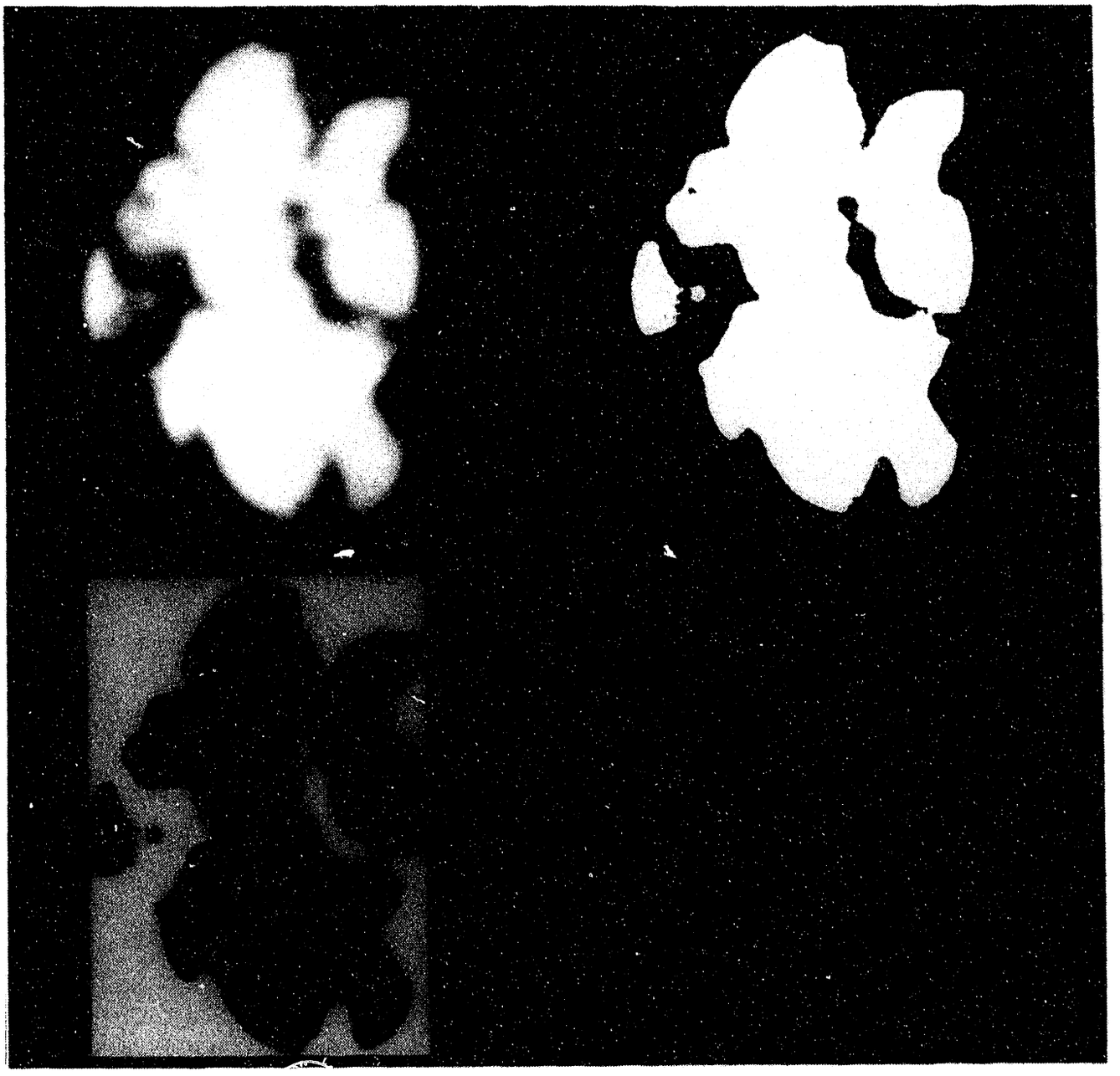

Test 22, Radiograph a ~

5 mm

6.35 mm Steel Sphere Impact Velocity:	4700 m/s
PMMA Target Thickness:	0.99 mm

Figure B36. Test 22, Radiograph a.

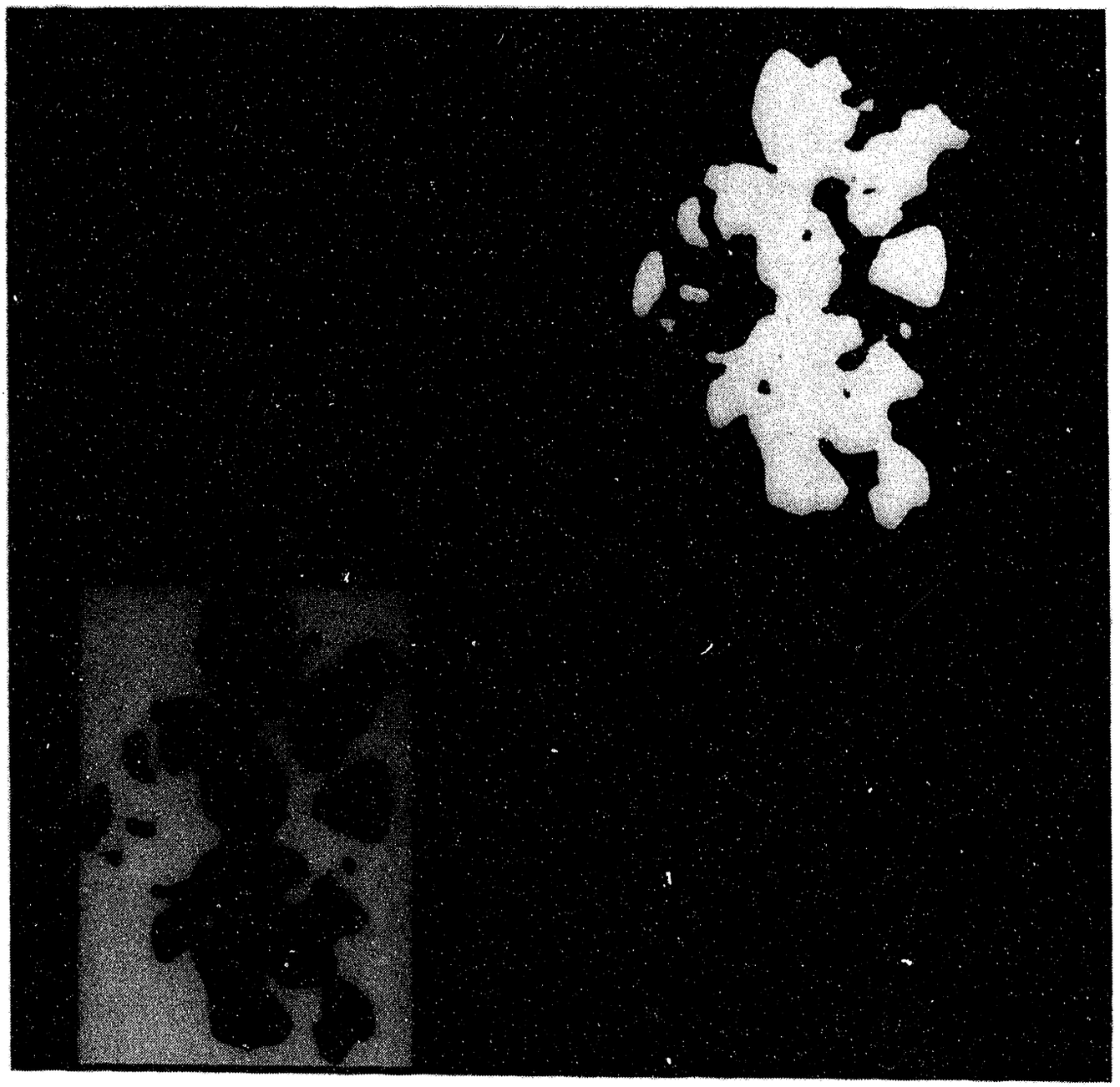

Test 22, Radiograph b ~

10 mm

6.35 mm Steel Sphere Impact Velocity: 4700 m/s
PMMA Target Thickness: 0.99 mm

Figure B37. Test 22, Radiograph b.

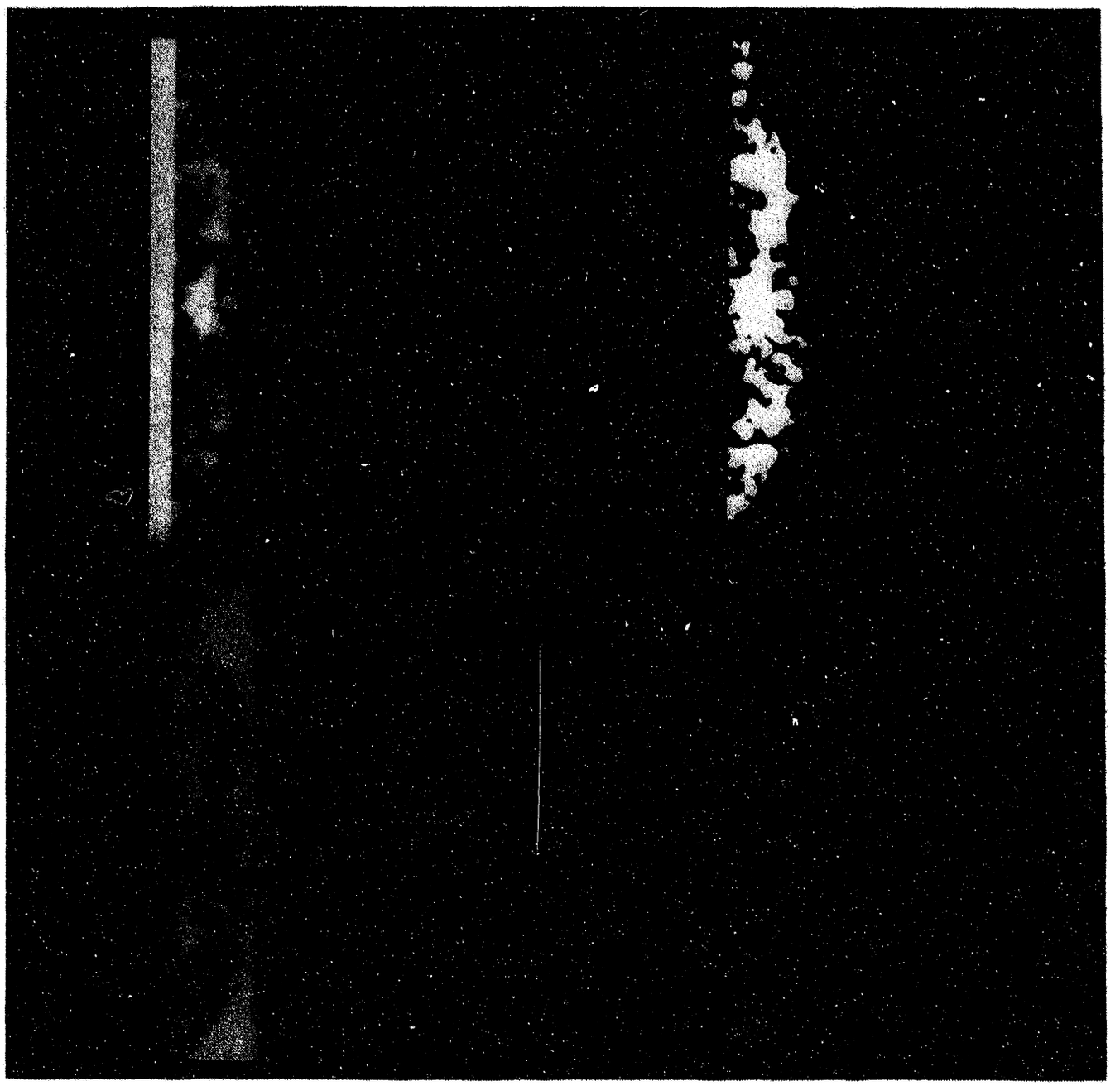

Test 23, Radiograph a ~

6.35 mm Steel Sphere Impact Velocity: 4060 m/s
PMMA Target Thickness: 11.23 mm

20 mm

Figure B38. Test 23, Radiograph a.

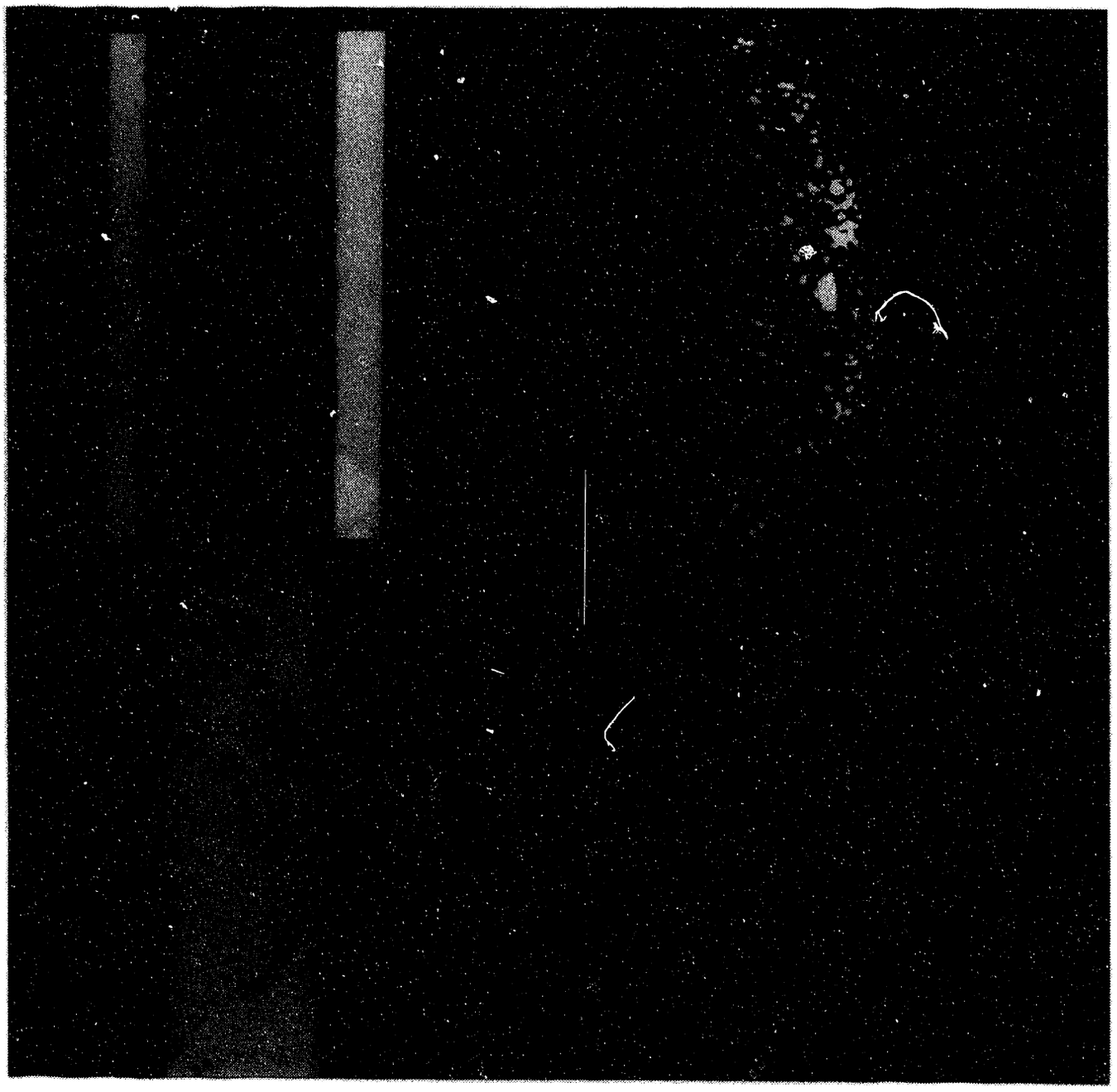

Test 23, Radiograph b ~

50 mm

6.35 mm Steel Sphere Impact Velocity: 4060 m/s
PMMA Target Thickness: 11.23 mm

Figure B39. Test 23, Radiograph b.

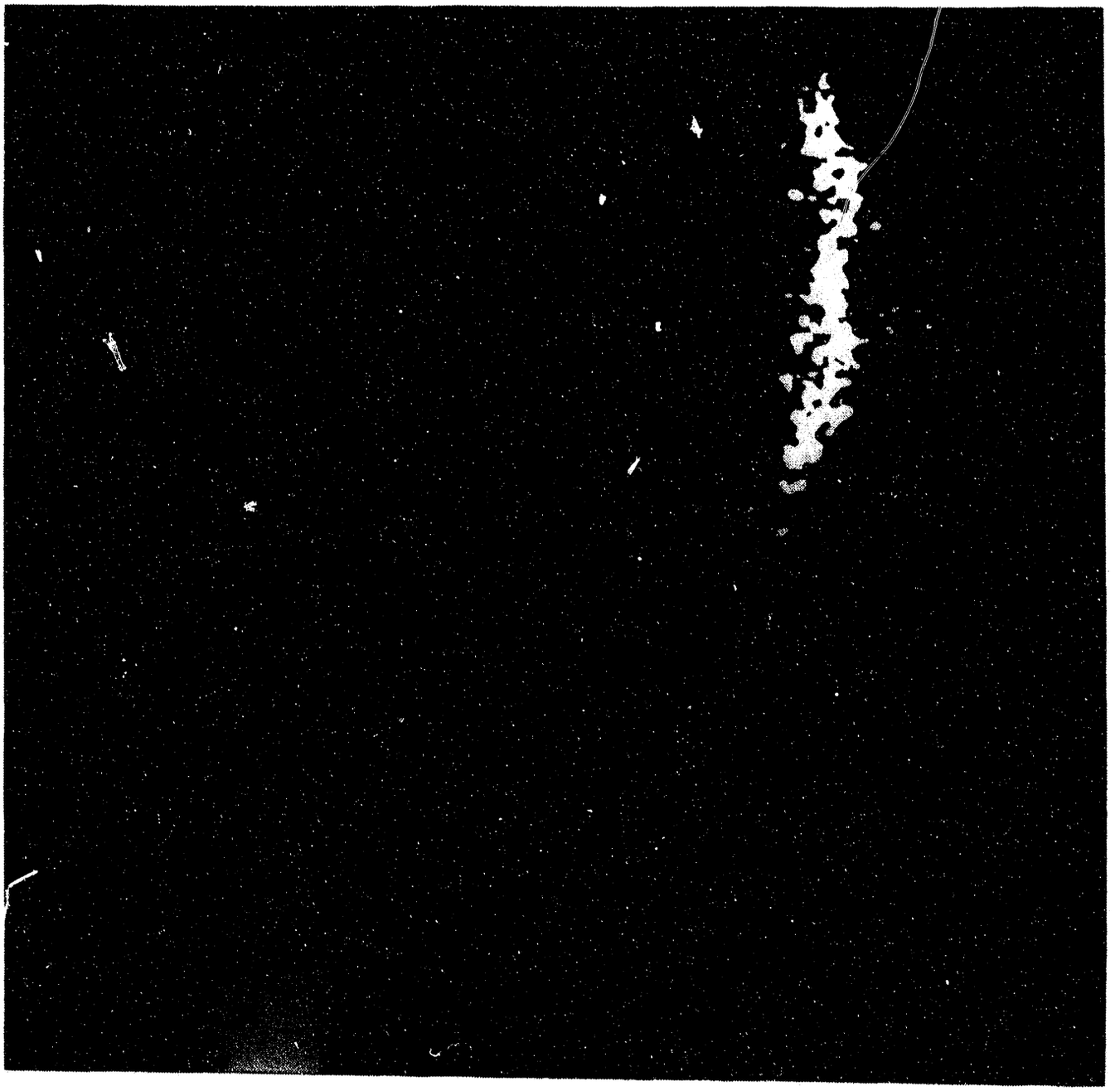

Test 24, Radiograph a ~

20 mm

6.35 mm Steel Sphere Impact Velocity: 4030 m/s
PMMA Target Thickness: 9.47 mm

Figure B40. Test 24, Radiograph a.

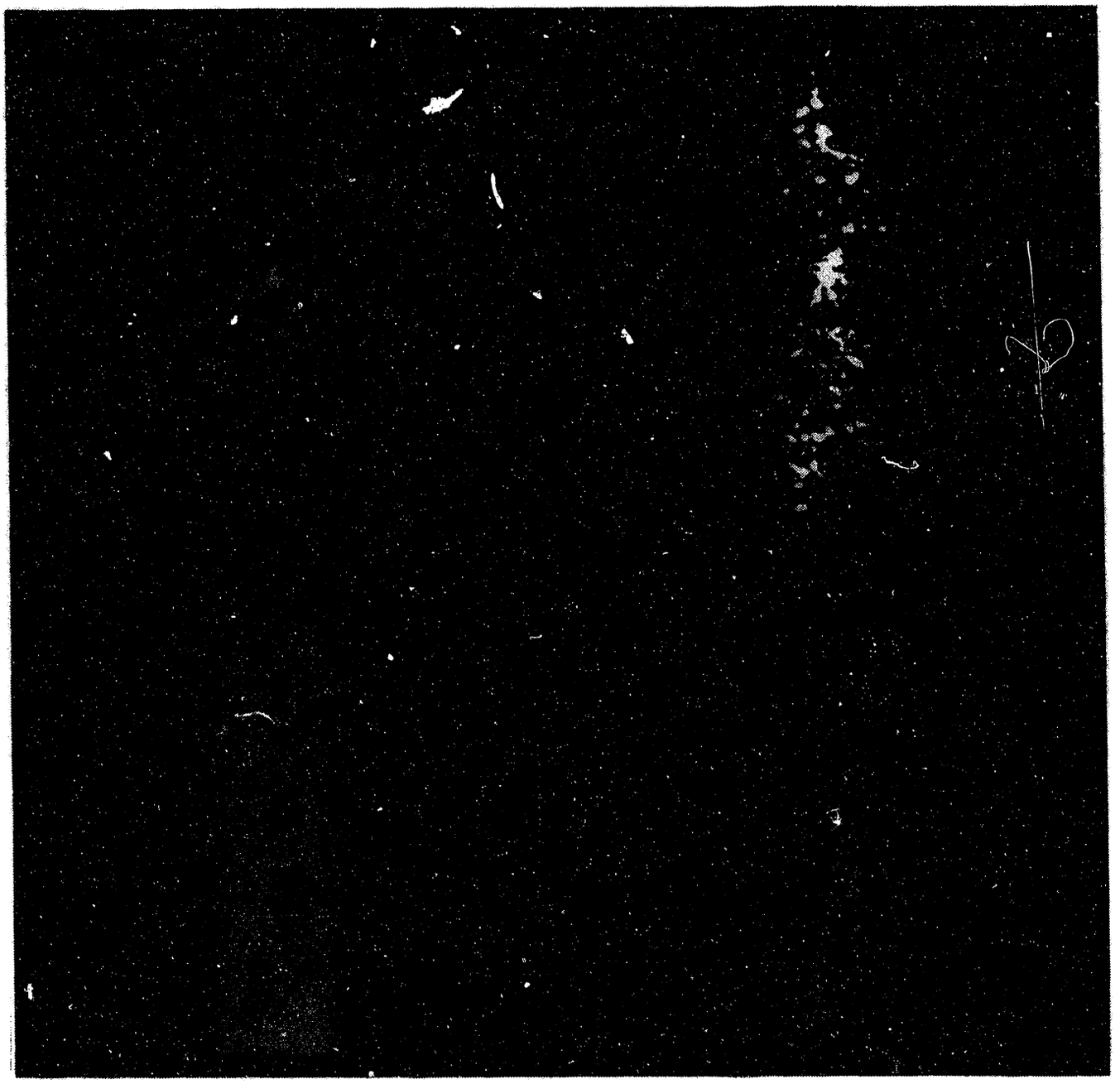

Test 24, Radiograph b ~

30 mm

6.35 mm Steel Sphere Impact Velocity: 4030 m/s
PMMA Target Thickness: 9.47 mm

Figure B41. Test 24, Radiograph b.

APPENDIX C - Foam Block Radiographs (Copper Impacts onto Steel Targets)

The radiographic data acquired of the foam blocks in two of the impact fragmentation events are included in the present appendix. The original radiograph is the upper left image in the figure. Each radiograph has been image-processed, and the results from those operations are included also: the upper right image is the digitized radiograph; the lower left is the same image with the encompassing envelope; and the lower right is the digitized outline of the fragments in the radiograph.

Figure C1. Radiograph of foam block for Test 1.

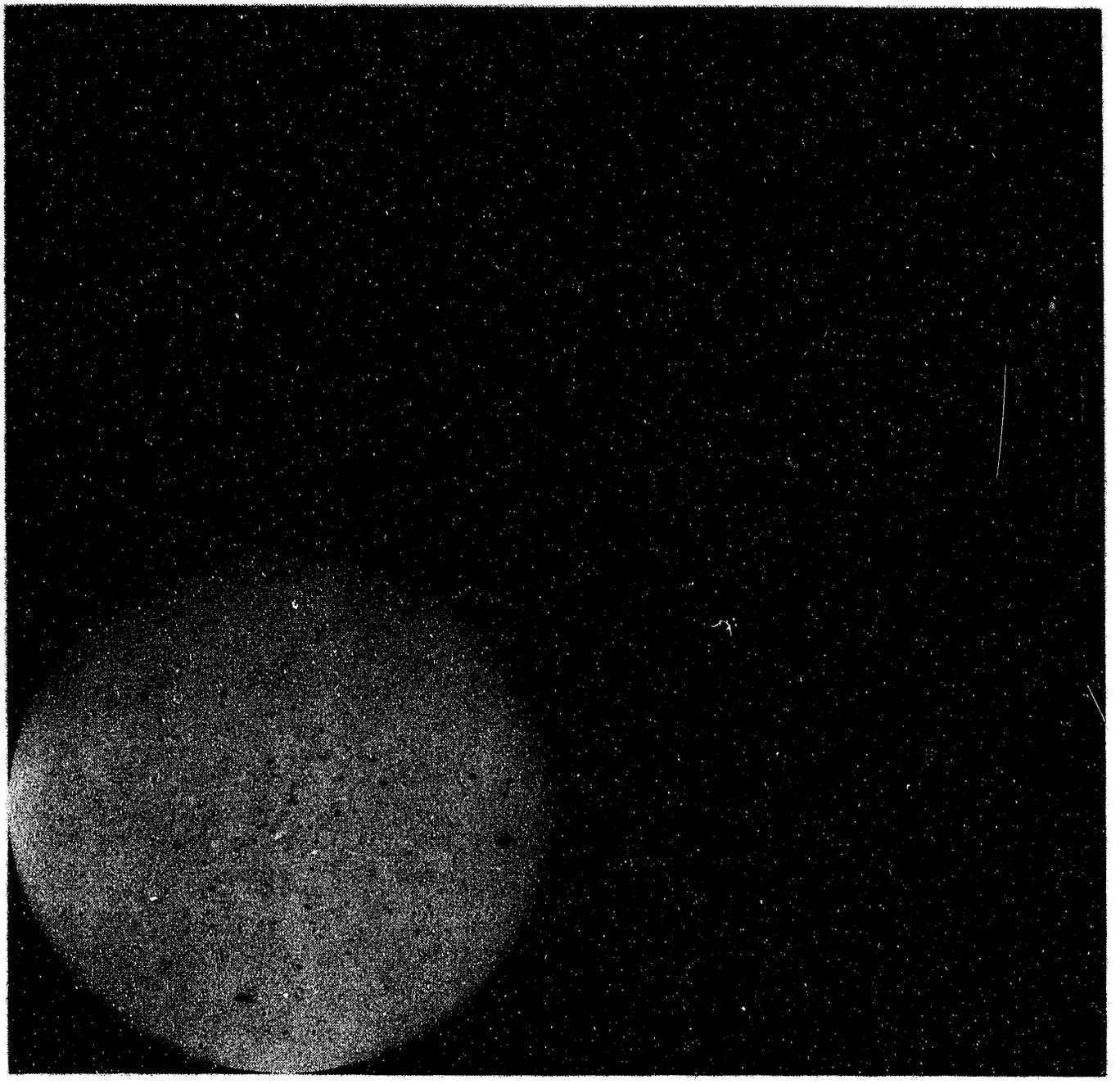

Figure C2. Radiograph of foam block for Test 3.

DISTRIBUTION

Prof. Thomas J. Ahrens
Seismological Laboratory 252-21
California Institute of Technology
Pasadena, CA 91125

Dr. Firroz Allahdadi
PL-NT1
Kirtland AFB
Albuquerque, NM 87117

Dr. Marv L. Alme
Alme and Associates
102 Stevens Forest Professional Center
9650 Santiago Road
Columbia, MD 21045

Charles E. Anderson
Southwest Research Institute
6220 Culebra Road
P. O. Drawer 28510
San Antonio, TX 78228-0510

Hu Bayi
Southwest Institute of Fluid Physics
P. O. Box 523-51, Chengdu
Sichuan, 610003, CHINA

Defense Advanced research Projects Agency
3701 North Fairfax Drive
Arlington, VA 22203-1714
Attn: J. Beno
Attn: R. Kocher

Stephen Bless
Institute for Advanced Technology
The University of Texas at Austin
4030-2 W. Braker Lane
Austin, TX 78759

William T. Brown
Applied Research Associates
2750 Eisenhower Avenue
Suite 104
Alexandria, VA 22314

Dr. Jeanne Crewes
NASA
Johnson Space Center
Mail Code SN3
Houston, TX 77058

Dr. Donald R. Curran
SRI International
333 Ravenswood Avenue
Menlo Park, CA 94025

Mr. Nick Dispenziere
Technology Development Associates
992 Old Eagle School Road
Suite 910
Wayne, PA 19087

Stephen Finnegan
Department of the Navy
Code 3894
Naval Air Warfare Center -
Weapons Division
China Lake, CA 93555-6001

Joseph C. Foster
Wright Laboratory
WL/MNMW
Eglin AFB, FL 32542-5434

Dr. Y. M. Gupta
Dept. of Physics
Washington State University
Pullman, WA 99164

Dr. Manfred Held
MBB Schrobenhausen
Schrobenhausen, 8898
GERMANY

William H. Holt
Naval Surface Warfare Center
Mail Code G22
Dahlgren, VA 22448-5000

Dr. Friedrich Horz
NASA
Lyndon B. Johnson Space Center
Houston, TX 77058

Dr. R. R. Ijsselstein
Ammunition Functioning & Explosives Group
Prins Maurits Laboratory TNO
P. O. Box 452280 AA Rijswijk
The Netherlands

Dr. Kailasam Iyer
U. S. Army Research Office
P. O. Box 12211
Research Triangle Park, NC 27709

Dr. Zeev Jaeger
Israel Atomic Energy Commission
Soreq Nuclear Research Centre
Yavne 70600
Israel

Gordon R. Johnson
7225 Northland Drive
Mail Station MN48-3700
Brooklyn Park, MN 55428

Kent Kimsey
U. S. Army Research Laboratory
Attn: AMSRL-WT-TC
Aberdeen Proving Ground, MD 21005-5066

John Kinecke
U. S. Army Research Laboratory
ATTN: AMXBR-TBD
Aberdeen Proving Ground, MD 21005-5066

Prof. Wolfgang Knauss
California Institute of Technology
Pasadena, CA 91125

Headquarters, Defense Nuclear Agency
Attn: SPSP (R. Jeffery Lawrence)
6801 Telegraph Road
Alexandria, VA 22310-3398

David L. Littlefield
Southwest Research Institute
6220 Culebra Road
P. O. Drawer 28510
San Antonio, TX 78228-0510

Prof. H. J. Melosh
Lunar and Planetary Laboratory
University of Arizona
Tucson, AZ 85721

Dr. S. Nemat-Nasser
4207 Engineering Building
R=011, Dept. of Applied Mechanics
University of California, San Diego
La Jolla, CA 92093-0411

Dennis L. Orphal
California Research & Technology, Inc.
5117 Johnson Dr.
Pleasanton, CA 94588

Ake Persson
Dynamec Research AB
Paradisgrand 7
Sodertalje S-15136
SWEDEN

Andrew Piekutowski
Experimental and Applied Mechanics Div.
Research Institute
The University of Dayton
300 College Park
Dayton, Ohio 45469-0180

Dr. Martin N. Raftenberg
U. S. Army Research Laboratory
ATTN: SLCBR-TB-W
Aberdeen Proving Ground, MD 21005-5066

Robert M. Schmidt
Boeing Defense & Space Group
P. O. Box 3999, MS 87-60
Seattle, WA 98124-2499

Peter H. Schultz
Box 1846
Dept. of Geological Sciences
Brown University
Providence, RI 02912

Lynn Seaman
SRI International
333 Ravenswood Avenue
Menlo Park, CA 94025

Dr. Donald A. Shockey
Dept. Metallurgy and Fracture Mechanics
SRI International
333 Ravenswood Avenue
Menlo Park, CA 94025

Vernon Smith
Kaman Sciences Corporation
P. O. Box 7463
Colorado Springs, CO 80933

Dr. Alois Stilp
Ernst-Mach Institut
Eckerstrabe 4
Freiburg I.Br. D-7800
GERMANY

Hallock F. Swift
Titan Corporation
7546 McEwen Road
Dayton. Ohio 45459

John Thomas
Phillips Laboratory
PL / WSSD
Kirtland Air Force Base
Albuquerque, NM 87117

Dr. Chris Weickert
Defence Research Establishment
Suffield
Box 4000, Medicine Hat
Alberta, Canada
TIA 4B6

Dr. James Wilbeck
Kaman Sciences Corporation
P. O. Box 2486
Huntsville, AL 35804-2486

C. H. Yew
Department of Aerospace Engineering
WRW 316
The University of Texas at Austin
Austin, TX 78712

Dr. Louis Zernow
Zernow Technical Services, Inc.
425 West Bonita Avenue
Suite 208
San Dimas, CA 91773

University of California
Lawrence Livermore National Laboratory
7000 East Avenue
P. O. Box 808
Livermore, CA 94550
Attn: L. A. Glenn, MS L-200
Attn: D. J. Steinberg, MS L-35

Los Alamos National Laboratory
Mail Station 5000
P. O. Box 1663
Los Alamos, NM 87545
Attn: T. F. Adams, MS F663
Attn: J. K. Dienes, MS B216
Attn: B. L. Holian, MS J569
Attn: J. W. Hopson, MS B216
Attn: J. N. Johnson, MS
Attn: D. Mandell, MS F663

Sandia National Laboratories Internal
333 R. E. Smith
1010 L. Lopez
1020 W. Herrmann
1400 E. H. Barsis
1401 J. R. Asay
1422 R. C. Allen, Jr.
1422 L. Romero
1425 J. H. Biffle
1431 J. M. McGlaun

1431 E. S. Hertel
1431 J. S. Peery
1431 A. C. Robinson
1431 T. G. Trucano
1431 L. Yarrington
1432 P. Yarrington
1432 R. L. Bell
1432 P. J. Chen
1432 H. E. Fang
1432 A. V. Farnsworth
1432 G. I. Kerley
1432 M. E. Kipp (25)
1432 F. R. Norwood
1432 S. A. Silling
1432 P. A. Taylor
1433 P. L. Stanton
1433 J. A. Ang
1433 M. B. Boslough
1433 L. C. Chhabildas
1433 M. D. Furnish
1433 D. E. Grady (25)
1434 D. R. Martinez
1561 B. J. Thorne
1562 E. P. Chen
1562 J. W. Swegle (5)
1562 R. K. Thomas
5941 C. M. Craft
6111 J. L. Wise
6418 S. L. Thompson
6418 L. N. Kmetyk
6641 B. D. Zak
7141 Technical Library (5)
7151 Technical Publishing
7613-2 Document Processing
DOE/OSTI (10)
8523-2 Central Technical Files
8741 L. E. Voelker
8743 D. J. Bammann
9614 M. J. Sagartz
9723 M. J. Forrestal

END

DATE FILMED

11/12/93